



**UCGE Reports
Number 20348**

Department of Geomatics Engineering

**Feature-based Boresight Self-Calibration of
a Mobile Mapping System**

(URL: <http://www.geomatics.ucalgary.ca/graduatetheses>)

by

Ting On Chan

December 2011



UNIVERSITY OF CALGARY

Feature-based Boresight Self-Calibration of a Mobile Mapping System

by

Ting On Chan

A THESIS

SUBMITTED TO THE FACULTY OF GRADUATE STUDIES
IN PARTIAL FULFILLMENT OF THE REQUIREMENTS FOR THE
DEGREE OF MASTER OF SCIENCE

DEPARTMENT OF GEOMATICS ENGINEERING

CALGARY, ALBERTA

December, 2011

© Ting On Chan 2011

Abstract

Over the past few years, the mobile mapping system (MMS) has become one of the most dominant tools for performing urban road survey. Its captured point cloud has to meet certain accuracies for geomatics applications such as national mapping and infrastructure deformation monitoring and the accuracy strictly relies on a rigorous system calibration scheme. The boresight estimation plays an important role in the overall point cloud quality. Especially when objects are scanned with multiple drive lines and scanners, poor boresight estimation will seriously degrade the accuracy of overlapping of point clouds for the same object. Therefore rigorous, but also cost-effective, boresight calibration methodologies are always desired.

In this thesis, a rigorous boresight self-calibration approach using planar and catenary features that naturally appear in road survey scenes is proposed for boresight calibration of MMSs. Building façades and hanging power cables are two typical examples of the planar and catenary features, respectively, and they can be found in most the modern city roads. The planar and catenary features are both used separately and simultaneously for estimation of the boresights, therefore, the calibration outcome in thesis are classified into three types of calibration: plane-based calibration, catenary-based calibration and mixed feature-based calibration.

A detailed analysis of the calibration is given in this thesis. The calibration results are promising even though they are hindered by lack of some feature geometries. The results also show that both the plane-based and catenary-based calibration have their own shortcomings, but they can be improved with the mixed featured-based calibration.

Acknowledgements

I wish to extend my sincere gratitude to my distinguished supervisor Dr. Derek Lichti for guidance, enlightenment and much encouragement during my studies at the University of Calgary. I also appreciated very much my thesis defense committee for their valuable comments: Dr. Ayman Habib, Dr. Kyle O’Keefe and Dr. Raafat El-Hacha.

It is a pleasure to acknowledge my team members for their assistance and also sharing: Hervé, Sherif, Sonam, Xiaojuan, Jacky, Kathleen, Claudius, Kristian and Tanvir. I would like to thank Ivan, Andrés, David, DLo, Eunju, Kelly and Junbo for helping me during my studies. Also, I thank Tyler, Johnny, Heather, Yan, Kitty and Shawn for making my stay in Calgary wonderful. A final word of sincere gratitude needs to be included for Dawn who is always here to help and inspire me.

Thanks also to Terrapoint Inc. for providing the point cloud data and the estimated bore-sight angles, and to Dr. Craig Glennie for valuable discussion. This research is funded by the Natural Sciences and Engineering Research Council of Canada (NSERC).

Table of Contents

Abstract	ii
Acknowledgements	iii
Table of Contents	iv
List of Tables	vii
List of Figures	viii
List of Acronyms	ix
1 Introduction	1
1.1 Overview of Feature-based Self-calibration for Mobile Mapping Systems	1
1.2 Research Objective	7
1.3 New Contribution of this Work	8
1.4 Thesis Outline	9
2 Introduction to the Mobile Mapping Systems (MMS) and its Error Sources	11
2.1 Overview of the MMS	11
2.1.1 Operation Mode of the MMS	13
2.1.1.1 Stop-and-go Mode	13
2.1.1.2 On-the-fly Mode	14
2.1.2 Difference between the MMS and ALS	15
2.1.3 The Main Components of the MMS	18
2.1.3.1 Imaging System	21
2.1.3.2 Positioning and Navigating System	21
2.1.3.2.1 Integration of GPS and INS/IMU	22
2.1.3.3 Operating System	24
2.1.4 Applications of the MMS	24
2.1.4.1 Highway Corridor and Railway Surveys	24
2.1.4.2 Mining and Tunnels	25
2.1.4.3 Coastal Mapping	25
2.1.4.4 Other Applications	25
2.2 Error Sources of the MMS	26
2.2.1 Boresight Errors	28
2.2.2 Lever-arm Errors	29
2.2.3 Attitude Errors	31
2.2.4 Positioning Errors	32
2.2.5 Scanner Component Errors	33
3 The Positioning Equation of the MMS	36
3.1 Introduction to the Full Positioning Equation for the MMS	36
3.1.1 Transformation from the Sensor Frame (s-frame) to the Body Frame (b-frame)	38
3.1.2 Transformation from the Body Frame (b-frame) to the Local-level Frame (l-frame)	40
3.1.3 Transformation from the Local-level Frame (l-frame) to the Earth-centred, Earth-fixed Frame (e-frame)	42

3.1.4	Transformation from the Earth-centred, Earth-fixed Frame (e-frame) to the Mapping Frame (m-frame)	43
3.2	Background of the TITAN and its Full Positioning Equation	46
4	The Calibration Models and the Least-Squares Implementation	53
4.1	Mathematical Model for Feature-based Self-Calibration	53
4.1.1	Mathematical Model for Plane-based Calibration	54
4.1.1.1	Background	54
4.1.1.2	Functional Model	55
4.1.2	Mathematical Model for Catenary-based Calibration	55
4.1.2.1	Background	55
4.1.2.2	3D Catenary Model	56
4.1.2.3	Symmetry of the Catenary	58
4.1.2.4	Functional Model	58
4.2	Least-Squares Model Implementation	60
4.2.1	Normal Equations with the Constraint	61
4.2.2	Residual Computation	65
4.2.3	Stochastic Model	66
4.2.4	Design Matrices of Unknowns and Observations	67
4.2.5	Efficient Computation of the Normal Matrix and the Residuals	70
4.2.5.1	Efficient Computation of the Normal Matrix - Summation of Normals	70
4.2.5.2	Efficient Computation of the Residuals	71
5	Calibration Input and Results Analysis	72
5.1	Calibration Input Data Set	72
5.1.1	Calibration Data Set Description	72
5.1.2	Initial Approximate Values Estimation for Calibration	74
5.1.2.1	Initial Approximated Values Estimation of the Boresights	74
5.1.2.2	Initial Approximate Values Estimation of Features Parameters	74
5.1.2.2.1	Approximate Values Estimation of the Plane Parameters	74
5.1.2.2.2	Initial Approximate Values Estimation of the Catenary Parameters	75
5.1.3	Feature Extraction	76
5.1.4	Blunder Detections of Calibration Input	76
5.2	Results of Plane-based Calibration	77
5.2.1	Calibration with 56 Planes	77
5.2.1.1	Accuracy Analysis	82
5.2.1.1.1	RMS of Test Plane Fitting	82
5.2.1.1.2	Profile Analysis	83
5.2.1.2	Parameter Correlation	85
5.2.2	Calibration Each Scanner Independently with the 56 Planes	85
5.2.2.1	Accuracy Analysis	86

5.2.3	Examination of the Plane-based Calibration Using Groups of Planes in Parallel and Orthogonal Drive Lines	88
5.2.4	Examination of the Plane-based Calibration Using 24 planes . . .	90
5.2.4.1	Accuracy Analysis	91
5.3	Results of Catenary-based Calibration	96
5.3.1	Calibration with 15 Catenaries: Group 1 and 2	96
5.3.1.1	Parameter Estimation	98
5.3.1.2	Accuracy Analysis	100
5.3.1.2.1	RMS with Test Catenary Fitting	100
5.3.1.2.2	Profile Analysis	100
5.3.1.3	Parameter Correlation	101
5.3.2	Calibration Results using Two Catenaries with Parallel and Orthogonal Drive Lines	102
5.4	Results of Mixed Feature-based Calibration	106
5.4.1	Accuracy Analysis	107
5.4.1.1	RMS of the Test Plane Fitting	107
5.4.1.2	Profile Analysis	107
5.4.2	Parameter Correlation	108
6	Conclusions and Recommendations for Future Works	111
6.1	Conclusions	111
6.2	The Advantages of the Developed Calibration Method	113
6.3	Recommendations for Future Works	114
	References	116

List of Tables

2.1	Current popular commercial MMSs	20
2.2	Common TLS used in MMSs and their range accuracy (range dependent)	34
5.1	Calibration results with 56 input planes	79
5.2	The plane types of the 56 planes	81
5.3	Calibration results for solving the four sets of boresight independently . .	87
5.4	The groups of planes used to examine the impact of using planar features captured by the system travelling in orthogonal drive lines	89
5.5	The results of the plane-based calibration using groups of planes in parallel and orthogonal drive lines	90
5.6	Results comparison of the plane-based calibration using 56 and 24 planes	93
5.7	The normalized height difference of the input catenaries	96
5.8	RMS z of input catenary fitting	97
5.9	Catenary-based calibration results with Group 1 and 2 catenaries	99
5.10	RMS z of 10 test catenaries	101
5.11	Calibration results of catenary-based calibration using 2 catenaries	105
5.12	Results comparison of the plane-based calibration (24 planes) and the mixed feature-based calibration (24 planes and 15 catenaries)	106

List of Figures

2.1	The simplified positioning equation of the MMS	14
2.2	Operation modes of the MMS	15
2.3	Direct-georeferencing principle of MMS and ALS	16
2.4	Three principal components of the MMS	19
2.5	Lever-arms of the MMS	30
3.1	The full positioning equation of the MMS	37
3.2	Transformation from the Sensor Frame (s-frame) to the Body Frame (b-frame)	39
3.3	The range and the encoder angle measurements of the 2D-Line scanner	39
3.4	Commonly-defined body frame (b-frame) of the MMS	40
3.5	The East-North-Up (ENU) or the North-East-Down (NED) coordinate systems	41
3.6	The rotation from the body-frame (b-frame) to the local-level frame (l-frame) - ENU	42
3.7	The Earth-centred, Earth-fixed frame/coordinate system	43
3.8	The rotation from the different local-level frames (ENUs) at different epochs, t_1, t_2, t_3 to the Earth-centred, Earth-fixed frame (e-frame)	44
3.9	The rotation from the ENU to the ECEF frame	45
3.10	The rotation from the NED to the ECEF frame	45
3.11	The rotation from the Earth-centred, Earth-fixed frame (e-frame) to mapping frame (m-frame)	46
3.12	The TITAN System	47
3.13	The TITANs mounted on the hydraulic racks built on trucks	48
3.14	The TITAN system assembly	48
3.15	Scanner orientation	49
3.16	Simulated TITAN scanning coverage	49
4.1	Correlation between b and c vs the normalized height difference (between the two ends) of the simulated catenaries (Chan and Lichti, 2011)	59
5.1	The Google Map TM and point cloud of the captured highway scene in Montreal	73
5.2	Calibration zone 1: The intersection of the highway and the bridge	74
5.3	Calibration zone 2: The hotel adjacent to the ramp	74
5.4	The Drive Lines	75
5.5	The point clouds captured by Scanner 1, 2, 3 and 4 are depicted by pale green, red, cyan and blue color respectively	76
5.6	The residuals of plane-based calibration adjustment using 56 planes	78
5.7	Scanner 1 and a vertical plane with γ_a (Top) and γ_b (Bottom)	80
5.8	The geometry of Scanner 1 and five vertical planes with different normal vectors	81

5.9	The geometry of Scanner 1 and five tilted/horizontal planes with different normal vectors	82
5.10	The Scanner 1 and a vertical plane in an arbitrary orientation	83
5.11	The geometry of Scanner 3 and a horizontal plane	84
5.12	RMS of the test plane fitting with the point cloud of before, Terrapoint and after calibration	85
5.13	Horizontal profile of highway surface reconstructed	86
5.14	The z -measurement of the horizontal profile reconstructed	87
5.15	The difference in z of the horizontal profile	88
5.16	Horizontal profile of bridge side reconstructed	89
5.17	The $x - y$ plane of the bridge side reconstructed	90
5.18	The difference of the $x - y$ position of the bridge side in terms of u , where $u = \sqrt{x^2 + y^2}$	91
5.19	Correlation Matrix of plane-based calibration adjustment using 56 planes. The yellow highlights the boresight parameters, the red highlights the plane parameters	92
5.20	RMS of the test plane fitting with the point cloud of before, after calibration with 56 planes and calibration with 56 planes independently	93
5.21	RMS of the test plane reconstructed from the boresight of calibration using 56 planes (without \perp drive lines) and 24 planes (with \perp drive lines)	94
5.22	The difference in z of the horizontal profile	94
5.23	The difference of the $x - y$ position of the bridge side in terms of u , where $u = \sqrt{x^2 + y^2}$	95
5.24	The $x - y$ position of the 18 catenaries	97
5.25	Scanner 1 and 2 scan the catenaries	99
5.26	The residuals of catenary-based calibration adjustment using 15 catenaries	100
5.27	The difference of the $x - y$ position of the bridge side in terms of u , where $u = \sqrt{x^2 + y^2}$	101
5.28	Correlation Matrix (absolute value taken) of the catenary-based calibration using the 15 catenaries (Group 1 and Group 2), the yellow highlights the boresight parameters and the green highlights the catenary parameters	103
5.29	The geometry of α and a_c	104
5.30	The x - y position of the catenaries	104
5.31	Correlation Matrix of the catenary-based calibration using only Catenary 2 and 17 (\perp case) and Catenary 2 and 3 (\parallel case), the yellow highlights the boresight parameters and the green highlights the catenary parameters	105
5.32	RMSs of the test plane fitting	107
5.33	The difference in z of the horizontal profile	108
5.34	The difference of the $x - y$ position of the bridge side in terms of u , where $u = \sqrt{x^2 + y^2}$	109
5.35	Correlation Matrix with calibration solving boresights with 24 planes and 15 catenaries. The yellow highlights the boresight parameters, the red highlights the plane parameters and the green highlights the catenary parameters	110

List of Acronyms

ALS	Airborne Laser Scanning
AR	Augmented Reality
CIO	Conventional International Origin
CTS	Conventional Terrestrial System
DGPS	Differential Global Positioning System
DOF	Degree Of Freedom
ECEF	Earth-centred Earth-fixed
ENU	East, North, Up
FOG	Fibre Optic Gyro
FOV	Field Of View
GPS	Global Positioning System
GPS/IMU	GPS/IMU Integration
GPS/INS	GPS/INS Integration
ICP	Iterative Closet Point
IMU	Inertial Measurement Unit
INS	Inertial Navigation System
ISA	Inertial Sensors Assembly
LiDAR	Light Detection And Ranging
LTP	Local Tangent Plane
MEMS	Micro Electro Mechanical System
MLS	Mobile Laser Scanning
MMS	Mobile Mapping System
NED	North, East, Down
PC	Personal Computer
POS	Position and Orientation System

PPS Pulse-Per-Second

RLG Ring Laser Gyro

RMS Root Mean Square

RTK Real-Time Kinematic

TITAN Tactical Infrastructure and Terrain Acquisition Navigator - an MMS developed by Terrapoint Inc.

TLS Terrestrial Laser Scanner

UTM Universal Transverse Mercator

VLS Vehicle-based Laser Scanning

VRS Virtual Reference Station

Chapter 1

Introduction

1.1 Overview of Feature-based Self-calibration for Mobile Mapping Systems

Rapid developments in terrestrial mobile mapping systems (MMSs) in recent years have brought road survey into a new era. Multi-scanner MMSs are capable of collecting a huge amount of directly georeferenced 3D data within a short time frame. The data capture capacity varies from system to system, but an average MMS can collect up to 10000 data points per second with the platform moving as fast as 100 km/h. The quantity of data acquired exceeds incomparably that captured with static terrestrial laser scanners (TLS) or light detection and ranging (LiDAR) systems mounted on tripods. These developments have enhanced many geomatics applications such as urban 3D mapping (Shi et al., 2008; Haala et al., 2008; Becker and Haala, 2009), urban planning (Leslar, 2009), tunnel construction (Ishikawa et al., 2009; Lam, 2010), road and railway construction (Wildi and Glaus, 2002; Morgan, 2009), topographic mapping (Alho et al., 2011), and many others. MMSs also enable various geomatics applications, for example, mobile geospatial technology used in automatic object recognition, real-time highway centerline mapping, and thematic mapping (Grejner-Brzesinska et al., 2004). These applications can be also extended from land to rivers/oceans to perform coastal survey (Böder et al., 2011). More details regarding the application of MMSs will be discussed in the coming sections.

An MMS is composed of multiple subsystems which have their own individual mea-

surement errors. Additionally, the assembly of the whole system will incur errors from positioning and orienting the sensors (boresight and lever-arm). Certainly, the presence of these errors will degrade the final accuracy of the coordinates of the georeferenced target point. While the accuracy is system dependent, it is typically at the sub-decimetre level for both horizontal and vertical directions after calibrations. According to Glennie (2007b), the error sources of MMSs can be categorized into five major types: (1) IMU attitude errors, (2) boresight errors, (3) laser scanner errors, (4) lever-arm offset errors, and (5) GPS positioning errors. These five error sources will be discussed in detail in Chapter 2. Practically, the boresight errors can critically degrade the quality of the point clouds. The point cloud of the same object captured with multiple opposite drive lines will not overlap each other correctly if there are errors found in the boresight. Cross-sections of houses' inclined roofs and grounds can be good indicators for inspecting the boresight errors in airborne laser scanning (ALS) (Skaloud and Lichti, 2006).

MMSs can be made from various subsystems and assemblies with different calibration methods. As a result, MMSs have a wide range of accuracies. Glennie (2007a) showed the root mean square (RMS) error of the data captured with the TITAN system, compared with the ground-truth, to be 4.1 cm and 2.8 cm in the horizontal and vertical directions respectively. Barber et al. (2008) evaluated the accuracy of the StreetMapper system and got an approximate 3 cm accuracy in the vertical direction and a relatively lower accuracy (10 cm) in the horizontal direction. The LYNX V100 and V200 systems from Optech Inc. in Canada claimed an absolute accuracy of 5 cm in their specification (Optech, 2011). The Mobile Laser Scanning System developed by Wang and Jin (2010) at Shandong University of Science and Technology in China showed the horizontal and vertical accuracy of their system to be around 4 cm and 7 cm respectively. Vertical accuracy is generally lower than horizontal accuracy as it is always predominantly limited

by the GPS accuracy. This is also the reason why when the GPS error is excluded in the error analysis of Glennie (2007b), the horizontal errors over the range is always less than the vertical errors.

One of the recent prevalent trends in MMS research is to investigate different methodologies to calibrate the MMS in order to raise the overall measurement accuracy. Basically, the calibration of individual sensors (static TLS) and the whole system (ALS and MMS) can be categorized into two major types: point-based and feature-based (mainly planar-based).

Although the design and fabrication of TLSs are advanced, they still contain systematic errors which can be tracked and modelled (Reshetyuk, 2010; Lichti, 2007, 2010). To do so, a large a number of artificial control points are required. Moreover, since TLS captures points discretely, the exact target point centre may not be captured as a data point, therefore, the pin-point location of this control point needs to be calculated from surrounding data points with multiple fitting steps (Lichti et al., 2007; Chow et al., 2010). Apart from this, using discrete points for calibration may introduce errors dependent on the sampling density and the beamwidth (Skaloud and Lichti, 2006). As a result, some researchers started to investigate using various features, particularly planar features for self-calibration of static TLS (Bae and Lichti, 2007; Lichti, 2010; Chow et al., 2011).

Using features for sensor calibration can be traced back to 1970's. Brown (1971) first proposed using linear features to calibrate cameras, which later became known as the plumb-line calibration. Its basic idea is that a straight line in object space should appear as a straight line in sensor space and any deviation from the straightness in sensor space is attributed to lens distortion. Although the plumb-line method could not estimate the ex-

terior orientation parameters (EOP) of cameras, it eliminates the need for control points as well as the need for multiple images captured in different positions and orientations, which makes in situ camera calibration more flexible. Linear feature-based calibrations have also been adapted into self-calibration of cameras (Habib et al., 2002) to make the calibration process simpler and more cost-effective. The potential problems of using point-based calibrations in TLS systems, as well as the success of feature-based calibration with traditional photogrammetry, have encouraged the introduction of feature-based calibration into static TLS and also ALS and MMS.

Recently, the feature-based calibration has become one of the dominant trends in the area of calibration research. Feature-based calibration methods can be classified into two main types based on the calibration adjustment principle:

1. Least squares estimation of calibration parameters with planar features used as adjustment constraints (Filin, 2003; Skaloud and Lichti, 2006; Glennie and Lichti, 2010, 2011).
2. Iterative Closest Point (ICP) estimation of the parameters or parameter offsets based on minimization of the discrepancy of points on features (planar or non-planar) from overlapping strips (Rieger et al., 2010; Kumari et al., 2011).

Filin (2003) was one of the first who used planar features in LiDAR system calibration. The boresight angles and the range finder offset of the airborne scanner are estimated by least-squares adjustment based on some fixed plane parameters in different orientations. It has shown that planes with the same orientation will result in high correlation existed between the range finder offset and one of the boresight parameters and thus lower the reliability of the calibration results.

Skaloud and Lichti (2006) presented their new approach for calibrating ALS boresight angles using natural planar surfaces appearing in the scene, for example, soccer fields, flat and inclined roofs of buildings. Extending from the basic form of Airborne LiDAR equations (Baltsavias, 1999), the LiDAR range measurement in the scanner space underwent a series of rigid body transformations to the position in the mapping frame, then the parameters (boresight and range finder offset) were adjusted along with the plane parameters such that the points were lying on the best fit planes. This method presented significant improvement in accuracy when data after the calibration was evaluated with independent plane fitting. However, the range finder offset was shown to have high correlation with the d parameter (the orthogonal distance between the plane and the origin), and its estimated value was found to be unrealistic with this method.

Glennie and Lichti (2010, 2011) applied a similar planar feature-based concept to carry out static calibration of a Velodyne HDL-64E S2 scanner, mounted on a MMS. The Velodyne HDL-64E S2 is neither a hybrid nor panoramic type of scanner - it contains a compact sensor pod that is built with an array of 64 2D line scanners. Each sensor has a 27° field of view(FOV) and the whole sensor can rotate 360° . Since the structure is different from other scanners, the mathematical model and calibration parameters are also different from other scanners, and the measurement does not include GPS/IMU position and thus no boresight angles are considered. The use of planar features was once again demonstrated to be able to improve the accuracy as the root mean square error (RMSE) of the planar disclosure is evidently reduced.

Instead of adjusting the boresight angles directly like Skaloud and Lichti (2006), Kumari et al. (2011) proposed another approach that estimates boresight discrepancies based on the minimization of the relative position differences of points between overlapping strips

captured by an airborne system using the ICP algorithm. They displayed encouraging results that show errors are significantly reduced with almost no correlation between the estimated parameters after applying this approach. Since the Gauss-Helmert least squares is used to estimate the minimum differences between points, stochastic models can be introduced and reliability of the parameter estimation is then examined by investigating the correlation matrices. Similar to the boresight calibration using planar features (Skaloud and Lichti, 2006), the LiDAR position equation for estimating the final coordinates in the mapping frame is first formulated by calculating the differences between points iteratively until the final overall differences converge to a specified threshold. As the ICP method usually requires a high number of iterations and the volume of airborne data is relatively large, the iterative computation can be very demanding in terms of computation power. Therefore, specific computation algorithms must be considered with regard to time and internal memory size.

Meanwhile, Rieger et al. (2010) from Reigl GmbH in Austria have developed a boresight alignment method based on ICP with planar surface point clouds as the input. The method has been successfully applied to boresight calibration of their self-developed 3D scanning MMS. This MMS utilizes a VZ-400 scanner, which is a 3D scanner that is different from many alternative MMS that only have 2D scanners. The approach they developed basically iteratively varies the boresight to minimize the root mean square value of projected distances onto the normal vectors of point clouds of planes captured by various scanning runs with different driving and scanning directions. In other words, this method utilizes the fact that point clouds of the same planes captured with different runs should overlap with minimal difference if the estimation of the boresight is accurate. This approach mitigates the problem of using artificial control points and control features since plane surfaces can commonly be found from the scene of MMSs. Furthermore,

on-site calibration can be executed as long as a sufficient number of planar features exist in the scene. Calibration can also be done with the end product, after data collection has occurred.

LiDAR is always able to capture the 3D positions along with the reflected intensity. Some researchers, e.g. Hefford et al. (2009), have attempted to incorporate this additional information into MMS calibration. They utilized ICP augmented with intensity to estimate the GPS position discrepancy of overlapping strips of sensors from a multi-sensor based MMS named TITAN and they showed that the integration of the intensity into ICP has increased the accuracy. For ALS, Burman (2000) have estimated the orientation errors based on the discrepancies between overlapping strips in terms of the height and the reflected intensity.

1.2 Research Objective

As mentioned earlier, using features in calibration can reduce the time and cost for setting up artificial control points, but it also can mitigate problems associated with the discrete sampling nature of LiDAR. Apart from this, an MMS always comprises more than one scanner to maximize the scanning coverage. Therefore, this research is dedicated to develop a featured-based multi-scanner boresight calibration technique for MMSs. Building on the work on the plane-based single-scanner boresight calibration of ALS by Skaloud and Lichti (2006), this research attempts to incorporate the catenary features from hanging power cables to the calibration, and also extend the estimation of boresight calibration from a single scanner to multiple scanners (up to ten scanners). In other words, this research aims at developing a multi-feature, multi-scanner boresight calibration technique for MMSs. Since the plane and catenary features can all be commonly found along many

highways, this technique is particularly suited for in-situ calibration.

The implementation of catenary-based calibration is motivated by the successful development of a new robust 3D equation by the contribution of the author in Chan and Lichti (2011) in the mid-way of this research.

The accuracies of the independent calibrations using planar features, catenary features and both the features are compared in terms of RMS of fitting of test features. Also, the reliabilities of the parameters estimation of the calibration are examined by the analysis of the correlation matrices. The geometry of the features and the calibration precision are also discussed.

1.3 New Contribution of this Work

This section summarizes the main contributions of this works as the following:

1. This work successfully calibrates the boresight of multi-scanners MMS (four scanners) using planar features with the least-square approach, which to the author's knowledge, no previous work has been reported. The calibration results showed that an average RMS of independent plane fittings in the vertical and horizontal directions of approximately 2.5 cm and 3 cm respectively.
2. A new robust 3D mathematical model for catenary curve was developed during the mid-stage of this research and detailed experimental results were reported in Chan and Lichti (2011). The model was evaluated with fitting of point cloud of catenary (hanging power cable) and therefore can be used in feature-based calibration or road scene object segmentation.
3. The 3D catenary model mentioned above is used for integrating catenary features

with the calibration of boresight as the planer features. The calibration results showed that promising accuracy can be achieved, an average RMSz of approximately 10 cm of independent catenary fittings (the range of the catenaries is approximately 40 m on average). To the author's knowledge, the work is the first publication concerning the use of catenary features in calibration.

4. The final outcome of this research is to calibrate the boresight using both the planar and the catenary features simultaneously. No previous calibration, either in MMS or static TLS, has more than one type of geometric features involved.

1.4 Thesis Outline

This thesis is organized as follows. Chapter 2 gives a detailed overview of MMS and its components. Updated details of some of the current dominant MMSs will be briefly discussed along with their accuracy. Also, some application examples of the MMS will be given. The major error sources of the various MMS will also be discussed in this chapter.

Chapter 3 presents the detailed position equation of the MMS and the position equation of the TITAN system. The background of TITAN will also be discussed.

Chapter 4 gives the geometric models of the planar and catenary features, and also the functional models for the calibration. The Gauss-Helmert model implementation of the functional models in efficient ways will be given.

In Chapter 5, the calibration data set will be first described and the data pre-processing is addressed. Then, results of the planar-based, catenary-based and a mix of the planar and catenary feature-based (mixed feature-based) calibration are analysed in terms of

independent features fitting and correlation matrix. The performance of the stochastic model is discussed. The geometry of the planes and the boresight accuracy are also discussed based on some simulated data.

Chapter 6 provides conclusions to the work and future recommendations. The important outcome of the research is summarized. Some recommendations for the future development of this research are briefly elucidated.

Chapter 2

Introduction to the Mobile Mapping Systems (MMS) and its Error Sources

2.1 Overview of the MMS

An MMS, is an integration of an imaging system and a near real-time direct-georeferencing system. The MMS usually refers to such a system that is installed on top of a moving platform that moves on terrestrial or aquatic surfaces. If its imaging system has the TLS/LiDAR as the dominant sensor, it can also be referred to as mobile laser scanning (MLS). Sometimes, the MMS is also referred to as kinematic or dynamical laser scanning. For the MMS built upon vehicles, the term vehicle-based laser scanning (VLS) is used (Boulaassal and Grussenmeyer, 2011). For the LiDAR-based MMS that is developed along with or mounted on an aircraft, it generally refers to ALS. Strictly speaking, ALSs share the basic characteristics of MMSs and thus can be classified as MMSs. However, the term MMS is generally referred to the mapping systems associated with the land-based applications which exclude the ALS, in most literature (e.g. Grejner-Brzezinska (2001); Petrie (2010); Vosselman and Mass (2010)). Mostafa and Schwarz (2001) defined MMS as “the product of integrating the concepts of kinematic geodesy and digital photogrammetry, to acquire, store, and process measurable quantities that sufficiently describe spatial and/or physical characteristics of a part of the Earth’s surface”. Moreover, as described by the webpage of the Center for Mapping of the Ohio State University (2011) which built one of the first generations of the MMS, the structure is “a moving platform, upon which multiple sensor/measurement systems have been integrated, to provide three-dimensional near-continuous positioning of both the platform and simulta-

neously collected geo-spatial data”.

A more general definition of the MMS is that a system with an image metrological system (imaging system) mounted on any moving platform (e.g. vans, trucks, rail cars, vessels, boats and etc.) that performs measurements as the platform moves. The system also consists of a position and attitude measuring device comprising an integrated Global Positioning System (GPS) receiver and Inertial Measurement Unit (IMU), it is also known as GPS/INS and sometimes refers to Position and Orientation System (POS). The position of a measured target point is calculated from the information collected with the GPS/IMU using the position equation (Equation 2.1) and the measurement of the imaging system rotated to a common mapping frame. Thus each point measurement can be direct-georeferenced in almost real-time while the data density point depends on the overall sampling rate of the whole system. The first generation of the MMS is composed of cameras and GPS/IMU systems (Grejner-Brzezinska, 2001; Schwarz and El-Sheimy, 2004; El-Sheimy, 2005). See the VISATTM system (El-Sheimy, 1996) as an example. As the design of the terrestrial laser scanner (TLS) continuously improves and becomes less costly, TLS has now become the main image metrological component of the MMS. Nevertheless, in most cases, the cameras are still kept in the system mainly for visualization. More about the MMS and its application can be found on Shan and Toth (2009) and Vosselman and Mass (2010).

Figure 2.1 illustrates the basic principle of an MMS and the corresponding positioning equation is given as Equation 2.1. It can be seen that the measurements of the GPS/IMU and the scanner are combined for estimating the position of the target . Such a combination can be only done before both the GPS/IMU and scanner measurements are transformed to a common frame, also known as the mapping frame. Equation 2.1 is

a simplified version of the full positioning equation that is extended with several more rotations and a translation. The full positioning equation will be discussed in Chapter 3. The boresights, or the boresight angles, (α , β and γ in Equation 2.1) are the Euler angles of rotation between the sensor frame and system body frame. The boresight angle are the main focuses in this research.

$$P_{target}^m(t) = P_{IMU}^m(t) + R_b^m(t)(a_s^b + R_s^b(\alpha, \beta, \gamma)P_{target}^s(t)) \quad (2.1)$$

where,

$P_{target}^m(t)$ is the target coordinates in the mapping frame;

$P_{IMU}^m(t)$ is the GPS/IMU centre coordinates in the mapping frame;

$R_b^m(t)$ is the rotation matrix from body frame to mapping frame;

a_s^b is the lever-arm between the scanner centre and GPS/IMU centre;

$R_s^b(\alpha, \beta, \gamma)$ is the rotation matrix from sensor frame to body frame;

α , β and γ are the boresight angles about y , x and z -axes of the sensor frame respectively;

$P_{target}^s(t)$ is the target coordinates in the scanner frame;

t is epoch.

2.1.1 Operation Mode of the MMS

2.1.1.1 Stop-and-go Mode

The MMS can be operated in two modes, one of them is the “stop-and-go” mode as illustrated in Figure 2.2. In this method, scanning is performed when the platforms stops at different locations. Note that the INS unit is not used in this mode, instead, only the GPS records the scan location. The whole dataset comprises a series of point clouds whose points are captured in a common local coordinate system. The registration of point clouds after surveys is carried out with the control points having known coordinates.

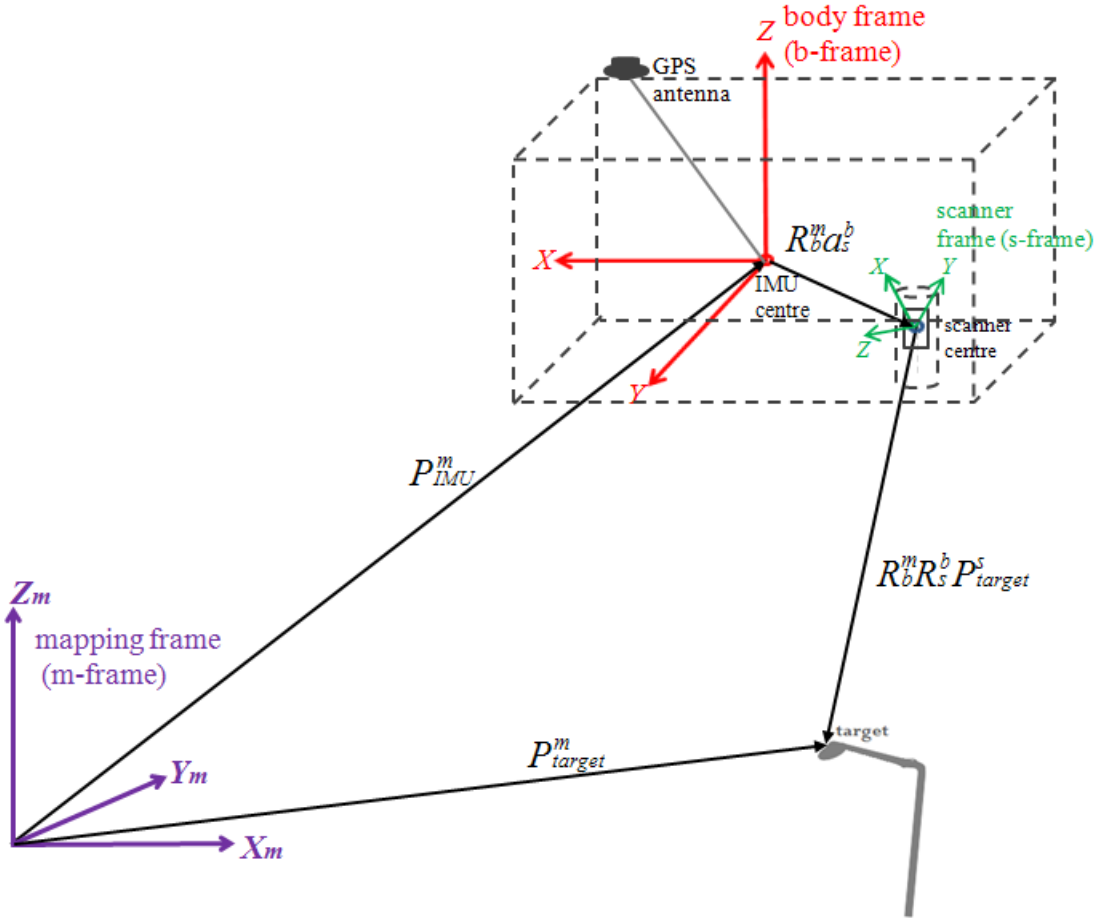


Figure 2.1: The simplified positioning equation of the MMS

This operating mode is similar to the situation of when a TLS mounted on a tripod is repeatedly located to different scan spots to perform scans. Therefore, “stop-and-go” can provide the accuracy similar to static TLS but with a more time efficient performance.

2.1.1.2 On-the-fly Mode

Another operation mode of MMS is the “on-the-fly” mode as illustrated in Figure 2.2. Unlike the “stop-and-go” mode, in which each point cloud captured is in the same local coordinate system, under “on-the-fly” mode is each point cloud has a distinct local coordinate system. The position (3D coordinates in a global frame) and attitudes (roll, pitch and yaw) of the platform vary point to point, therefore, points are captured at different

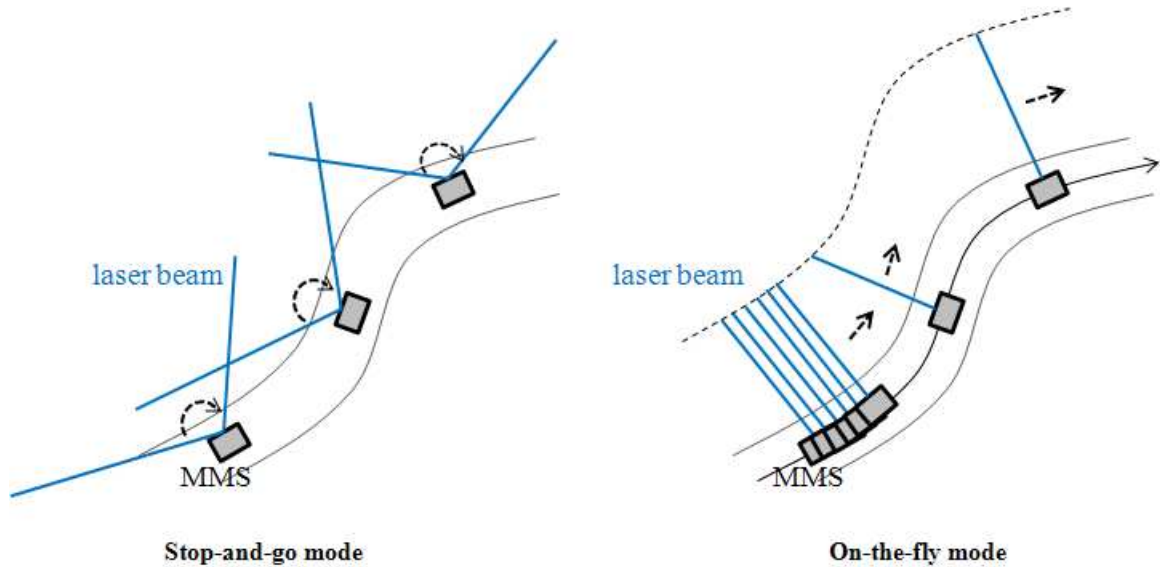


Figure 2.2: Operation modes of the MMS

local coordinate systems at each epoch in respect to a global system (e.g. Earth-Centered, Earth-Fixed (ECEF) system). All the points captured are eventually transformed into a common local mapping system as the survey end-product. Most of the applications of MMS are carried out under the “on-the-fly” mode due to its superior time and cost efficiency for its almost instantaneous direct capture of huge amount of 3D coordinates, similar to the ALS. For more about the two operation modes, please see Chapter 9 of Vosselman and Mass (2010).

2.1.2 Difference between the MMS and ALS

The “on-the-fly” mode MMS is very similar to ALS in terms of the position modelling. Figure 2.3 depicts an operating MMS and ALS. In general, ALS cannot survey the façades of building while MMS is capable to do this and therefore, it becomes the major surveying tool for 3D city models. Even though the basic model of MMSs is very similar to that of ALSs (Baltsavias, 1999), there are some differences between them that are worthwhile noting. Examples are listed as follows:

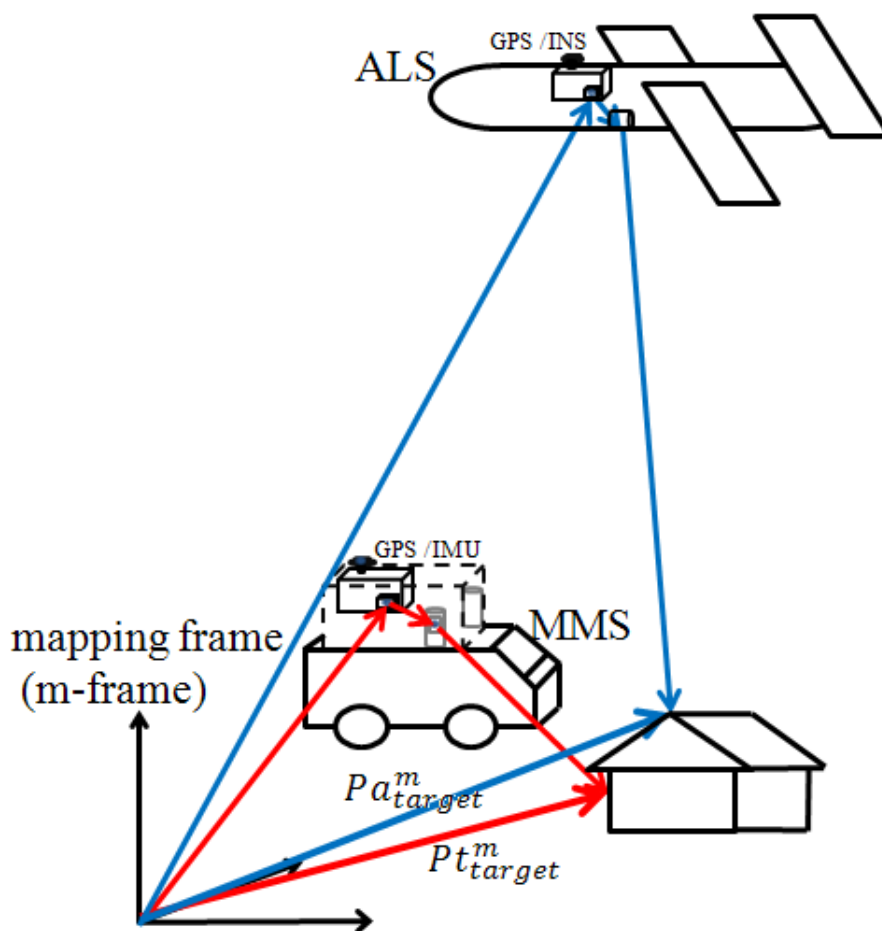


Figure 2.3: Direct-georeferencing principle of MMS and ALS

(1) Number of sensors: In the ALS, there is usually one laser scanner, while an MMS usually has more than one scanner (2-4) because more scanners are needed to increase the coverage of the scans.

(2) Difference in laser measurement and point density: The time-of-flight measurement of the ALS is based on the pulse method. The idea is to estimate the distance between the laser and the target based on the time taken for a pulse to bounce back. The strength of the pulse decreases as the flying height increases while seriously attenuated returning pulses cannot be detected. Therefore, multiple pulse measurements have been introduced to increase the point density to allow operating ALS at higher altitudes. See Shan and Toth (2009) for more about the background of ALS. On the other hand, the time-of-flight measurement of MMS can be either based on pulse-based or the phase comparison method, e.g. Zhu et al. (2011). Instead of emitting a series of pulses, a continuous waveform from the laser is radiated in the phase comparison method. This method estimates the distance between the laser and the target by interpreting the phase of the laser waveform emitted which bounced back.

Typically, ALS is operated at altitude of 80 – 3500 metres; however, MMS is operated at a distance no larger than several hundred metres from the target. Due to the difference in the range and also the laser time-of-flight measurement techniques, ALS point density is only several points per square metre in general while MMS point density can reach several thousands per square metre. For ALS being operated at altitude of 1000 – 3000 m, the vertical accuracy varies from 5 – 30 cm and the horizontal accuracy is approximately 50 – 150 cm (Bang, 2010). On the contrary, the current MMS accuracy is at the sub-decimetre level.

(3) GPS signal availability: ALS is always operated at higher altitudes so that it is always exposed to good satellite geometry. As a result, the GPS signal received by ALS is relatively accurate and stable compared to MMS. MMS usually travels within urban areas for surveying. Tall buildings, bridges and other infrastructure are all commonly-found in urban areas and they potentially block GPS receivers from receiving signals. This greatly lowers the GPS's position accuracy and contributes to the overall system accuracy. See more about GPS accuracy in the Section 2.2.4.

(4) Boresights: The boresight angles of the ALS are usually very small (less than 1°) while that of the MMS can be a relative large value (for e.g. 270°). Therefore, small angle approximations cannot be used.

(5) IMU requirement: The ALS always requires a higher grade and a more costly INS that contain a higher grade IMU (navigation-grade IMU). Even though MMS's IMU is in a relatively lower grade (tactical-grade), it can be the most expensive component in the whole system. See Section 2.2.3 for more about different IMU grades.

(6) Scanning geometry: The ALS is usually in nadir-looking while the MMS is able to scan in other directions (e.g. two sides, upward and downward scanning in TITAN). Besides, the MMS can only perform scanning in one direction on a lane of a two-way traffic.

2.1.3 The Main Components of the MMS

There are three principal components of an MMS (Figure 2.4): (1) Imaging System: This system is primarily comprised of TLSs for collecting spatial measurement, such as range

and encoder angle, and also the light intensity reflected back from the target. Other imaging sensors such as digital cameras (DC) or video cameras (VC)) are also often embedded in the system for auxiliary purposes such as visualization while acting as supplementary information for scene analysis; (2) Positioning and Navigating System: This consists principally of an integrated GPS/IMU integration system which consistently delivers highly accurate positions in the global mapping system and attitudes (roll, pitch, yaw) during the navigation of the system; (3) Operating System: This system is usually a high-level computer with specific software packages for coordinating different components. Its functionalities include, time synchronization, data communication, processing and storage. Finally, other components such as an odometer, distance measurement indicator (DMI), and thermometer are sometimes incorporated depending on the system's design to provide complementary measurements. Information from some manufacturers' webpages and datasheets have been summarized in Table 2.1 to give an overview of the components of the current popular commercial MMS around the world.

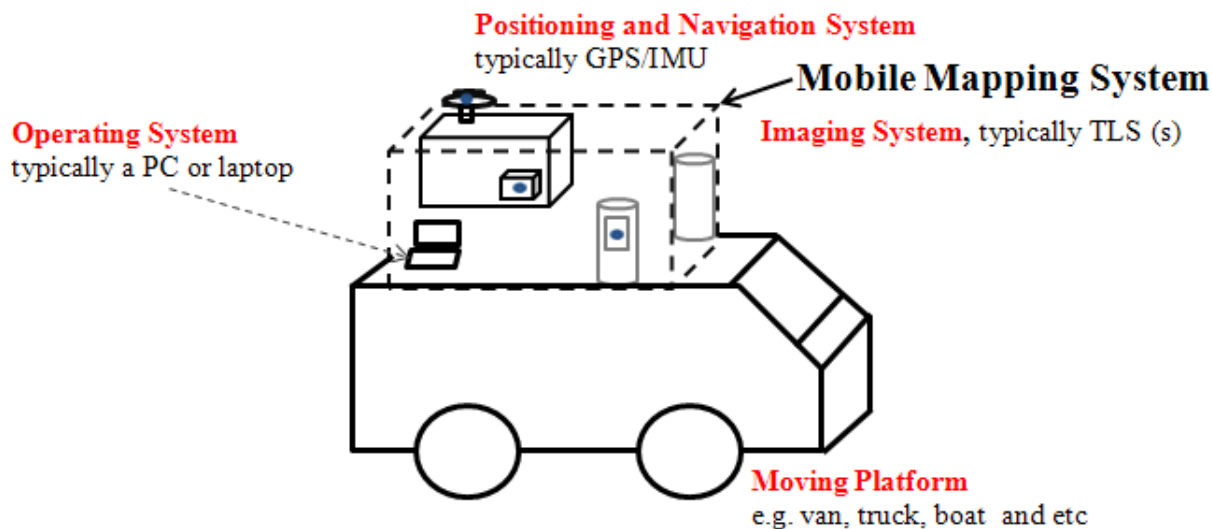


Figure 2.4: Three principal components of the MMS

Table 2.1: Current popular commercial MMSs

System	Developer	GPS	INS/IMU	Scanner	no. of Other Scanner hardware	Software	References
TITAN	Terrapoint Inc.	NovAtel OEM-4	Honeywell 1700 RLG	Riegl Q-120/140	4 Sony DVC, 11 Mpixel DC	CAPTIN (Neptec Inc.)	Glennie et al. (2006) Glennie (2007b,a) Hefford et al. (2009) Harrap and Daniel (2009)
StreetMapper	3D Laser Mapping Ltd IGI GmbH	NovAtel OEMV-3	IGI IMU-IIId FOG based	Riegl VQ-180, VQ-250 and etc	2 - 4 VDC, DC, Touch screen LCD	TERRAoffice, Graf-Nav, Terrasolid software	Kremer and Hunter (2007); Barber et al. (2008);
Lynx Mobile Mapper	Optech	Applanix POS LV420	Applanix POS LV 420	Optech ILRIS-3D	1-4 DC	LYNX-Survey, Process	Morgan (2009); Ussyshkin et al. (2011);
Riegl VMX-250	Riegl GmbH	Applanix POS LV 420	Applanix POS LV 420	Riegl VQ 250/ VZ - 400	1 (3D)/ 2(2D) Camera	Riegl VMX-RiACQUIRE	Rieger et al. (2010)
Trimble MX8	Trimble Inc.	Trimble	unknown	unknown	3 DC	Kronos, Trident-3D Analyst	
IP-S2 HD Mapping System	Topcon Inc. Topcon Co.	Topcon dual-freq 40-channel	Honeywell HG1700	Velodyne HDL-64E	1 DC, odometer	Topcon Geoclean	
TeleAtlas Mobile Mapping Van	TeleAtlas	Fugro OmniSTAR	unknown	SwissSICK/ LASE GmbH/	1-2 6DC, distance measuring device	unknown	
MMS Series	Mitsubishi Electric Co.	Trimble	Crossbow FOG	SICK LMS 291	4 6 DC	Mitsubishi software	

2.1.3.1 Imaging System

Currently, the TLS is the dominant imaging sensor for the MMS. Two-dimensional line scanners, i.e. the scanners that deflect their laser beams in just one plane (e.g. Riegl Q-120 has a scan angle of 80° in the x - z plane), are used in various systems. A 360° scanner is also available in some MMSs. Examples of 360° scanners include the Riegl VQ 250 and the Optech ILRIS-3D. A hybrid TLS, the Faro Photon 80, is used by Vaaja et al. (2011) in an MMS for river side surveying. A hybrid scanner has a horizontal scanning angle of 360° and a vertical scanning angle spanning from a minimum value that is below the horizontal scanning plane, and with a maximum values that can reach the zenith direction (Lichti et al. (2011)). Moreover, the Velodyne HDL-64H S2 TLS provides another alternative scanning mechanism. It consists of an array of 64 lasers and can rotate 360° while scanning. Although the TLS is the presently the main surveying component in the MMS, digital images of scenes are often desired and thus an advanced digital camera or video camera system is highly demanded. Riegl VMX-250-CS6 is a good example for this.

2.1.3.2 Positioning and Navigating System

The amalgamation of the GPS and INS compensates for the demerits of each system to create more accurate and stable positioning and attitude (roll, pitch, yaw) tracking device that has been widely used in navigation and mapping related applications. The system is an essential component of most of the MMS. Such an integrated system is always referred to GPS/INS or in some literatures about the MMS, as the GPS/IMU. The GPS/INS and the GPS/IMU basically mean the same integrated device as the IMU is the core functional component for INS. The INS essentially comprises a navigation computer and the IMU. An the IMU usually contains three gyros and three accelerometers to measure angular velocities and specific force (specific force = acceleration w.r.t.

the inertial frame – gravitational acceleration) respectively. The IMU can deliver the attitudes of a moving rigid body by measuring the angular velocities. The angular measurement accuracy of a high-end IMU can be less than $0.03^\circ/\text{hour}$ (Leyssens, 2009).

The differential GPS (DGPS) is the principal positioning technique used for many survey-related applications and the accuracy of DGPS can reach several millimetres (Dow et al., 2009). The kinematic positioning accuracy of DGPS receivers used in MMS is approximately $2 \text{ cm} + 1 \text{ ppm}$ of the baseline length (horizontal and vertical) with less than a 30 km kinematic baseline (Glennie, 2007b).

2.1.3.2.1 Integration of GPS and INS/IMU

The function of the GPS/INS integration in the MMS is to directly geo-referencing every scanned point by providing the position and attitude of the system body. Instead of integrating INS with the GPS, the INS's main component - the IMU can also be integrated with the GPS, and the IMU only provides the raw inertial data (the incremental velocities and angular rates) instead of the navigation positions and velocities. In ALS, the aircraft always has an INS installed for basic navigation purposes and thus the terms GPS/INS are more often used in ALS, while the term GPS/IMU is used in MMS if only IMU is installed for the navigation. Low-cost IMU/GPS integration techniques for MMS are the subject of ongoing research (Angrisano et al., 2010; Sun, 2010) since the cost of the IMU is the main limitation for its popularity. The GPS/IMU will be used through this thesis.

The two most common GPS/IMU integration strategies are loosely-coupled and tightly-coupled. For many applications, loosely-coupled integration strategy is mostly used,

especially in both the ALS and the MMS. The principle is that the GPS output position, and IMU incremental velocities and angular rates are combined in a separate Kalman filter (Grewal et al., 2007). The errors sources of the GPS/IMU will be discussed in detail in the coming sections as they contribute the total errors budget of the MMS measurement.

The GPS and the INS/IMU have complementary error characteristics and thus their integration possess the advantages from both of them. Much literature regarding the GPS/INS integration and comparison of their advantages exists, see for example, Skaloud (1999). Here a brief discussion is given: the GPS has high long-term accuracy but is dependent on external factors and is also subject to loss of lock and cycle slips with a low update rate. Also, its measurement is insensitive to the gravity. While the INS has only high short-term accuracy but its measurement is autonomous with a high update rate, though it is sensitive to the gravity.

The IMU errors degrade with time while the GPS errors do not. Therefore, the time varying IMU errors are compensated by the GPS measurements through updating the parameters by the filter state vector which is estimated by the predicted INS measurement and the GPS measurement. The Kalman filtering also allows the integrated system to track the drifting parameters of the accelerometers and gyros of the IMU based on the statistical information from both the GPS and the IMU. The integrated system can still maintain high inertial navigation accuracy even GPS signals are not available due to the change of the surrounding (Farrell and Barth, 1999).

2.1.3.3 Operating System

The operating system generally refers to a personal computer (PC) or a computer system integrated with more than one PC installed with specific software packages that coordinate each component with time synchronization signals generated by the pulse-per-second (PPS) module of GPS. Furthermore, the operating system also manages the post-processing and the storage of the data. Note that the collected point cloud should be well organized for storage due to the extremely large data density (Hunter, 2009). The typical data density of an MMS can be up to ten thousand points per square metre and the point clouds captured per km can have a file size of over 1 GB.

2.1.4 Applications of the MMS

As mentioned in Chapter 1, there is a large number of different MMS applications which cover a broad scope. Some examples are detailed in the following four sections:

2.1.4.1 Highway Corridor and Railway Surveys

The MMS is relatively much more cost-effective than traditional road survey approaches and its usage also relieves the safety issues associated with road surveying crews. There are many applications derived from mobile road surveys. For instance, road features such as traffic signs can be segmented automatically (El-Halawany and Lichti, 2011) and vegetation can be identified (Puttonen et al., 2011). Apart from these, automated road rehabilitation (Heikkilä et al., 2004) and road snow cover profiling (Kaasalainen et al., 2011) can be assisted by the MMS. Conventionally, railway track surveys can only be done by technicians and crews. With the MMS, the track survey can be done automatically (Wildi and Glaus, 2002). Another example of its usage is the Optech Lynx which was used intensively in a railway survey project in the US (Morgan, 2009).

2.1.4.2 Mining and Tunnels

In recent years, the MMS has been widely adopted in coal mining industries for various purposes to reduce operation costs. For example, the MMS has been used to provide safer and more efficient mine shaft monitoring, collect spatial data of shafts and tunnels to facilitate the construction design, and estimate underground volumes. The MMS could also be mounted on top of a shaft elevator (TITAN, 2011) or on a remote-controlled vehicle. An excellent example of MMS application with remote-controlled vehicles, found in Hunter (2009), is the 3D-R1 model. The 3D-R1 is a compact MMS, approximately man-sized and equipped with the Riegl 3D scanner. Moreover, the GPS signal is transferred from land surface to underground to support the system. For applications in tunnel construction, see Ishikawa et al. (2009) and Lam (2010).

2.1.4.3 Coastal Mapping

The MMS can be mounted on any platform that moves on aquatic surfaces. This enables a wide variety of applications related to coastal areas. One example is fluvial geomorphologic mapping has been investigated with MMS by Alho et al. (2011). Another example is from Böder et al. (2011), who mounted an MMS on a vessel and surveyed the riverside. This could not be accomplished by vehicle-based MMS.

2.1.4.4 Other Applications

There are still many other applications: (1) Augmented reality (AR) applications. Harrap and Daniel (2009) discussed mobile AR application with the TITAN. (2) Environmental monitoring applications, e.g. Kukko et al. (2010) use MMSs to monitor the fluvial morphology and snow cover. (3) Applications for the oil industry. Pipeline mapping and pigging with MMSs (El-Sheimy, 2003) became popular in the oil industries.

2.2 Error Sources of the MMS

Although many similarities exist between ALS and MMS, the error sources of ALS are not discussed in detail in this section. For more detail about ALS error sources, see (Baltsavias, 1999; Morin, 2003; Habib et al., 2008). The most significant difference in their error sources is the GPS positioning error. As mentioned in section 2.1.2, the GPS error is much higher in the MMS than the ALS since the scenes surveyed with the MMS will always contain dense architectures or vegetations which limits the GPS receiver's exposure to the GPS reference station(s) or GPS satellites. On the contrary, the ALS usually flies over 80 – 3500 m and so it does not suffer from this problem.

Deriving from Equation 2.1, the position in the local-level frame (see Section 3.1.2 for definition) is:

$$\begin{aligned}
 \begin{bmatrix} X(t) \\ Y(t) \\ Z(t) \end{bmatrix}_{target}^l &= \begin{bmatrix} X(t) \\ Y(t) \\ Z(t) \end{bmatrix}_{IMU}^l + R_b^l(r(t), p(t), y(t)) \left(R_s^b(\alpha, \beta, \gamma) \begin{bmatrix} X(\rho(t), \theta(t)) \\ 0 \\ Y(\rho(t), \theta(t)) \end{bmatrix}_{scanner}^s \right. \\
 &\quad \left. + \begin{bmatrix} l_x \\ l_y \\ l_z \end{bmatrix}_{lever-arm}^b \right)
 \end{aligned} \tag{2.2}$$

Glennie (2007) modelled the error sources of MMS by differentiating Equation 2.2 with respect to the 14 variables:

$$\begin{aligned}
\underbrace{\begin{bmatrix} \delta X(t) \\ \delta Y(t) \\ \delta Z(t) \end{bmatrix}^l}_{\text{Total Errors}} &= \underbrace{\begin{bmatrix} \delta X(t) \\ \delta Y(t) \\ \delta Z(t) \end{bmatrix}^l}_{\text{Positioning Errors}} + \underbrace{J}_{\text{Attitude Errors}} \underbrace{\begin{bmatrix} \delta r(t) \\ \delta p(t) \\ \delta y(t) \end{bmatrix}}_{\text{Attitude Errors}} + \underbrace{K}_{\text{Boresight Errors}} \underbrace{\begin{bmatrix} \delta \alpha \\ \delta \beta \\ \delta \gamma \end{bmatrix}}_{\text{Boresight Errors}} \\
&+ \underbrace{M}_{\text{Lever-arm Errors}} \underbrace{\begin{bmatrix} \delta l_x \\ \delta l_y \\ \delta l_z \end{bmatrix}}_{\text{Lever-arm Errors}} + \underbrace{N}_{\text{Scanner Component Errors}} \underbrace{\begin{bmatrix} \delta \rho(t) \\ \delta \theta(t) \end{bmatrix}}_{\text{Scanner Component Errors}}
\end{aligned} \tag{2.3}$$

where,

$$\begin{aligned}
J &= \begin{bmatrix} \frac{\delta P_{target}^l(t)}{\delta r} & \frac{\delta P_{target}^l(t)}{\delta p} & \frac{\delta P_{target}^l(t)}{\delta y} \end{bmatrix} \\
K &= \begin{bmatrix} \frac{\delta P_{target}^l(t)}{\delta \alpha} & \frac{\delta P_{target}^l(t)}{\delta \beta} & \frac{\delta P_{target}^l(t)}{\delta \gamma} \end{bmatrix} \\
M &= \begin{bmatrix} \frac{\delta P_{target}^l(t)}{\delta l_x} & \frac{\delta P_{target}^l(t)}{\delta l_y} & \frac{\delta P_{target}^l(t)}{\delta l_z} \end{bmatrix} \\
N &= \begin{bmatrix} \frac{\delta P_{target}^l(t)}{\delta \rho} & \frac{\delta P_{target}^l(t)}{\delta \theta} \end{bmatrix}
\end{aligned}$$

Based on the analysis of Glennie (2007b), the contributions of each of the four main error sources to the overall accuracy varies with the range (GPS positioning error is not included in the analysis for the great deal of uncertainty in its magnitude, e.g. atmospheric situation, satellite signal availabilities and so on). The GPS error can be simply added back to the estimated error budget as the GPS error is in a linear relation with the error budget. The error adheres to the sensor and is the most dominant of the error sources in the MMS as it contributes over 50% of the overall error budget regardless to the range. In Glennie et al. (2006), the accuracy of an MMS (the TITAN system) is evaluated with a dense network of ground control points. The RMS of a comparison in a vertical position, and less than 1 km distance from the GPS reference station is approximately 6 cm (range

= 10 – 15 m). The corresponding error budget estimated with the Glennie (2007b)'s error model is about 4 – 5 cm. Therefore, when approximately 2 cm GPS error is added to the previously mentioned error budget, an approximately 6 – 7 cm of total error is obtained. This finding has been consistent with the results from the real data estimation and confirmed.

Barber et al. (2008) evaluated the accuracy of an MMS (the StreetMapper system) with two different scenes (a peri-urban residential area and a former industrial area). The reason for selecting the above two scenes was for examining the MMS in situations where one is to the benefit of the MMS while the other is not due to the latter one always having tall buildings that hinder the reception of GPS signal. The evaluation results got an estimation of RMS errors in elevation in about 0.03 m. Moreover, an approximate positional (planimetric) accuracy of around 0.1 m was reported in the peri-urban area, which was worse than the value predicted by the pre-analysis.

2.2.1 Boresight Errors

The boresight angles are fixed physically during the assembly of the system with certain values that should be kept constant throughout the whole scanning process. Miscalculations before the scanning or poor stability of the boresights during the scanning adversely affect the overall accuracy. The boresights cannot be measured by physical means; therefore, they can only be calculated indirectly (estimated by calibration). Several works about calibration of the boresights have already been addressed in Chapter 1. Before the rigorous calibration of the boresights, their approximate values can be found with indoor or rather small scale (short range, e.g. less than 5 m) least-squares based calibration with some overlap strips containing a certain amount of control points and tie points. Alternatively, boresight angles can be found by repeating manual adjustments

empirically until the data of opposing passes visually align. Usually edges of buildings are used during the manual adjustment process. This manual adjustment is rather a time consuming process and demands skilled operators. Glennie (2007b) pointed out that such a manual adjustment is always no better than the least squares approach in terms of accuracy. A routine accuracy level of the boresight angles (α , β and γ) found with the TITAN system by the least-squares approach is 0.001° , 0.001° and 0.004° respectively (Glennie, 2007b).

If the boresights are not accurately estimated by calibration, the point clouds of the same object obtained by two runs in opposite directions will not overlap correctly with each other. Also, the severity of misalignment of point clouds will increase with the range as the vertical errors produced by angular errors are proportional to the range. Rieger et al. (2010) has demonstrated the point clouds misalignment effect due to unmodelled boresights. In the case of a multi-scanner MMS, the point clouds of the same object from different scanners of the same run will also not overlap if the boresights are not well estimated. As a result, it is always critical for MMS users to estimate boresights accurately to guarantee good quality of the point clouds.

The research objective of this thesis is to present an alternative, rigorous boresight calibration methodology for a multi-scanner MMS, using multiple geometric features. The methodology developed in this research is especially suited for in-situ calibration.

2.2.2 Lever-arm Errors

Similar to the boresights, the lever-arm error is one of the system assembly errors. The lever-arm is basically the distance offset between the centres of two sensors and is possible to be measured directly through tacheometric method. In fact, there are two lever-arms

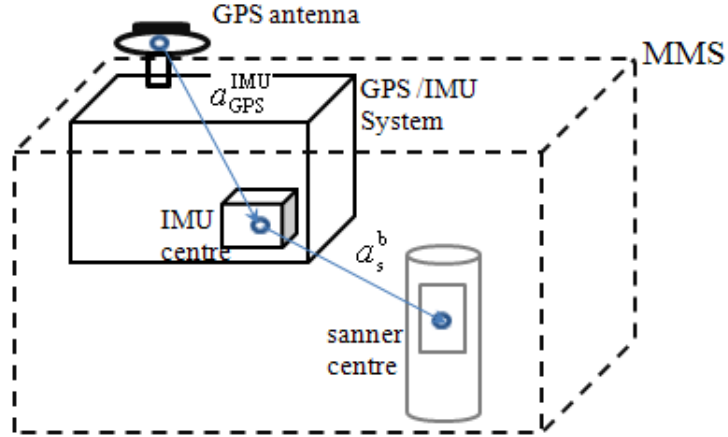


Figure 2.5: Lever-arms of the MMS

in an MMS. The first is the lever-arm between the GPS receiver and the IMU centre (a_{IMU}^{GPS} in Figure 2.5) and it can be as large as several metres. This can be found independently in laboratory using a combined method of tacheometry and photogrammetric bundle adjustment (Vallet and Skaloud, 2004). Since this lever-arm is always determined before the Kalman filtering process of GPS/IMU integration (i.e. the offset between the GPS centre and IMU centre has already been compensated during the assembly of the GPS/IMU system), this lever-arm is usually not considered in the positioning equation of MMS for sake of simplicity even though the compensation may incur errors (Hong et al., 2006) mostly in the case of the low-end IMU. Another lever-arm is the distance offset between the centre of image sensor and centre of IMU (a_b^s in Figure 2.5) and is the only lever-arm usually being considered in the positioning equation of MMS. This lever-arm error is generally in the centimetre level. There are basically two alternatives to find out the lever-arm value. The first approach is using the least squares calibration. However, this is not always efficient as the lever-arm has high correlation with other calibration parameters. Consequently, the second method is utilized in most cases to determine the lever-arm. The method is a semi-manual measurement method that combines the mea-

surement from regular measuring tapes and values from the engineering drawings (e.g. AutoCAD drawings) of the GPS/IMU and the imaging sensors. The errors of such a method can be limited within 2 cm (Glennie, 2007b). The impact of the lever-arm error is the existence of constant biases on target positions regardless to the range.

2.2.3 Attitude Errors

An IMU is composed of an inertial sensors assembly (ISA) which contains a common mounting base for the triads of accelerometers and gyros, and the associated electronic circuits that perform signal digitalization and temperature compensation. The drifting errors from the sensors of the ISA, the sensors assembly errors and also the errors associated with the digital signal processing will contribute the overall IMU errors. Based on the discussion of Petrie (2010), an IMU can be classified as one of three types based on the gyros implanted:

1. Ring Laser Gyro (RLG): it is most accurate but also the most costly, mainly for high accuracy application.
2. Fiber Optic Gyro (FOG): it is the most commonly-used in MMS as the accuracy is high with medium cost.
3. Micro Electro Mechanical System (MEMS) based Gyro: it is the least accurate but also has the least cost. Thanks to its lower cost, it is now becoming more popular in MMS for moderate accuracy applications.

IMUs can also be categorized into four grades (VectorNav, 2011). Among them, the highest grade (navigation grade) IMU usually consists of the RLG. Some tactical-grade IMU can also contain RLGs, such as the Honeywell HG1700. Tactical-grade (the second highest grade) IMUs typically contain FOGs or MEMSs. A navigation grade IMU can cost about \$100k USD while the tactical-grade IMUs' costs range from \$5k – \$30k

USD. Applanix Inc. is one of the best known GPS/IMU system integrators, and the accuracy of its IMU products, (e.g. tactical-grade 610 series) have a 0.005° accuracy for roll/pitch, and 0.015° for heading respectively (Applanix, 2011). Another navigation technology company, IGI GmbH, has its AEROcontrol series used by the StreetMapper. The AEROcontrol-III has accuracies of 0.003° for roll/pitch and 0.007° for heading respectively (IGI, 2011).

Apart from the errors associated with the ISA mentioned in the beginning of this section, the errors of the accelerometers and the gyros caused by electronics sensitivity, signal background noises, sensors assembly and etc can also be modelled with stochastic models. More discussion can be found in Grewal et al. (2007).

2.2.4 Positioning Errors

The Global Navigation Satellite System (GNSS) receivers (predominantly, the GPS receivers) with the dual-frequency survey grade or the geodetic grade are used in mobile mapping technology, and the GPS receivers are operated in differential mode, i.e. DGPS, with base stations or global DGPS network services to achieve the sub-decimetre accuracy. Another GPS technology that utilizes the Carrier-Phase DGPS (CP-DGPS) in the real-time is known as Real-Time Kinematic (RTK), and this is also adopted by MMSs. The ProMark3 RTK from Ashtech Inc. is an example (Ashtech, 2011).

The DGPS and RTK accuracies degrade with the distances from the reference baseline/station, and typically the sub-decimetre accuracy of the RTK can be achieved only with limits on the order of 10 km. A large network of dependent reference stations can be set up to simulate a reference station that is close to the receiver, for maintaining centimetre-level accuracy within a wider area. This technique is known as Virtual Refer-

ence Stations (VRS), and it keeps the centimetre-level accuracy with for wider area (up to several 10 km) compared to traditional DGPS or RTK network. Many commercial VRSs has been developed, e.g. Trimble (2011). For more information about the VRS, see Vollath et al. (2000). The GPS errors are not explained in detail here but are classified and listed as the following three groups (Samama, 2008):

1. Synchronization Errors: satellite and receiver synchronization errors
2. Propagation Errors: errors due to propagation in the ionosphere and the troposphere; multipath
3. Location Errors: satellite geometry

The current accuracy of relative kinematic DGPS/INS for TITAN can reach $2 \text{ cm} + 1 \text{ ppm}$ of the baseline length in both horizontal and vertical directions (Glennie, 2007b).

2.2.5 Scanner Component Errors

The modelling of the systematic errors of the TLS can be classified into two main groups Lichti (2007). The first is referred to as the modelling with the basic additional parameters groups inherited from total stations, as the TLS share several common properties in their architecture. The other group is the empirical parameters which models errors associated with seemingly unapparent physical causes. Such modelling can be complicated and involves many parameters. In MMS, the modelling of the TLS systematic error is usually simplified due to the fact that the architecture of 2D scanners are simpler than that of 3D scanners. Many imaging systems in MMSs are the 2D line TLSs which contain one scanning angle rotation (encoder angle) and support the model's simplification. However, the model of scanner component varies for different TLS systems. For example the error modelling of Velodyne HDL-64E S2 is totally different from that of the 2D Line

scanner (Glennie and Lichti, 2010). In general, the rangefinder (ρ) and encoder angle (θ) errors are modelled as the following:

$$\rho_{real}(t) = \rho_{obs}(t) + \Delta\rho \quad (2.4)$$

$$\theta_{real}(t) = \theta_{obs}(t) + \Delta\theta \quad (2.5)$$

where,

$\Delta\rho$ and $\Delta\theta$ are constant biases.

The range error of modern TLSs varies from several millimetres to several centimetres, and it is dependent of the range. While the encoder error will usually stay from sub-minutes to sub-degree level. Accuracies of some common TLS used in MMS are summarized in Table 2.2.

Table 2.2: Common TLS used in MMSs and their range accuracy (range dependent)

MMS	TLS	Range Accuracy (mm)
TITAN	Riegl MLS-Q120	25
StreetMapper	Riegl VQ-180	15
Mitsubishi MMS Series	SICK LMS 291	10
Riegl VMX-250	VZ-400	5

The encoder angle errors might include an additional scale factor term (s_θ in Equation 2.6) if the mirror in the laser system is subject to positional shift due to the torsions caused by its high accelerations during the oscillating scanning mechanisms (Katzenbeisser, 2003).

$$\Delta\theta = \Delta\theta_0 + s_\theta \theta(t) \quad (2.6)$$

where, θ_0 is the zero-offset constant bias.

Another error source associated with ρ and θ is the divergence of the laser beam. The divergence of the laser beam for a static TLS increase as the magnitude of ρ_{obs} , and it can be modelled appropriately under the assumptions that the beam cross-section is circular and has a definite radius and the probability governing the angular position of the range measurement is uniform within the beamwidth (Lichti, Gordon, and Tipdecho, Lichti et al.). For the MMS in on-the-fly mode, the divergence errors might be more complicated as the effect of the kinematic scanning has to be considered in the models.

In conclusion, the GPS errors are dependent on multiple external factors (e.g. GPS geometry, atmospheric condition and etc) and thus also location dependent, therefore, both errors from the position and orientation measurement from the GPS/IMU are excluded in the calibration of this work. In addition, the lever-arms and the encoder angles offsets are not usually solved by the least-squares due to the fact that high correlations exists between them and the input measurements (GPS position and orientation measurement) and thus they are excluded in the calibration of this work. The rangefinder offset is also excluded as in Skaloud and Lichti (2006) showing that the rangefinder offset ($\Delta\rho$) incurs problems of high correlation with the plane parameter and the estimated values are not realistic when no control points are used in the calibration. As a result, only calibration of the three boresight angles will be focused on this thesis. In next Chapter, the full position equation of the MMS is presented and in Chapter 4, the mathematical models that combined the full positioning equation of the MMS and also the geometric features are given and implemented with the least-square algorithm.

Chapter 3

The Positioning Equation of the MMS

In this Chapter, the full positioning equations for MMS and TITAN are introduced. The background of TITAN and the orientation of each scanner of TITAN will be also discussed.

3.1 Introduction to the Full Positioning Equation for the MMS

In Chapter 2, the simplified position equation of the MMS was briefly described. Before discussing the mathematical models for the calibration, the full position equation of the MMS will be first thoroughly discussed in this section as it is the main component of the calibration models. The position equation is the fundamental equation of direct geo-referenced measurement and also the core mathematical model for MMS since the presence of first generation of camera-based MMS. Its principle is derived from that of ALS (Baltsavias, 1999), which is basically the vector sum of the transformations of measurements from imaging sensors and also measurements from the GPS/INS into a common mapping frame. The transformation is straightforward, however, it can be broken down into multiple transformations which are associated with independent sources of measurement errors and they have been already been elicited in Chapter 2.

Figure 3.1 depicts the summation of vectors in the mapping frame for the full position equation of MMS, which is given as the following:

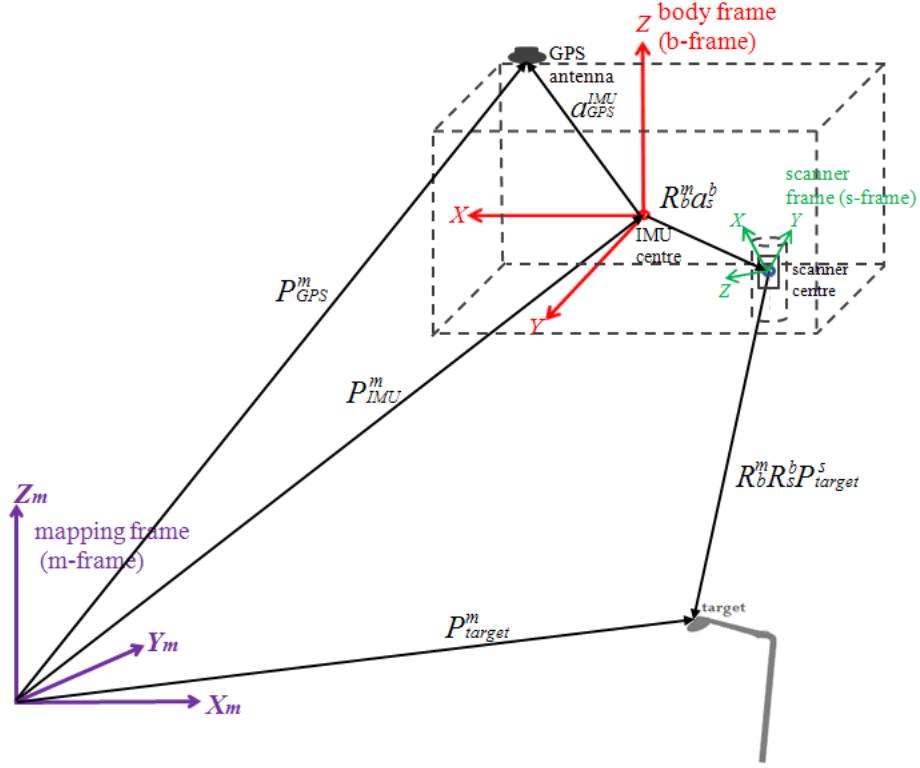


Figure 3.1: The full positioning equation of the MMS

$$\begin{aligned}
 P_{target}^m(t) &= \begin{bmatrix} X(t) \\ Y(t) \\ Z(t) \end{bmatrix}_m \\
 &= P_{GPS}^m(t) - a_{GPS}^{IMU} + R_b^m(t)a_s^b + R_b^m(t)R_s^b P_{target}^s(t) \\
 &= P_{GPS}^m(t) - a_{GPS}^{IMU} + R_e^m R_l^e(t)R_b^l(t)a_s^b + R_e^m R_l^e(t)R_b^l(t)R_s^b P_{target}^s(t) \\
 &= P_{IMU}^m(t) + R_e^m R_l^e(t)R_b^l(t)a_s^b + R_e^m R_l^e(t)R_b^l(t)R_s^b P_{target}^s(t) \quad (3.1)
 \end{aligned}$$

where,

$P_{target}^m(t)$ is the position vector of the target in the mapping frame;

$P_{GPS}^m(t)$ is the position vector of the GPS receiver in the mapping frame;

$P_{IMU}^m(t)$ is the position vector of the IMU centre in the mapping frame;

a_{GPS}^{IMU} is the lever-arm between the GPS receiver and the IMU centre;

$R_b^m(t)$ is the rotation matrix from the body frame to the mapping frame;

a_s^b is the lever-arm between the IMU centre and the scanner centre;

R_s^b is the rotation matrix from the sensor frame to the body frame;

$P_{target}^s(t)$ is the position vector of the target in the sensor frame;

R_e^m is the rotation matrix from the ECEF frame to the mapping frame;

$R_l^e(t)$ is the rotation matrix from the local-level frame to the ECEF frame;

$R_b^l(t)$ is the rotation matrix from the body frame to the local-level frame;

t is the epoch.

The expanded form of Equation 3.1 shows that the position of the target in the mapping frame is actually the sum of following three terms: (1) the measurement from the scanner, rotated from the sensor frame to the mapping frame; (2) the lever-arm between the sensor-frame and the body-frame (a_s^b) rotated from the body-frame to the mapping frame; and (3) the absolute position of the IMU centre calculated by offsetting the lever-arm (a_{IMU}^{GPS}) between the GPS receiver and the IMU centre. Note that there is no scale factor for any term of Equation 3.1 because the range measurement determine the scale.

3.1.1 Transformation from the Sensor Frame (s-frame) to the Body Frame (b-frame)

The transformation (Figure 3.2) from the sensor frame to the body frame involves a rotation (R_s^b) and a translation (a_s^b). The sensor frame or the scanner frame refers to the right-handed 3D Cartesian space with the sensor's centre (the position where laser beams are emitted) as its origin. It is equivalent to the scanner space of static TLSs. The scanners embedded in MMSs are usually 2D line scanners with their laser beams deflecting only in one dimension to acquire 2D data. Since the 2D scanning is performed on moving platforms along a particular direction, 3D scanning of objects can be achieved and thus point clouds can be collected. The scanners usually involve two measurement quantities: range (ρ) and encoder angle (θ). The measured position can be given as 3×1

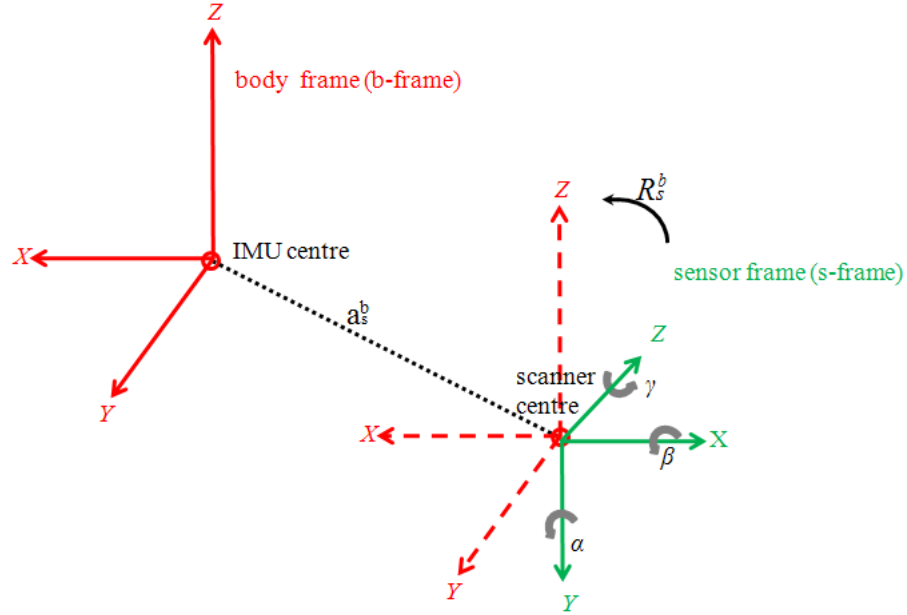


Figure 3.2: Transformation from the Sensor Frame (s-frame) to the Body Frame (b-frame)

column vectors with different combinations of $\pm\rho\sin\theta$ or $\pm\rho\cos\theta$ in either the $x-z$ plane or the $y-z$ plane depending on different scanners or settings. The following equation shows an example of the scanner column vector in the $x-z$ plane (Figure 3.3):

$$P_{target}^s(t) = \begin{bmatrix} \rho(t) \cos\theta(t) \\ 0 \\ \rho(t) \sin\theta(t) \end{bmatrix} \quad (3.2)$$

The scanner vector is thereafter rotated into the body frame (Figure 3.2) by the rotation

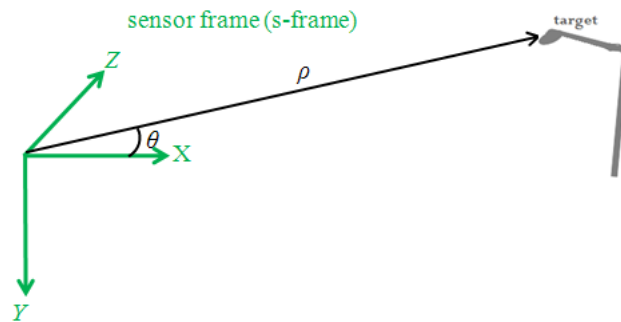


Figure 3.3: The range and the encoder angle measurements of the 2D-Line scanner

matrix R_s^b that is a function of the boresight angles (α , β and γ). The body frame refers to a right-handed 3D Cartesian space with the IMU centre as its origin, and it is the 3D space with respect to the MMS system body. R_s^b can be broken down into three basic rotational matrices which rotate the scanner vector about the x , y and z axes of the sensor space. The sequence of the the three rotations of R_s^b is not unique and an example is given as the following:

$$R_s^b = R_3(\gamma)R_1(\beta)R_2(\alpha) \quad (3.3)$$

The body frame for the MMS is commonly defined as in Figure 3.4, e.g. El-Sheimy (1996) for matching the use of the ENU as the local-level frame. After the rotation, a

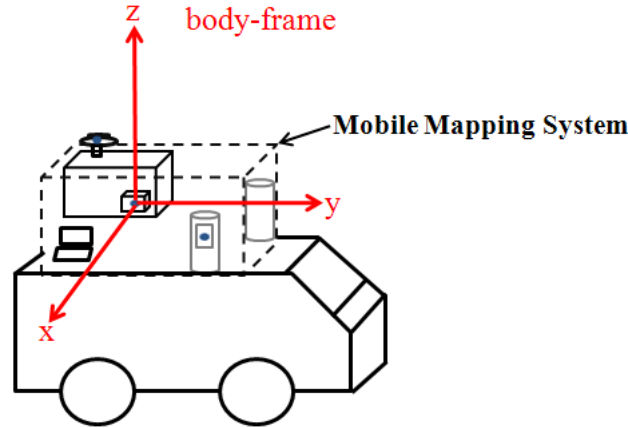


Figure 3.4: Commonly-defined body frame (b-frame) of the MMS

translation of the lever-arm offset (a_s^b) is applied which will lead to the coincidence of the origin of the transformed s-frame with the b-frame that involves the IMU measurement.

3.1.2 Transformation from the Body Frame (b-frame) to the Local-level Frame (l-frame)

The local-level frame generally refers to a local 3D Cartesian coordinate system, usually either the East-North-Up (ENU) or the North-East-Down (NED) coordinate system (Figure 3.5). Both the ENU and NED are a local tangent plane (LTP) coordinate system with an origin which is not unique. The $x - y$ plane of an ENU system is a tangential

surface of a point which is on or above the ellipsoid with its x , y and z axes pointing towards east, north and along the ellipsoid normal (upward), respectively. On the contrary, the NED system has its x , y and z axes pointing towards north, east and along the ellipsoid normal (downward) respectively. The ALS usually takes the NED as the local-level frame as its scanning geometry is nadir-looking while MMSs will mostly take the ENU. The IMU measures the attitude (roll, pitch and yaw) of the navigating plat-

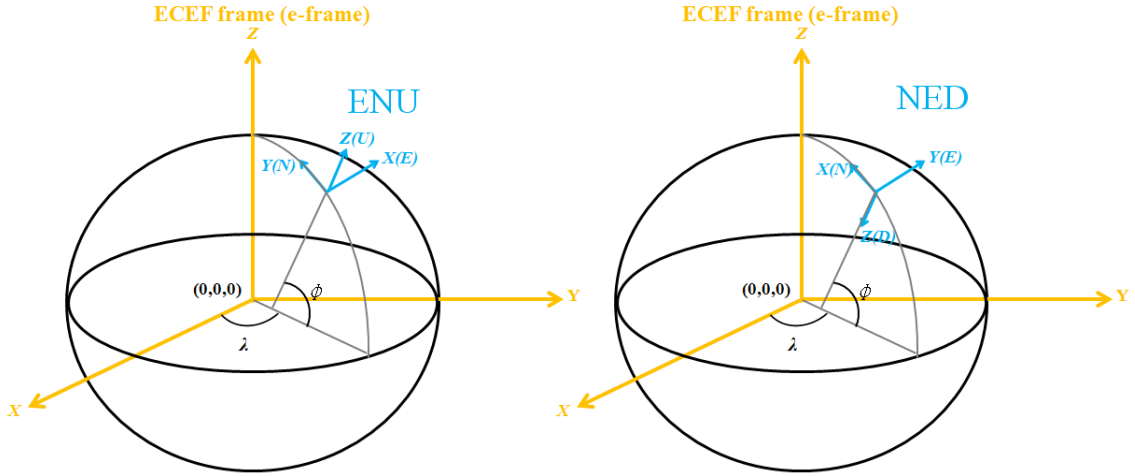


Figure 3.5: The East-North-Up (ENU) or the North-East-Down (NED) coordinate systems

form, i.e. the Euler angles between the body frame and the local-level frame. In other words, $R_b^l(t)$ is a function of the roll, pitch and yaw, for rotation from the body frame to the local-level frame. For rotating the body-frame to an ENU frame, $R_b^{l(ENU)}(t)$ can be defined as the following:

$$R_b^{l(ENU)}(t) = R_3(y(t))R_1(p(t))R_2(r(t)) \quad (3.4)$$

where, $r(t)$, $p(t)$ and $y(t)$ are the roll, pitch and yaw, respectively.

The origin of the ENU system coincides with the origin of the body frame (the IMU centre). The position and attitude vary as the platform moves and thus the ENU is

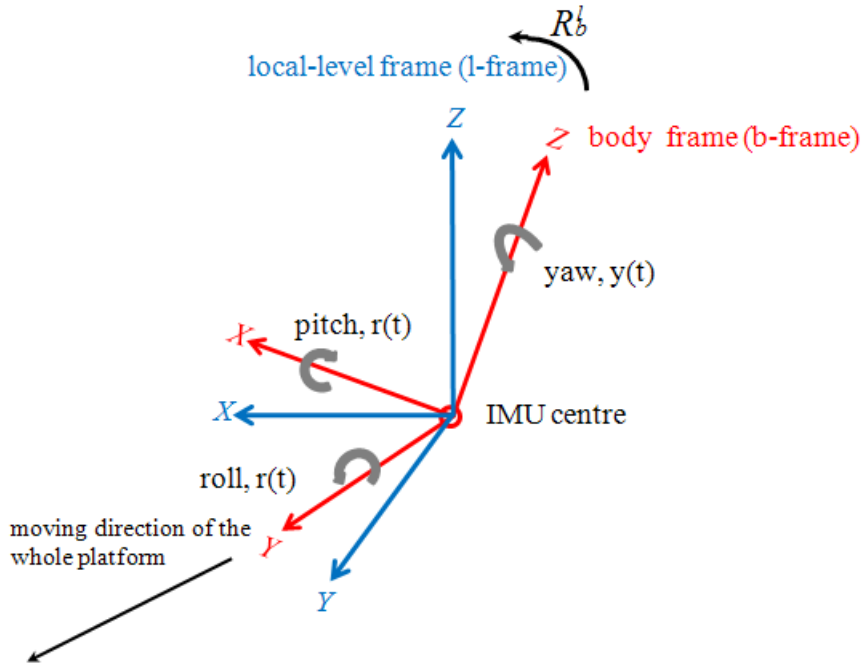


Figure 3.6: The rotation from the body-frame (b-frame) to the local-level frame (l-frame) - ENU

repeatedly defined with different origins during the movement of the platform (Figure 3.6). However, the x , y and z axes always point to east, north and upward respectively, regardless of the positions of the origin.

3.1.3 Transformation from the Local-level Frame (l-frame) to the Earth-centred, Earth-fixed Frame (e-frame)

The Earth-centred, Earth-fixed frame (ECEF) is also known as the Conventional Terrestrial System (CTS). The ECEF (Figure 3.7) is a right-handed Cartesian system with its origin at the centre of mass of the Earth. Its x -axis points to the mean Greenwich meridian ($\lambda = 0^\circ$) and its z -axis points to the Conventional International Origin (CIO) which is an average location of the pole of the Earth's rotation. Unlike the ENU or the NED systems, the ECEF is a unique system regardless to locations as its origin is always at the centre of mass of the earth. For more information about ECEF, see Xu

(2007). $R_i^e(t)$ rotates the space vector from the local-level frames (l-frame) at different

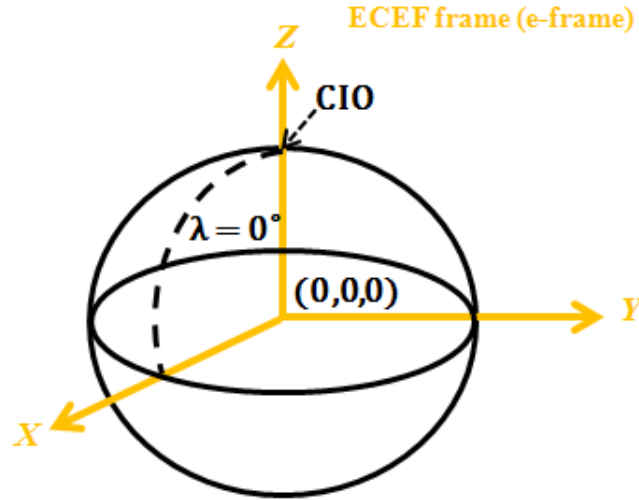


Figure 3.7: The Earth-centred, Earth-fixed frame/coordinate system

epochs (t_1, t_2, t_3, \dots) to the ECEF-frame (e-frame) as shown in Figure 3.8 and basically the rotation is a two-step rotation process. This is illustrated in Figures 3.9 and 3.10 for ENU and NEU respectively. The latitude and longitude of the IMU centre at epoch (t) determine the rotation angles of the two rotation matrices. The equation for the rotation from the ENU to the ECEF frame is given as the following equation:

$$R_{i(ENU)}^e(t) = R_3 \left(-\frac{\pi}{2} - \lambda(t) \right) R_1 \left(-\frac{\pi}{2} + \phi(t) \right) \quad (3.5)$$

The equation for the rotation from the NED to the ECEF frame is given as follows:

$$R_{i(NED)}^e(t) = R_3 (-\lambda(t)) R_2 \left(\frac{\pi}{2} + \phi(t) \right) \quad (3.6)$$

3.1.4 Transformation from the Earth-centred, Earth-fixed Frame (e-frame) to the Mapping Frame (m-frame)

The measurements are eventually transformed from the e-frame into a mapping frame (m-frame) as final survey products (Figure 3.11). The mapping frame can be a national

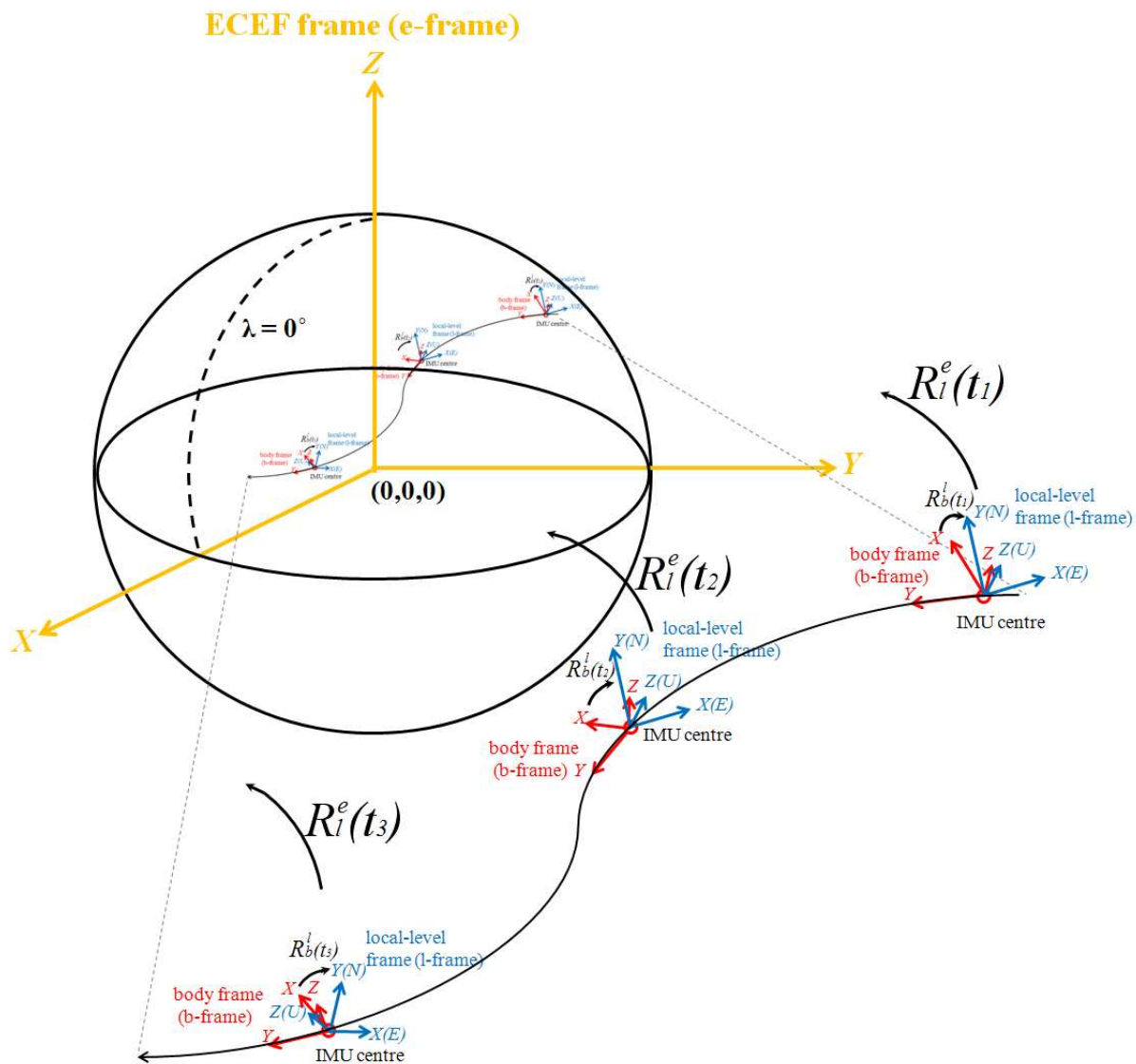


Figure 3.8: The rotation from the different local-level frames (ENUs) at different epochs, t_1, t_2, t_3 to the Earth-centred, Earth-fixed frame (e-frame)

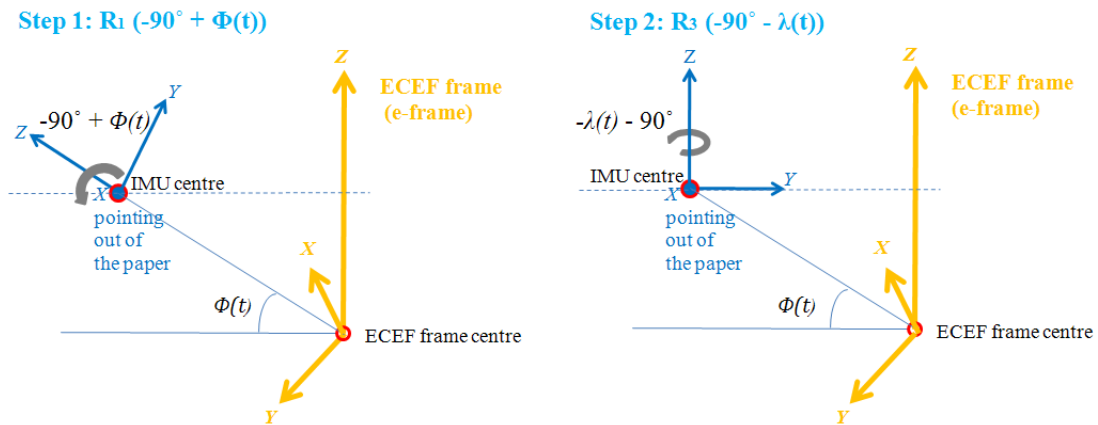


Figure 3.9: The rotation from the ENU to the ECEF frame

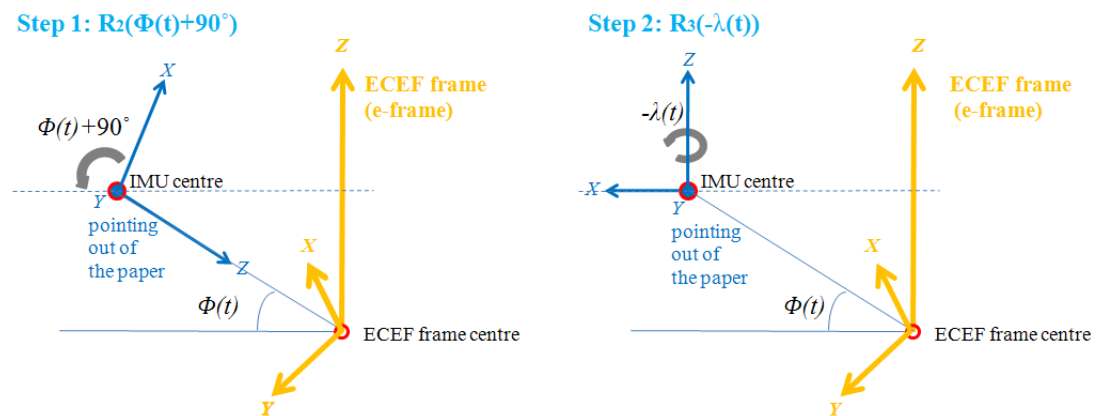


Figure 3.10: The rotation from the NED to the ECEF frame

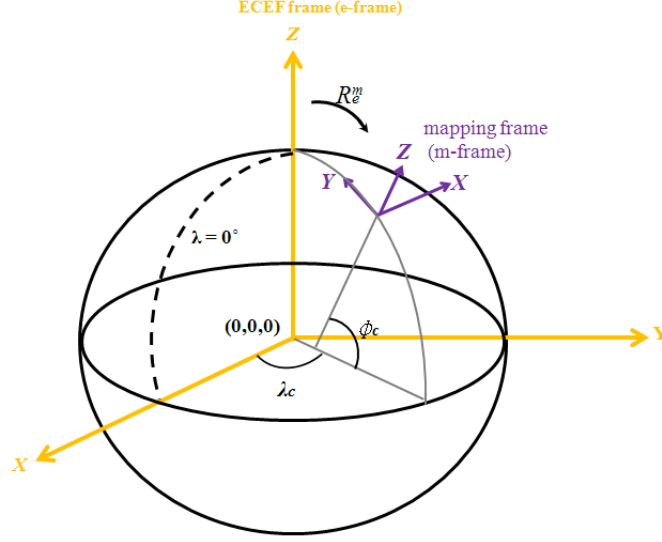


Figure 3.11: The rotation from the Earth-centred, Earth-fixed frame (e-frame) to mapping frame (m-frame)

coordinate system such as Universal Transverse Mercator (UTM), ENU, NED or others. To transform from the e-frame to either the ENU or the NED, the centroid of the captured point clouds in terms of the latitude and longitude (ϕ_c , λ_c) is first computed as the origin. The equation for rotation from ECEF to ENU is given as below:

$$R_e^{l(ENU)} = [R_{l(ENU)}^e(\phi_c, \lambda_c)]^T \quad (3.7)$$

$$= R_1\left(\frac{\pi}{2} - \phi_c\right) R_3\left(\frac{\pi}{2} + \lambda_c\right) \quad (3.8)$$

The equation for rotation from ECEF to NED is given as below:

$$R_e^{l(NED)} = [R_{l(NED)}^e(\phi_c, \lambda_c)]^T \quad (3.9)$$

$$= R_2\left(-\frac{\pi}{2} - \phi_c\right) R_3(\lambda_c) \quad (3.10)$$

3.2 Background of the TITAN and its Full Positioning Equation

The MMS being investigated in this research is called TITAN (Figure 3.12), which is the acronym of Tactical Infrastructure and Terrain Acquisition Navigator system. It was

solely developed by the Terrapoint Inc. in 2007. The previous generation of the TITAN was named SideSwipe and it was built by the same company in 2005 for road surveys and mapping in Afghanistan. SideSwipe was basically a modified version of an airborne laser scanning system from the same company with only one scanner and a tactical grade IMU. The TITAN incorporated four 2D-line TLSs (Riegl LMS-Q120) and also an upgraded tactical grade IMU (Honeywell HG1700) and thus has overcome the limitation of the multiple-pass scanning required by the SideSwipe which contained one TLS, the limited accuracy of the tactical-grade IMU and also the limited field of view (FOV) of 60° (Shan and Toth, 2009). The NovAtel OEM-4 GPS receiver is also integrated with the system. Moreover, the TITAN is built with a transferable compact blackbox that can be flexibly mounted on different moving platforms(e.g trucks, Figure 3.13), while SideSwipe and even some other current popular MMSs cannot. Apart from this, up to four digital cameras/video cameras are also equipped with the system. The TITAN can generate point clouds with a density of 40 points/m² when the MMS is moving at 80 km/hr. The typical measurement range can reach 150 m. For the system assembly, two of the



Figure 3.12: The TITAN System

scanners are mounted on each side of the system blackbox (left and right sides), while the other two are mounted at their back and the laser beams are set pointing upward and downward (Figure 3.14). The sensor frames of each of the four scanners and also the common body frame of the system are shown in Figure 3.15 (the effect of the negative



Figure 3.13: The TITANs mounted on the hydraulic racks built on trucks

sign of ρ (Equation 3.11) is considered). This configuration can maximize the coverage

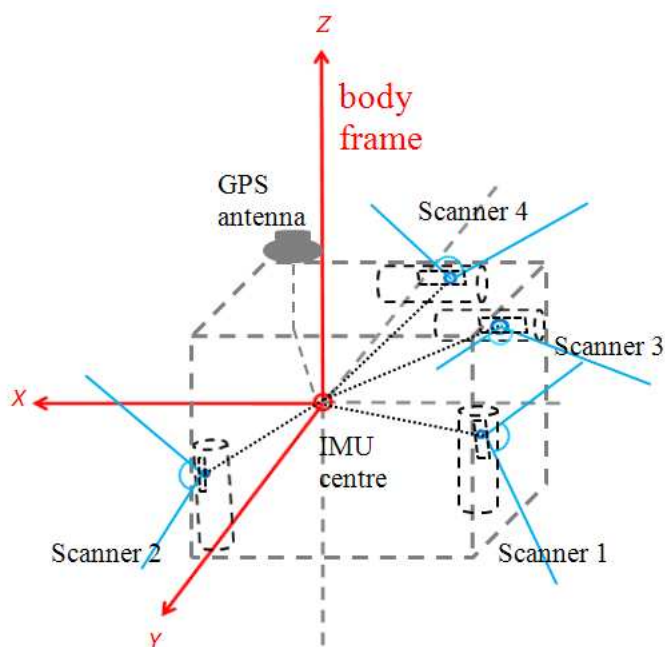


Figure 3.14: The TITAN system assembly

of the scan space to 360° . In this thesis, scanners pointing to the left, right, down and up sides are defined as Scanners 1, 2, 3 and 4, respectively. There are only small overlap areas between Scanner 1, 3 and 4 and also between Scanner 2, 3 and 4. Figure 3.16 is a plot of simulated TITAN scanning coverage of the four scanners. The scanning ranges are from 4.8 m to 8.75 m, and the FOVs of all four scanners are set to 80° (the Riegl LMS-Q120's maximum value), and also the boresight angles and lever-arms are provided

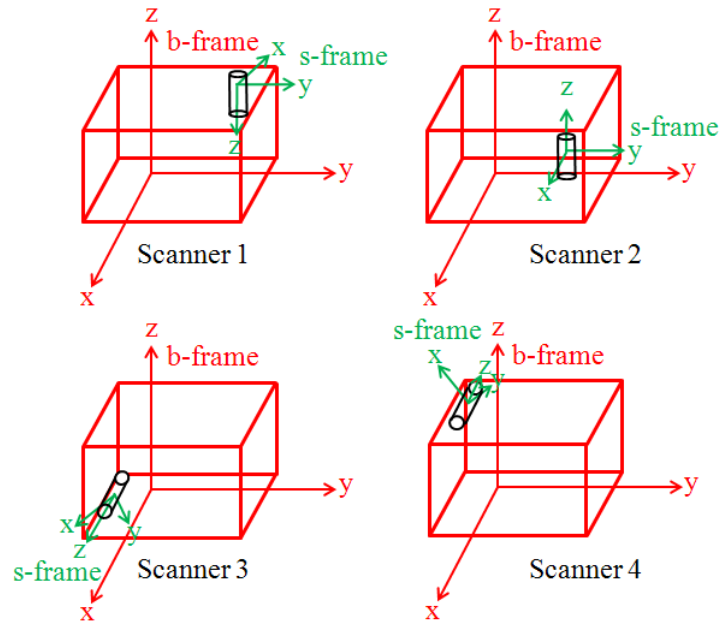


Figure 3.15: Scanner orientation

by Terrapoint. It can be seen that the overlap areas of the scanners are quite limited but 360° coverage is guaranteed. More discussion about the overlap of the scanning can be found in Hefford et al. (2009).

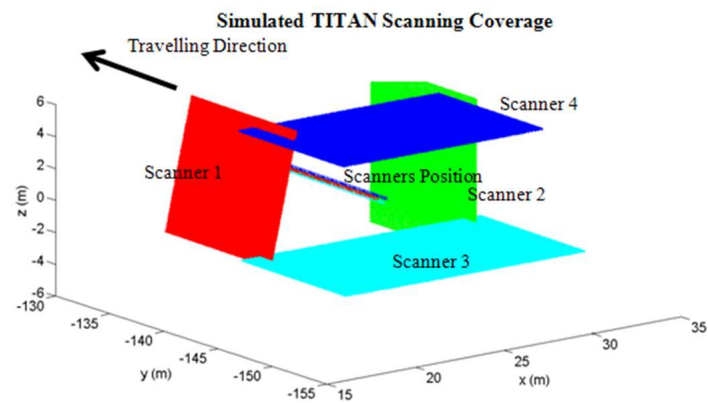


Figure 3.16: Simulated TITAN scanning coverage

The four scanners share the same positioning equation but with different boresight angles and lever-arm values. Based on Equation 3.1, the position equation for TITAN is given as the following:

For scanner s_n ,

$$\begin{aligned}
& \begin{pmatrix} X_{ENU_0} \\ Y_{ENU_0} \\ Z_{ENU_0} \end{pmatrix} = \begin{pmatrix} X(t) \\ Y(t) \\ Z(t) \end{pmatrix}_{m(ENU_0)} \\
& = R_e^{m(ENU_0)} \left\{ \left[\begin{pmatrix} X_I(t) \\ Y_I(t) \\ Z_I(t) \end{pmatrix}_e + R_{l(ENU)}^e(t) R_b^{l(ENU)}(t) \left(R_s^b T_s \begin{pmatrix} -\rho(t) \cos\theta(t) \\ 0 \\ -\rho(t) \sin\theta(t) \end{pmatrix}_s \right. \right. \\
& \qquad \qquad \qquad \left. \left. + \begin{pmatrix} l_{x_{s_n}} \\ l_{y_{s_n}} \\ l_{z_{s_n}} \end{pmatrix}_b \right) \right] - \begin{pmatrix} X_c \\ Y_c \\ Z_c \end{pmatrix}_e \right\} \\
& = \begin{pmatrix} X_I(t) \\ Y_I(t) \\ Z_I(t) \end{pmatrix}_{m(ENU_0)} + R_e^{m(ENU_0)} R_{l(ENU)}^e(t) R_b^{l(ENU)}(t) \left[R_s^b T_s \begin{pmatrix} -\rho(t) \cos\theta(t) \\ 0 \\ -\rho(t) \sin\theta(t) \end{pmatrix}_s + \begin{pmatrix} l_{x_{s_n}} \\ l_{y_{s_n}} \\ l_{z_{s_n}} \end{pmatrix}_b \right]
\end{aligned} \tag{3.11}$$

where,

$$T_s = \begin{pmatrix} 0 & 0 & -1 \\ 0 & 1 & 0 \\ 1 & 0 & 0 \end{pmatrix} \text{ is the a-priori known rotation matrix within the s-frame;}$$

$R_s^b = R_3(\gamma_{s_n}) R_1(-\beta_{s_n}) R_2(-\alpha_{s_n})$ is the rotation matrix from the s-frame to the b-frame,

and $\alpha_{s_n}, \beta_{s_n}, \gamma_{s_n}$ are the boresight angles about the y, x and z -axes respectively;

$R_b^{l(ENU)}(t) = R_3(y(t))R_1(-p(t))R_2(-r(t))$ is the rotation matrix from the b-frame to the l-frame, and $r(t), p(t), y(t)$ are the roll, pitch and yaw about the y, x and z -axes respectively;

$R_{l(ENU)}^e(t) = R_3(-\frac{\pi}{2} - \lambda(t))R_1(-\frac{\pi}{2} + \phi(t))$ is the rotation matrix from the l-frame to the e-frame, and $\phi(t), \lambda(t)$ are the latitude and longitude of $X_I(t), Y_I(t), Z_I(t)$;

$R_e^{m(ENU_0)} = R_1(\frac{\pi}{2} - \phi_c)R_3(\frac{\pi}{2} + \lambda_c)$ is the rotation matrix from the e-frame to the m-frame, $\phi(t), \lambda(t)$ are the latitude and longitude of X_c, Y_c, Z_c ;

$R_1(\Theta) = \begin{pmatrix} 1 & 0 & 0 \\ 0 & \cos(\Theta) & \sin(\Theta) \\ 0 & -\sin(\Theta) & \cos(\Theta) \end{pmatrix}$ is the 3D rotation matrix about the x -axis;

$R_2(\Theta) = \begin{pmatrix} \cos(\Theta) & 0 & -\sin(\Theta) \\ 0 & 1 & 0 \\ \sin(\Theta) & 0 & \cos(\Theta) \end{pmatrix}$ is the 3D rotation matrix about the y -axis;

$R_3(\Theta) = \begin{pmatrix} \cos(\Theta) & \sin(\Theta) & 0 \\ -\sin(\Theta) & \cos(\Theta) & 0 \\ 0 & 0 & 1 \end{pmatrix}$ is the 3D rotation matrix about the z -axis;

$X_I(t), Y_I(t), Z_I(t)$ are GPS positions of the IMU centre of the GPS/IMU;

X_c, Y_c, Z_c are centroid of all the points of the data set;

$lx_{s_n}, ly_{s_n}, lz_{s_n}$ are the lever-arm between the scanner s_n and the IMU centre;

$\rho(t), \theta(t)$ are the range and the encoder angle respectively;

t is the epoch.

The TITAN position equation is basically very similar to the general one (Equation 3.1). The significant differences are that the rotation is in negative directions for α and β , roll (r) and pitch (p), and the mounting matrix T_s exists. The role of the T_s matrix is equal to a rotation about the y axis with 90° and it helps simplifying the system design. T_s is not unique and is system dependent. Since the positioning equation involves the translation by the lever-arm, the least-square adjust should be perform in Cartesian coordinates system with a local origin, e.g. ENU. Thus the GPS position of the IMU centre should be transformed to ENU by using the centroid of the whole data set as given in the first term of Equation 3.11

Accordingly, the terms, X_{ENU_0} , Y_{ENU_0} , Z_{ENU_0} from Equation 3.11 are substituted to the geometric models of the features presented in the next Chapter to form the functional models for the calibration adjustment.

Chapter 4

The Calibration Models and the Least-Squares Implementation

4.1 Mathematical Model for Feature-based Self-Calibration

The previous works for the boresight calibration using planar features have been discussed in detail in Chapter 1. The mathematical model for the feature-based self-calibration is based on the principle that the 3D equation of each type of geometric feature is augmented with the x , y and z terms of the full position equation (Equation 3.11). The boresight angles and also the features' parameters are then set to be unknowns. Meanwhile, the GPS/IMU observed values, i.e. the position $(X_I(t), Y_I(t), Z_I(t))$ and the orientation angles $(r(t), p(t), y(t))$, as well as the scanners' observed quantities, range $(\rho(t))$ and encoder angle $(\theta(t))$ are set as observation terms for the Gauss-Herlmert (combined) model least-square adjustment. Through the adjustment process, the boresight angles, along with the features' parameters are estimated in a way such that the minimization of the variation function (the sum of weighted squares of residuals) are achieved. In other words, a set of optimal boresight angles are estimated in such a way that the feature models best fits the groups of points lying on the features. Two types of geometric features are used in this work: planar and catenary features. They are used to calibrate the boresights separately (plane-based calibration and catenary-based calibration) and also simultaneously (mixed-feature based calibration). For the latter, the four sets of boresights, along with the parameters of the planes and the catenaries are estimated such that all the geometric models best fit the input data points.

4.1.1 Mathematical Model for Plane-based Calibration

4.1.1.1 Background

Planar features are the most abundant geometric features that appear in most of the survey sites. Buildings usually contain planar features as their façades and roofs, and architectures other than buildings such as road and bridge surfaces are also bountiful with planar features. The good availability of the planar features is one of the reasons for static TLS self-calibration (Bae and Lichti, 2007; Glennie and Lichti, 2010; Chow et al., 2011) and also boresight self-calibration works in ALS (Filin, 2003; Skaloud and Lichti, 2006) and MMS (Rieger et al., 2010).

The 3D equation for a plane is defined by the unit normal vector $(a \ b \ c)$ and d where a , b , c are the direction cosines of the plane and d is the orthogonal distance of the plane from the origin. For an arbitrary point (x_1, y_1, z_1) lying on a plane, we have:

$$(a \ b \ c) \cdot \begin{pmatrix} x - x_1 \\ y - y_1 \\ z - z_1 \end{pmatrix} = 0 \quad (4.1)$$

$$ax + by + cz - (ax_1 + by_1 + cz_1) = 0$$

Since $(a \ b \ c)$ is the the unit normal vector,

$$\begin{pmatrix} x_1 \\ y_1 \\ z_1 \end{pmatrix} = d \begin{pmatrix} a \\ b \\ c \end{pmatrix} \quad (4.2)$$

then,

$$ax + by + cz - (a \ da + b \ db + c \ dc) = 0$$

which yields,

$$ax + by + cz - d(a^2 + b^2 + c^2) = 0$$

and since the length of the unit vector is equal to one, we get:

$$ax + by + cz - d = 0 \tag{4.3}$$

where,

$$a^2 + b^2 + c^2 = 1 \tag{4.4}$$

4.1.1.2 Functional Model

Augmenting Equation 4.3 with the ENU position vector from Equation 3.11 in Chapter 3 and adding the subscripts $_p$ to the plane parameters to distinguish them from the catenary parameters, we have:

$$f : f_p(\vec{x}, \vec{l}) = a_p X_{ENU_0} + b_p Y_{ENU_0} + c_p Z_{ENU_0} - d_p = 0 \tag{4.5}$$

and along with the functional model, the plane constraint model is given as the following:

$$g_p(\vec{x}) = a_p^2 + b_p^2 + c_p^2 - 1 = 0 \tag{4.6}$$

4.1.2 Mathematical Model for Catenary-based Calibration

4.1.2.1 Background

Apart from planar surfaces, hanging cables are also very commonly-found structures that are mathematically well-defined geometric features in modern cities. If a hanging cable is supported at each end and loaded only by its own weight, its 3D shape can be classified as a catenary feature. In the realm of ALS and MMS, these features have been investigated intensively in terms of their 3D point clouds, for examples, the detection and segmentation of transmission lines with ALS point cloud by McLaughlin (2006), and

the reconstruction of transmission lines with airborne LiDAR data by Jwa and Sohn (2009). More examples are power-line scene classification (Kim and Sohn, 2011), the estimation of the height of hanging cables for road safety purposes with the StreetMapper system developed by Kremer and Hunter (2007), the assessment of LiDAR accuracy of the Optech system using transmission wires (Ussyshkin and Smith, 2007) and power line asset management (Ussyshkin et al., 2011).

4.1.2.2 3D Catenary Model

Among the current publications related to catenary point clouds, none of them use catenary features for sensor or system calibration. In this section, a proposed methodology for boresight calibration will be discussed based on an 3D equation of catenary that has been recently proposed by the author in Chan and Lichti (2011). The rotation angle about the z -axis and also the perpendicular distance between the catenary and the origin at the xy -plane, have been shown to always have high correlation with the catenary shape parameters. Therefore, the 3D catenary was explicitly modelled with a new variable, u , which is defined as the distance from the centroid of the xy -coordinates of the curve. It is known from regression that the centroid lies on the best-fit straight line for the catenary. The proposed 3D equation of catenary is given as the following:

$$z = a + c \left(\cosh \left(\frac{u - b}{c} \right) - 1 \right) \quad (4.7)$$

where,

$$u = \pm \sqrt{(x - x_m)^2 + (y - y_m)^2} \quad (4.8)$$

and

a is the translation parameter from the origin along the z axis;

b is the translation parameter from the origin along the projected u axis;

c is the scaling factor that is governed by the ratio between the tension at the cable's vertex and the weight of the cable per unit length;

(x_m, y_m) are the centroid co-ordinates of the catenary in $x - y$ plane.

The previous works on the catenary objects mainly adopted a two-step approach to fit the point clouds first with the 2D line equation and then the 2D catenary equation. For example, Ussyshkin and Smith (2007) first determine the azimuth of a power line by first fitting a straight line to the x and y coordinates. Then, the transformed x and z coordinates are used to solve the conventional 2D equation of the catenary curve. Jwa and Sohn (2009) first estimate the orientation of the transmission lines using the 2D line equation augmented in the polar coordinate system, followed by the reconstruction based on the 2D catenary model. In both cases, the 3D modelling process was broken down into two 2D processes. This is not sufficient for rigorous calibration since the geometric contributions of x , y , and z are not considered simultaneously in one equation and therefore in one adjustment. Therefore, a 3D equation is essential to rigorous modelling and this is the motivation behind the development of the 3D catenary model (Equation 4.7). The equation is proved to be appropriate in terms of fitting accuracy and parameters correlation with simulated and real catenary data captured by TITAN (Chan and Lichti, 2011).

The motivation of using catenary features is trivial: hanging cables can be easily found in any modern highway and also catenary features provide unique and strong geometry that presumably serves as controls for rigorous calibration. Also, the catenary features can be used when planar features are not always available (e.g. in a rural area). Furthermore, the catenary features can be used along with planar features in one adjustment process when the number of planar features are not sufficient.

4.1.2.3 Symmetry of the Catenary

As shown in Chan and Lichti (2011), fitting the point clouds of highly asymmetric catenaries with the 3D equation will result in extremely high parameter correlations between the b and c parameters. It has been shown that the more asymmetric the catenary, the higher the correlation between b and c . In order to evaluate the degree of the symmetry, the term ΔH_n , the normalized height difference between the two ends of the catenary is defined as the following:

$$\Delta H_n = \frac{\Delta H}{L} \quad (4.9)$$

where,

ΔH is the height difference between the two ends of the catenary;

L is the length of the catenary projected onto the horizontal plane.

It was found by simulation that the correlation coefficient between b and c is a function of both ΔH_n and L (Figure 4.1). For instance, if a 40 m long catenary has $\Delta H_n = 0.05$ m, the the correlation coefficient between b and c will be around 0.95 that will seriously lower the reliability of the adjustment.

4.1.2.4 Functional Model

Equation 4.7 takes the contributions of the x , y and z coordinates into account simultaneously to estimate the parameters by first transforming x and y coordinates into u along the centroid of $x - y$ based on the collinearity of the x and y coordinates of a catenary. The b parameter of the 2D catenary equations is either the x or the y position of the vertex of the catenary, thus it varies readily with the position of catenary, and a and c will vary with b . With the proposed 3D equation, since the x and y coordinates are reduced to the centroid, the parameters a , b and c vary according to the shapes of the

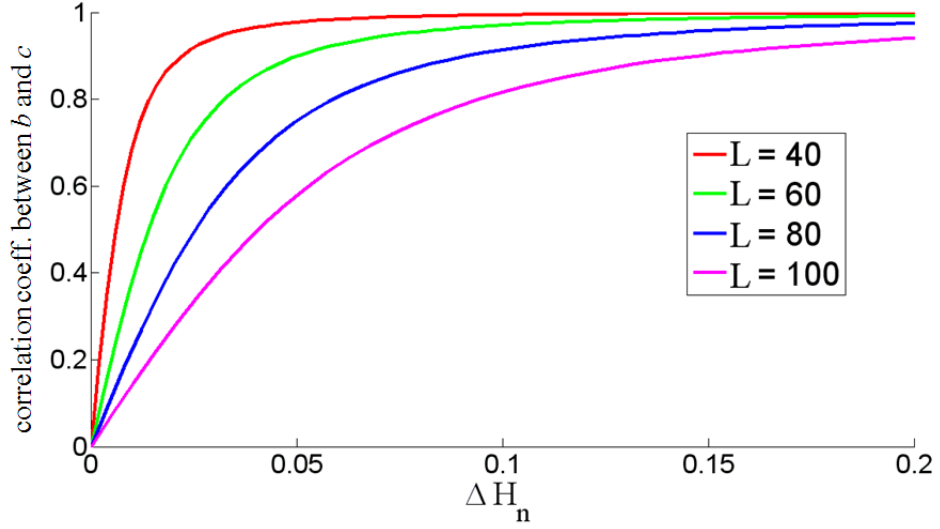


Figure 4.1: Correlation between b and c vs the normalized height difference (between the two ends) of the simulated catenaries (Chan and Lichti, 2011)

catenaries but not the position (while in the case of the 2D catenary, all the parameters are dependent on the location of the catenary). Therefore, the catenaries with the same shape but in different locations will have the same a , b , c . This can definitely save computation power for estimating the initial value of a , b , c when the number of catenaries is getting large.

Augmenting Equation 4.7 with the ENU position vector from Equation 3.11 in Chapter 3 and subscripts c are added to the catenary parameters to distinguish them from the plane parameters, we have:

$$f : f_c(\vec{x}, \vec{l}) = a_c + c_c \left(\cosh \left(\frac{u - b_c}{c_c} \right) - 1 \right) - Z_{ENU_0} = 0 \quad (4.10)$$

where,

$$u = \pm \sqrt{(X_{ENU_0} - x_m)^2 + (Y_{ENU_0} - y_m)^2} \quad (4.11)$$

4.2 Least-Squares Model Implementation

As detailed in Chapter 1, the self-calibration in this work primarily estimates the optimal boresight angles of each scanner by expressing the observation and unknown terms with the direct-georeferencing equation, and then conditioning groups of points lying on certain geometric features (in this work, the planar and catenary features) within a least-square adjustment. Since the observation and the unknown terms are inseparable in the position equations, the combined adjustment model (Wells and Krakiwsky, 1971), also known as the Gauss-Helmert model, is used. The Linearised model for the combined adjustment model can be expressed as the following:

$$A\hat{\delta} + B\hat{v} + w = 0 \quad (4.12)$$

The variation function, φ of the combined adjustment model can be expressed as the following:

$$\varphi = \hat{v}^T P \hat{v} + 2\hat{k}^T (A\hat{\delta} + B\hat{v} + w) \quad (4.13)$$

where,

A is the design matrix of the partial derivatives of the functional model respect to the unknowns;

B is the design matrix of the partial derivatives of the functional model respect to the observations;

P is the weight matrix of the observations;

$\hat{\delta}$ is the correction vector to the unknowns;

\hat{v} is the residual vector of observations;

\hat{k} is the Langrange multiplier vector for the condition;

w is the misclosure vector of the observation.

4.2.1 Normal Equations with the Constraint

For the plane-based calibration, the adjustment will be subject to a constraint that the sum of the squares of the direction cosines equalling one. Therefore, two extra terms for the constraint model (constraint residual and the Lagrange multiplier term) are added to Equation 4.13 as the following:

$$\boldsymbol{\varphi} = \hat{v}^T P \hat{v} + \hat{v}_c^T P_c \hat{v}_c + 2\hat{k}^T (A\hat{\delta} + B\hat{v} + w) + 2\hat{k}_c^T (G\hat{\delta}_c + w_c - \hat{v}_c) \quad (4.14)$$

where,

P_c is weight matrix of the constraint;

\hat{k}_c is the Langrange multiplier vector for the constraint;

G is the design matrix of the plane constraint;

$\hat{\delta}_c$ is the correction vector to the constraint unknowns;

v_c is the residual vector of the plane constraint;

w_c is the misclosure vector of the plane constraint;

The unknowns, \vec{x} can be divided into two group: boresight angles and the plane parameters, and therefore \vec{x} can be broken down into \vec{x}_1 and \vec{x}_2 for boresights and planes' parameters respectively, Equation 4.13 becomes:

$$\boldsymbol{\varphi} = \hat{v}^T P \hat{v} + \hat{v}_c^T P_c \hat{v}_c + 2\hat{k}^T (A_1\hat{\delta}_1 + A_2\hat{\delta}_2 + B\hat{v} + w) + 2\hat{k}_c^T (G\hat{\delta}_2 + w - \hat{v}_c) \quad (4.15)$$

where,

$A_1, \hat{\delta}_1$ are the design matrix and the correction vector of the boresights (\vec{x}_1) respectively;

$A_2, \hat{\delta}_2$ are the design matrix and the correction vector of the plane parameters (\vec{x}_2) respectively.

In order to minimize $\boldsymbol{\varphi}$, the partial derivatives of $\boldsymbol{\varphi}$ with respect to the six vectors:

$\hat{v}, \hat{v}_c, \hat{k}, \hat{k}_c, \hat{\delta}_1$ and $\hat{\delta}_2$ are all set to zero (null vector) and are listed as the following:

$$\frac{\partial \varphi}{\partial \hat{v}} = 2\hat{v}^T P + 2\hat{k}^T B = 0 \quad (4.16)$$

$$\frac{\partial \varphi}{\partial \hat{v}_c} = 2\hat{v}_c^T P + 2\hat{k}_c^T = 0 \quad (4.17)$$

$$\frac{\partial \varphi}{\partial \hat{k}} = 2\hat{\delta}_1^T A_1^T + 2\hat{\delta}_2^T A_2^T + 2\hat{v}^T B + 2w^T = 0 \quad (4.18)$$

$$\frac{\partial \varphi}{\partial \hat{k}_c} = 2\hat{\delta}_2^T G^T + 2w_c^T + 2\hat{v}_c^T = 0 \quad (4.19)$$

$$\frac{\partial \varphi}{\partial \hat{\delta}_1} = 2\hat{k}^T A_1 = 0 \quad (4.20)$$

$$\frac{\partial \varphi}{\partial \hat{\delta}_2} = 2\hat{k}^T A_2 + 2\hat{k}_c^T G = 0 \quad (4.21)$$

Then, the above six equations are divided by two and transposed to form the system of the six equations:

$$\left\{ \begin{array}{l} P^T \hat{v} + B^T \hat{k} = 0 \end{array} \right. \quad (4.22)$$

$$\left\{ \begin{array}{l} A_1^T \hat{k} = 0 \end{array} \right. \quad (4.23)$$

$$\left\{ \begin{array}{l} A_2^T \hat{k} + G^T \hat{k}_c = 0 \end{array} \right. \quad (4.24)$$

$$\left\{ \begin{array}{l} P_c \hat{v}_c - \hat{k}_c = 0 \end{array} \right. \quad (4.25)$$

$$\left\{ \begin{array}{l} A_1 \hat{\delta}_1 + A_2 \hat{\delta}_2 + B \hat{v} + w = 0 \end{array} \right. \quad (4.26)$$

$$\left\{ \begin{array}{l} G \hat{\delta}_2 + w_c - \hat{v}_c = 0 \end{array} \right. \quad (4.27)$$

and then it is arranged in hyper-matrix form as the normal equations:

$$\left[\begin{array}{c|cccc} P^T & 0 & B^T & 0 & 0 & 0 \\ \hline 0 & P_c & 0 & -I & 0 & 0 \\ B & 0 & 0 & 0 & A_1 & A_2 \\ 0 & -I & 0 & 0 & 0 & G \\ 0 & 0 & A_1^T & 0 & 0 & 0 \\ 0 & 0 & A_2^T & G^T & 0 & 0 \end{array} \right] \begin{bmatrix} \hat{v} \\ \hat{v}_c \\ \hat{k} \\ \hat{k}_c \\ \hat{\delta}_1 \\ \hat{\delta}_2 \end{bmatrix} + \begin{bmatrix} 0 \\ 0 \\ w \\ w_c \\ 0 \\ 0 \end{bmatrix} = \begin{bmatrix} 0 \\ 0 \\ 0 \\ 0 \\ 0 \\ 0 \end{bmatrix} \quad (4.28)$$

More than a half of the elements in the coefficient matrix are null matrices and so the direct inversion of the matrix might not be practical. Also, only the estimation of δ_1 and δ_2 are our primary interest. Therefore, the normal equations are necessarily partitioned and simplified. Prior to this, we first investigate the following equation for solving x and y with the normal equations augmented with arbitrary matrices D , E , F and vectors u , v .

$$\left[\begin{array}{c|c} E & D \\ \hline D^T & F \end{array} \right] \begin{bmatrix} x \\ y \end{bmatrix} + \begin{bmatrix} u \\ v \end{bmatrix} = \begin{bmatrix} 0 \\ 0 \end{bmatrix} \quad (4.29)$$

If the Cayley inverse of E exists, then

$$x = -E^{-1}(Dy + u) \quad (4.30)$$

which is then substituted into

$$D^T x + Fy + v = 0 \quad (4.31)$$

to yield

$$(F - D^T E^{-1} D)y + (v - D^T E^{-1} u) = 0 \quad (4.32)$$

so that the coefficient matrix is simplified by eliminating x . As a result, Equation 4.28 can be simplified by eliminating v_c and the simplified equation is given as the following:

$$\left[\begin{array}{c|ccc} P_c & 0 & I & 0 & 0 \\ \hline 0 & -BP^{-1}B^T & 0 & A_1 & A_2 \\ -I & 0 & 0 & 0 & G \\ 0 & A_1^T & 0 & 0 & 0 \\ 0 & A_2^T & G^T & 0 & 0 \end{array} \right] \begin{bmatrix} \hat{v}_c \\ \hat{k} \\ \hat{k}_c \\ \hat{\delta}_1 \\ \hat{\delta}_2 \end{bmatrix} + \begin{bmatrix} 0 \\ w \\ w_c \\ 0 \\ 0 \end{bmatrix} = \begin{bmatrix} 0 \\ 0 \\ 0 \\ 0 \\ 0 \end{bmatrix} \quad (4.33)$$

Eliminations of \hat{v}_c and \hat{k} from Equation 4.33 yield Equation 4.34 and Equation 4.35 respectively:

$$\left[\begin{array}{c|cc} -BP^{-1}B^T & 0 & A_1 & A_2 \\ \hline 0 & -P_c^{-1} & 0 & G \\ A_1^T & 0 & 0 & 0 \\ A_2^T & G^T & 0 & 0 \end{array} \right] \begin{bmatrix} \hat{k} \\ \hat{k}_c \\ \hat{\delta}_1 \\ \hat{\delta}_2 \end{bmatrix} + \begin{bmatrix} w \\ w_c \\ 0 \\ 0 \end{bmatrix} = \begin{bmatrix} 0 \\ 0 \\ 0 \\ 0 \end{bmatrix} \quad (4.34)$$

$$\left[\begin{array}{c|cc} -P_c^{-1} & 0 & G \\ \hline 0 & A_1^T(BP^{-1}B^T)^{-1}A_1 & A_1^T(BP^{-1}B^T)^{-1}A_2 \\ G^T & A_2^T(BP^{-1}B^T)^{-1}A_1 & A_2^T(BP^{-1}B^T)^{-1}A_2 \end{array} \right] \begin{bmatrix} \hat{k}_c \\ \hat{\delta}_1 \\ \hat{\delta}_2 \end{bmatrix} + \begin{bmatrix} w_c \\ A_1^T(BP^{-1}B^T)^{-1}w \\ A_2^T(BP^{-1}B^T)^{-1}w \end{bmatrix} = \begin{bmatrix} 0 \\ 0 \\ 0 \end{bmatrix} \quad (4.35)$$

And finally, \hat{k}_c is eliminated from Equation 4.35 to give Equation 4.36, which is the normal equation that solves only $\hat{\delta}_1$ and $\hat{\delta}_2$. One can notice that the contribution of the constraint linearized model is added to the design matrix terms (A_2) of the plane parameters .

$$\begin{bmatrix} A_1^T(BP^{-1}B^T)^{-1}A_1 & A_1^T(BP^{-1}B^T)^{-1}A_2 \\ A_2^T(BP^{-1}B^T)^{-1}A_1 & A_2^T(BP^{-1}B^T)^{-1}A_2 + G^T P_c G \end{bmatrix} \begin{bmatrix} \hat{\delta}_1 \\ \hat{\delta}_2 \end{bmatrix} + \begin{bmatrix} A_1^T(BP^{-1}B^T)^{-1}w \\ A_2^T(BP^{-1}B^T)^{-1}w + G^T P_c w_c \end{bmatrix} = \begin{bmatrix} 0 \\ 0 \end{bmatrix} \quad (4.36)$$

or it can be written as

$$N\hat{\delta} + u = 0 \quad (4.37)$$

for abbreviation.

If we let $M = BP^{-1}B^T$, Equation 4.36 becomes:

$$\begin{bmatrix} A_1^T M^{-1} A_1 & A_1^T M^{-1} A_2 \\ A_2^T M^{-1} A_1 & A_2^T M^{-1} A_2 + G^T P_c G \end{bmatrix} \begin{bmatrix} \hat{\delta}_1 \\ \hat{\delta}_2 \end{bmatrix} + \begin{bmatrix} A_1^T M^{-1} w \\ A_2^T M^{-1} w + G^T P_c w_c \end{bmatrix} = \begin{bmatrix} 0 \\ 0 \end{bmatrix} \quad (4.38)$$

Similarly, for the catenary-based calibration, if design matrix for the catenary parameters

is defined as A_3 for solving $\hat{\delta}_3$, the normal matrix, N can be expressed as the following equation:

$$N = \begin{bmatrix} A_1^T M^{-1} A_1 & A_1^T M^{-1} A_3 \\ A_3^T M^{-1} A_1 & A_3^T M^{-1} A_3 \end{bmatrix} \quad (4.39)$$

When both the plane and catenary features are used in the calibration simultaneously, the normal matrix, N can be expressed as the following equation:

$$N = \begin{bmatrix} A_1^T M^{-1} A_1 & A_1^T M^{-1} A_2 & A_1^T M^{-1} A_3 \\ A_2^T M^{-1} A_1 & A_2^T M^{-1} A_2 + G^T P_c G & A_2^T M^{-1} A_3 \\ A_3^T M^{-1} A_1 & A_3^T M^{-1} A_2 & A_3^T M^{-1} A_3 \end{bmatrix} \quad (4.40)$$

4.2.2 Residual Computation

After the unknowns are estimated, the residuals for observations (\hat{v}) and constraints (\hat{v}_c) can be computed with the original observation by back-substitution as the following:

From Equation 4.22, we have

$$\hat{v} = -P^{-1} B^T \hat{k} \quad (4.41)$$

Substituting Equation 4.41 into Equation 4.26, we have:

$$\hat{k} = (BP^{-1}B^T)^{-1}(A_1\hat{\delta}_1 + A_2\hat{\delta}_2 + w) \quad (4.42)$$

Substituting Equation 4.42 back into Equation 4.41, finally we get:

$$\hat{v} = -P^{-1}B^T(BP^{-1}B^T)^{-1}(A_1\hat{\delta}_1 + A_2\hat{\delta}_2 + w) \quad (4.43)$$

From Equation 4.25, we have:

$$\hat{v}_c = P_c^{-1} \hat{k}_c \quad (4.44)$$

Substituting Equation 4.44 into Equation 4.27, we have:

$$\hat{k}_c = P_c(G\hat{\delta}_2 + w_c) \quad (4.45)$$

Substituting Equation 4.45 back into Equation 4.44, finally we get:

$$\hat{v}_c = G\hat{\delta}_2 + w_c \quad (4.46)$$

Similarly, the residuals of observation for catenary-based and mixed feature-based are computed by Equation 4.47 and 4.48 respectively:

$$\hat{v} = -P^{-1}B^T(BP^{-1}B^T)^{-1}(A_1\hat{\delta}_1 + A_3\hat{\delta}_3 + w) \quad (4.47)$$

$$\hat{v} = -P^{-1}B^T(BP^{-1}B^T)^{-1}(A_1\hat{\delta}_1 + A_2\hat{\delta}_2 + A_3\hat{\delta}_3 + w) \quad (4.48)$$

4.2.3 Stochastic Model

For the sake of simplification of the model formulation, and also due to the fact that the information of the cross-correlation of the GPS/IMU is not available, all the eight observational errors are essentially assumed to have zero-mean and be uncorrelated with each other, as in Skaloud and Lichti (2006) and Kumari et al. (2011). Thus, the weight matrix for the observations, P is a diagonal matrix and is given as the following:

$$P = C_l^{-1} = \begin{bmatrix} P_1 & 0 & \cdots & 0 \\ 0 & P_2 & \cdots & 0 \\ \vdots & \vdots & \ddots & \vdots \\ 0 & 0 & \cdots & P_n \end{bmatrix} \quad (4.49)$$

where,

$$P_i = \begin{bmatrix} \frac{1}{\sigma_{X_{Ii}}^2} & 0 & 0 & 0 & 0 & 0 & 0 & 0 \\ 0 & \frac{1}{\sigma_{Y_{Ii}}^2} & 0 & 0 & 0 & 0 & 0 & 0 \\ 0 & 0 & \frac{1}{\sigma_{Z_{Ii}}^2} & 0 & 0 & 0 & 0 & 0 \\ 0 & 0 & 0 & \frac{1}{\sigma_{r_i}^2} & 0 & 0 & 0 & 0 \\ 0 & 0 & 0 & 0 & \frac{1}{\sigma_{p_i}^2} & 0 & 0 & 0 \\ 0 & 0 & 0 & 0 & 0 & \frac{1}{\sigma_{y_i}^2} & 0 & 0 \\ 0 & 0 & 0 & 0 & 0 & 0 & \frac{1}{\sigma_{\rho_i}^2} & 0 \\ 0 & 0 & 0 & 0 & 0 & 0 & 0 & \frac{1}{\sigma_{\theta_i}^2} \end{bmatrix} \quad (4.50)$$

It is also assumed that the constraints for all planes, as well as the parameters of each plane are equally weighted. Thus, the weight matrix, P_c of the constraint is given as:

$$P_c = \frac{1}{\sigma_c^2} I \quad (4.51)$$

where, σ_c^2 is the variance of the constraint, and its value should be set much smaller than that of any of the eight observations such that

$$\frac{1}{\sigma_c^2} \gg P_{i_{1,2,\dots,8}} \quad (4.52)$$

4.2.4 Design Matrices of Unknowns and Observations

In the calibration, there are three group of unknowns of our interest: (1) the boresight parameters, $((\alpha, \beta, \gamma)_{s_n=1,2,3,4})$; (2) the plane parameters, $(a_p, b_p, c_p, d_p)_{j=1\dots q_p}$; (3) the catenary parameters, $(a_c, b_c, c_c)_{j=1\dots q_c}$, where q_p and q_c denote the numbers of the planes and catenaries respectively for the calibration. Note that for catenary-based calibration, only the boresights of Scanner 1 and 2 are solved, therefore, $s_n = 1, 2$.

The design matrix A is split into two or three matrices as the following:

$$A = \begin{cases} \begin{bmatrix} A_1 & A_2 \end{bmatrix} & \text{for the plane-based calibration} \\ \begin{bmatrix} A_1 & A_3 \end{bmatrix} & \text{for the catenary-based calibration} \\ \begin{bmatrix} A_1 & A_2 & A_3 \end{bmatrix} & \text{for the mixed features-based calibration} \end{cases} \quad (4.53)$$

The number of rows of A is equal to the number of the observed points, n .

For an observed point i , the i^{th} row of A_1 , a_{1i} is expressed as the following row vectors depending on which scanner captured the point i :

$$a_{1i} = \begin{cases} \left[\frac{\partial f_p}{\partial \alpha_1} & \frac{\partial f_p}{\partial \beta_1} & \frac{\partial f_p}{\partial \gamma_1} & 0 & 0 & 0 & 0 & 0 & 0 & 0 & 0 & 0 \right]_i & \text{if point } i \text{ is captured by Scanner 1;} \\ \left[0 & 0 & 0 & \frac{\partial f_p}{\partial \alpha_2} & \frac{\partial f_p}{\partial \beta_2} & \frac{\partial f_p}{\partial \gamma_2} & 0 & 0 & 0 & 0 & 0 & 0 \right]_i & \text{if point } i \text{ is captured by Scanner 2;} \\ \left[0 & 0 & 0 & 0 & 0 & 0 & \frac{\partial f_p}{\partial \alpha_3} & \frac{\partial f_p}{\partial \beta_3} & \frac{\partial f_p}{\partial \gamma_3} & 0 & 0 & 0 \right]_i & \text{if point } i \text{ is captured by Scanner 3;} \\ \left[0 & 0 & 0 & 0 & 0 & 0 & 0 & 0 & 0 & \frac{\partial f_p}{\partial \alpha_4} & \frac{\partial f_p}{\partial \beta_4} & \frac{\partial f_p}{\partial \gamma_4} \right]_i & \text{if point } i \text{ is captured by Scanner 4;} \end{cases} \quad (4.54)$$

or for the catenary-based calibration,

$$a_{1i} = \begin{cases} \left[\frac{\partial f_c}{\partial \alpha_1} & \frac{\partial f_c}{\partial \beta_1} & \frac{\partial f_c}{\partial \gamma_1} & 0 & 0 & 0 \right]_i & \text{if point } i \text{ is captured by Scanner 1;} \\ \left[0 & 0 & 0 & \frac{\partial f_c}{\partial \alpha_2} & \frac{\partial f_c}{\partial \beta_2} & \frac{\partial f_c}{\partial \gamma_2} \right]_i & \text{if point } i \text{ is captured by Scanner 2;} \end{cases} \quad (4.55)$$

The number of columns of A_1 depends the number of scanners involved in the calibration.

For an observed point i , the i^{th} row of A_2 , a_{2i} is expressed as the following row vectors with the length equal to the number of the planes, $q_p \times 4$:

$$a_{2i} = \left[0 \ 0 \ 0 \ 0 \ \dots \ \frac{\partial f_p}{\partial \alpha_{pk}} \ \frac{\partial f_p}{\partial \beta_{pk}} \ \frac{\partial f_p}{\partial \gamma_{pk}} \ \frac{\partial f_p}{\partial d_{pk}} \ \dots \ 0 \ 0 \ 0 \ 0 \right]_i \quad (4.56)$$

for a point lying on the k^{th} plane.

Similarly, for an observed point i , the i^{th} row of A_3 , a_{3i} is expressed as the following row vectors with the length equal to the number of the catenaries, $q_c \times 3$:

$$a_{3i} = \left[0 \ 0 \ 0 \ \dots \ \frac{\partial f_c}{\partial a_{ck}} \ \frac{\partial f_c}{\partial b_{ck}} \ \frac{\partial f_c}{\partial c_{ck}} \ \dots \ 0 \ 0 \ 0 \right]_i \quad (4.57)$$

for a point lying on the k^{th} catenary. Note that the centroid of the catenary in the $x - y$ plane, x_m and y_m are not solved in the adjustment but their values are updated as the observation are for each iteration.

Let

$$b_i = \left[\frac{\partial f}{\partial X_I} \ \frac{\partial f}{\partial Y_I} \ \frac{\partial f}{\partial Z_I} \ \frac{\partial f}{\partial r} \ \frac{\partial f}{\partial p} \ \frac{\partial f}{\partial y} \ \frac{\partial f}{\partial \rho} \ \frac{\partial f}{\partial \theta} \right]_i \quad (4.58)$$

where,

$$f = \begin{cases} f_p(\vec{x}, \vec{l}) & \text{if } i^{th} \text{ point belongs to a plane} \\ f_c(\vec{x}, \vec{l}) & \text{if } i^{th} \text{ point belongs to a catenary} \end{cases} \quad (4.59)$$

The the i^{th} of design matrix of the observations (B), b'_i is given as the following:

$$b'_i = \left[0 \ 0 \ 0 \ 0 \ 0 \ 0 \ 0 \ 0 \ \dots \ b_i \ \dots \ 0 \ 0 \ 0 \ 0 \ 0 \ 0 \ 0 \ 0 \right]_i \quad (4.60)$$

Let

$$g_i = \left[\frac{\partial g_p}{\partial a_{pk}} \ \frac{\partial g_p}{\partial b_{pk}} \ \frac{\partial g_p}{\partial c_{pk}} \ \frac{\partial g_p}{\partial d_{pk}} \right]_i \quad (4.61)$$

Whenever the point i belongs to a plane, its contribution to the design matrix of the constraint (G), i.e. the i^{th} row of G , g'_i is computed as the following:

$$g'_i = \left[0 \ 0 \ 0 \ 0 \ \dots \ g_i \ \dots \ 0 \ 0 \ 0 \ 0 \right]_i \quad (4.62)$$

4.2.5 Efficient Computation of the Normal Matrix and the Residuals

4.2.5.1 Efficient Computation of the Normal Matrix - Summation of Normals

It is straightforward to use the summation of normals algorithm (Mikhail and Ackerman, 1976) for implementing the least-squares when the number of observations are getting considerably large. The algorithm utilizes the fact that the weight matrix is block-diagonal, so that the whole normal matrix is block-diagonal, then the unnecessary multiplication of zero terms can be eliminated and also design matrices with large dimensions can be avoided. Instead to form the full design matrices at one time, the design matrices are broken down into row vectors and the products of vector multiplications are then summed up to form the normal matrix.

For the plane-based calibration, for the total number of the observed point n , the normal equation matrix, N is calculated as the following with the constraint term added to corresponding location of N :

$$N = \sum_{i=1}^n \begin{bmatrix} a_{1i}^T \\ a_{2i}^T \end{bmatrix} \begin{bmatrix} m_{ii}^{-1} \end{bmatrix} \begin{bmatrix} a_{1i} & a_{2i} \end{bmatrix} + \sum_{j=1}^{q_p} \frac{1}{\sigma_c^2} g_j^T g_j \quad (4.63)$$

Similarly, for the catenary-based calibration, the contribution of each observation can be added to N sequentially as the following:

$$N = \sum_{i=1}^n \begin{bmatrix} a_{1i}^T \\ a_{3i}^T \end{bmatrix} \begin{bmatrix} m_{ii}^{-1} \end{bmatrix} \begin{bmatrix} a_{1i} & a_{3i} \end{bmatrix} \quad (4.64)$$

For the mixed features calibration using both the plane and catenary, the normal matrix N_m is calculated as the following:

$$N = \sum_{i=1}^{n_p} \begin{bmatrix} a_{1i}^T \\ a_{2i}^T \end{bmatrix} \begin{bmatrix} m_{ii}^{-1} \end{bmatrix} \begin{bmatrix} a_{1i} & a_{2i} \end{bmatrix} + \sum_{i=n_p+1}^n \begin{bmatrix} a_{1i}^T \\ a_{3i}^T \end{bmatrix} \begin{bmatrix} m_{ii}^{-1} \end{bmatrix} \begin{bmatrix} a_{1i} & a_{3i} \end{bmatrix} + \sum_{j=1}^{q_p} \frac{1}{\sigma_c^2} g_j^T g_j \quad (4.65)$$

where, $m_{ii} = b_i P_i^{-1} b_i^T$ and n_p is total number of points of the planes.

4.2.5.2 Efficient Computation of the Residuals

The residual vectors, \hat{v} and \hat{v}_c can be expressed as:

$$\hat{v} = \begin{bmatrix} \hat{v}_1 & \hat{v}_2 & \dots & \hat{v}_m \end{bmatrix}^T \quad (4.66)$$

and

$$\hat{v}_c = \begin{bmatrix} \hat{v}_{c_1} & \hat{v}_{c_2} & \dots & \hat{v}_{c_{qp}} \end{bmatrix}^T \quad (4.67)$$

and thus can be computed point by point. For point i ,

$$\hat{v}_i = -P_i^{-1} b_i (b_i P_i^{-1} b_i^T)^{-1} (a_{1i} \hat{\delta}_1 + a_{2i} \hat{\delta}_2 + w_i) \quad (4.68)$$

and for points lying on the k^{th} plane,

$$\hat{v}_{c_k} = g_k \hat{\delta}_{2k} + w_{c_k} \quad (4.69)$$

The functional models and the least-squares implementation algorithm are already presented and ready for calibration. However, the data must be converted to an appropriate coordinate system (the mapping frame, ENU in this work) and the features should be segmented properly without blunders. The blunder detection is needed for both the planes and the catenaries before using them for calibration. The degree of symmetry of the catenaries must also be considered to avoid extremely high correction existing between the parameters for the adjustment. The details of these precautions and also the calibration results are given in the next Chapter.

Chapter 5

Calibration Input and Results Analysis

5.1 Calibration Input Data Set

5.1.1 Calibration Data Set Description

The data set was captured with TITAN around the riverside of the St Lawrence River in Montreal, Quebec, Canada at the end of 2008. The data comprised 17 drive lines. The data mainly comprise the point cloud of an intersection of the bridge (Route Transcandinienne) and the Highway Route 132 of Quebec as shown in the Google MapsTM illustrated in Figure 5.1 and the figure also shows the $x - y$ plane of the captured point cloud. The point cloud also comprises an ramp with a hotel that provides façades.

The data set was not intentionally captured for the purpose of calibration. It was originally captured for highway surveying purposes. Nevertheless, the methodology developed in this thesis can be applied to any data and it is not necessary to collect specific data for only calibration.

Two zones were selected from this for the calibration input set as they contain most of the geometric features as illustrated in Figure 5.4: (1) The intersection between the highway and the bridges (Figure 5.2); (2) The hotel adjacent to the ramp (Figure 5.3). The four different colors (pale green, red, cyan and blue) indicate the point clouds captured by scanners 1, 2, 3 and 4 respectively. Scanner 1 and 2 captured the most points while the Scanner 4 captured the least (Figure 5.5).

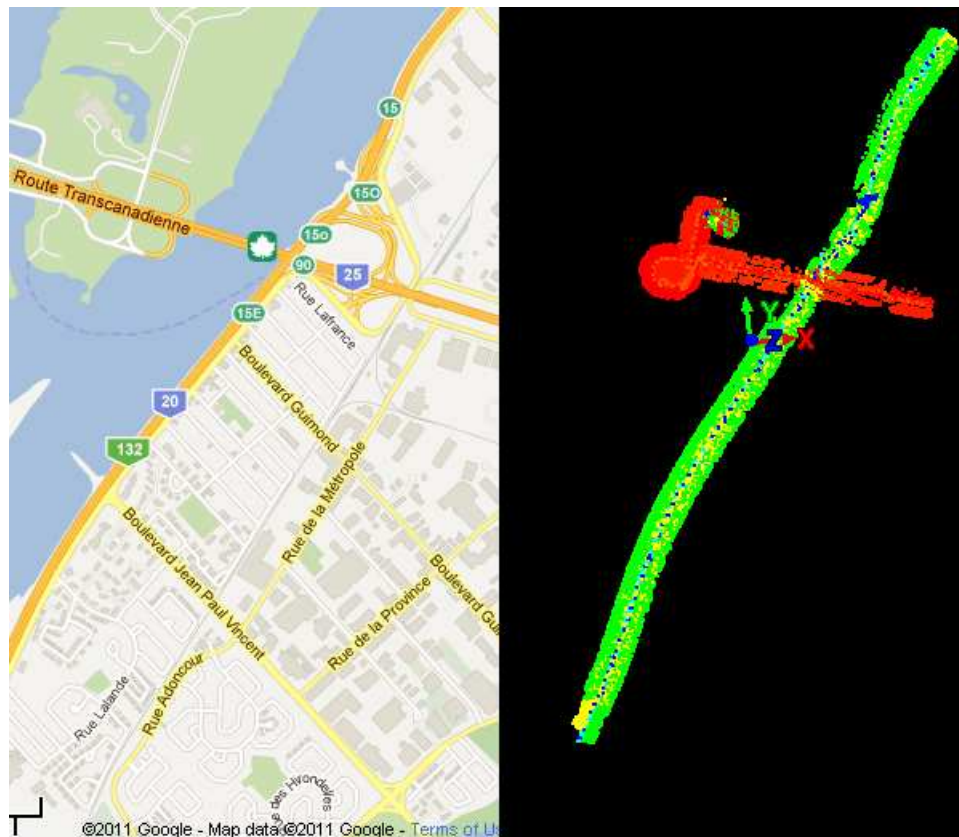


Figure 5.1: The Google MapTM and point cloud of the captured highway scene in Montreal

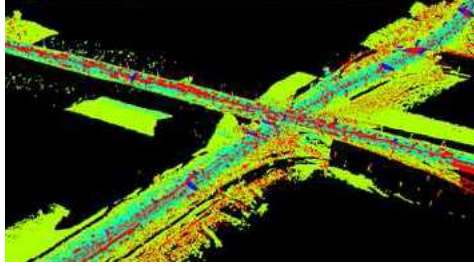


Figure 5.2: Calibration zone 1: The intersection of the highway and the bridge

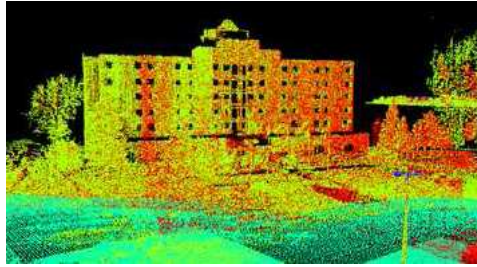


Figure 5.3: Calibration zone 2: The hotel adjacent to the ramp

5.1.2 Initial Approximate Values Estimation for Calibration

5.1.2.1 Initial Approximated Values Estimation of the Boresights

The initial approximate values of the boresights are the nominal values of the corresponding boresights. The initial approximate values of boresights can also be obtained by the least-squares approach or manual edge alignment approach that has been described in Chapter 2 - Boresight Errors.

5.1.2.2 Initial Approximate Values Estimation of Features Parameters

5.1.2.2.1 Approximate Values Estimation of the Plane Parameters

The approximate values of the plane parameters (a_p , b_p , c_p and d_p) can be calculated directly from the point clouds with the method of orthogonal regression. The method minimizes the sum of the squares of the orthogonal distances to a plane by reducing the least-squares problem to an eigenvalue problem. The detailed proof can be found on Shakarji (1998) and the essential procedure of the method is summarized as follows:

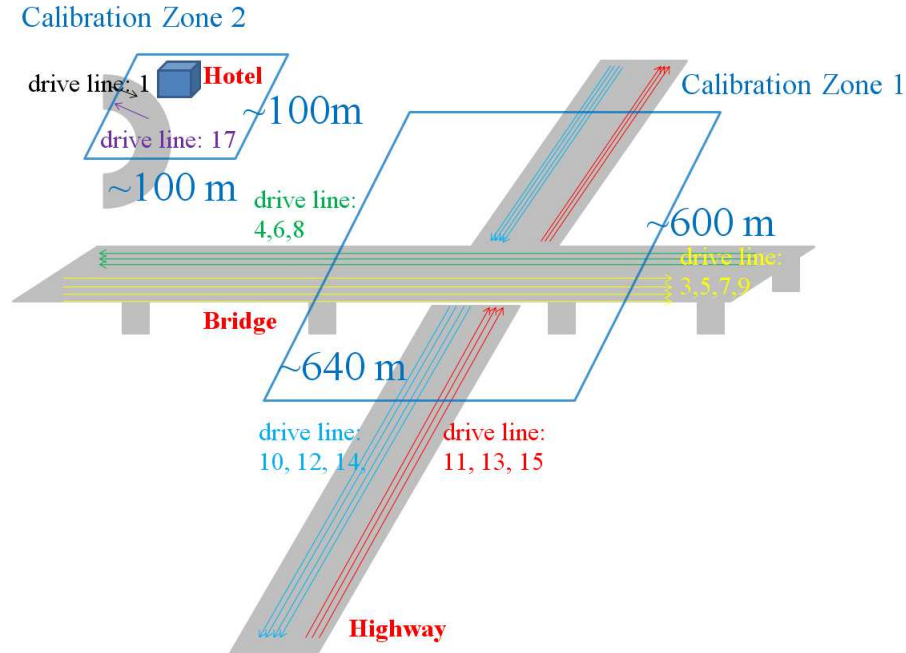


Figure 5.4: The Drive Lines

1. Calculate the centroid of the points lying on the plane
2. Calculate the covariance matrix C with all the x , y and z observation of the plane
3. Find the smallest eigenvalue of C and its corresponding normalized eigenvector.
The normalized eigenvector comprises the direction cosines a_p , b_p and c_p
4. Calculate the orthogonal distance d_p by the dot product of the centroid row vector and the normalized eigenvector

5.1.2.2.2 Initial Approximate Values Estimation of the Catenary Parameters

The initial values of the catenary parameter can be found by first fitting the point cloud with a 2D line and then followed by a 2D catenary fit with the catenary parameters a_c , b_c and c_c .

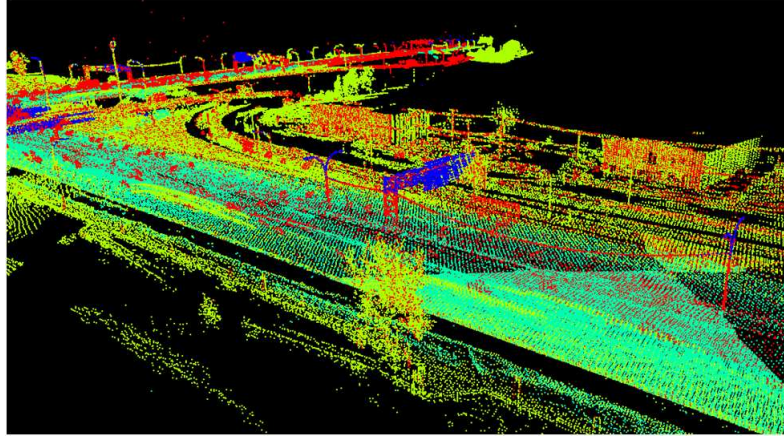


Figure 5.5: The point clouds captured by Scanner 1, 2, 3 and 4 are depicted by pale green, red, cyan and blue color respectively

5.1.3 Feature Extraction

Since the feature segmentation is out of the scope of this research, all the features were extracted manually using the point cloud processing software Leica Cyclone 7.0.2. Cyclone can only load point clouds with four columns (X , Y , Z and intensity). Therefore, once the features coordinates are extracted, the raw MMS measurements had to be traced back from the database created with the whole data set by looking up the exact X , Y , and Z coordinates.

5.1.4 Blunder Detections of Calibration Input

To assure the calibration quality, any blunders of the calibration input have to be detected and removed before the calibration, by computing the standardized residuals when fitting the features' point cloud with their geometric models. Let A , B be the design matrices for the unknowns and observation of the feature fitting respectively; P is the weight matrix of the feature fitting. Then, the standardized residual, \hat{r}_i is computed as the following:

$$\hat{r}_i = \frac{\hat{v}_i}{\sqrt{\sigma_i^2 R_{ii}}} \quad (5.1)$$

where, \hat{v}_i is the residual, σ_i^2 is the i^{th} diagonal element of the P^{-1} and R_{ii} is the i^{th} diagonal element of the reliability matrix, R computed by the following equation (Cothren, 2005):

$$R = P^{-1}B^T M^{-1}(I - AN^{-1}A^T M^{-1})B \quad (5.2)$$

where $N = A^T M^{-1}A$ and $M = BP^{-1}B^T$.

5.2 Results of Plane-based Calibration

5.2.1 Calibration with 56 Planes

Fifty-six planes extracted from the intersection area (Calibration Zone 1 of Figure 5.4) were used for performing the 4-scanner self-calibration and the results are shown in Table 5.1. The 56 planes were captured with the system travelled in parallel drive lines on the highway. The results are compared with the calibrated values given by Terrapoint, based on its own dedicated plane-based calibration techniques using 350 planes. The values were estimated from another independent dataset that was collected specifically for calibration every two years. It can be seen that there are larger discrepancies between the estimated values of the two calibrations for the Scanner 3 and 4. The residuals of the eight observations are shown in Figure 5.6. All the residual distributions are centred around zero. That implies that the model is appropriate and the overall adjustment estimation is in good condition. Before analysing the parameter precisions and the geometry of the scanners and planes, an important concept is first explained as follows. As the 2D-line scanner is moving with the whole system, all laser beams hitting a plane must be parallel to each other. Figure 5.7 (Top) shows the $x - y$ cross-section of a vertical plane with an arbitrary orientation and Scanner 1 installed with γ_a ; and 5.7 (Bottom) shows the same vertical plane but with Scanner 1 installed with γ_b . It can be seen that if only one plane's orientation is given, the corresponding γ can be either γ_a or γ_b , or some other values. That means only one plane is not sufficient to solve γ . If we presume

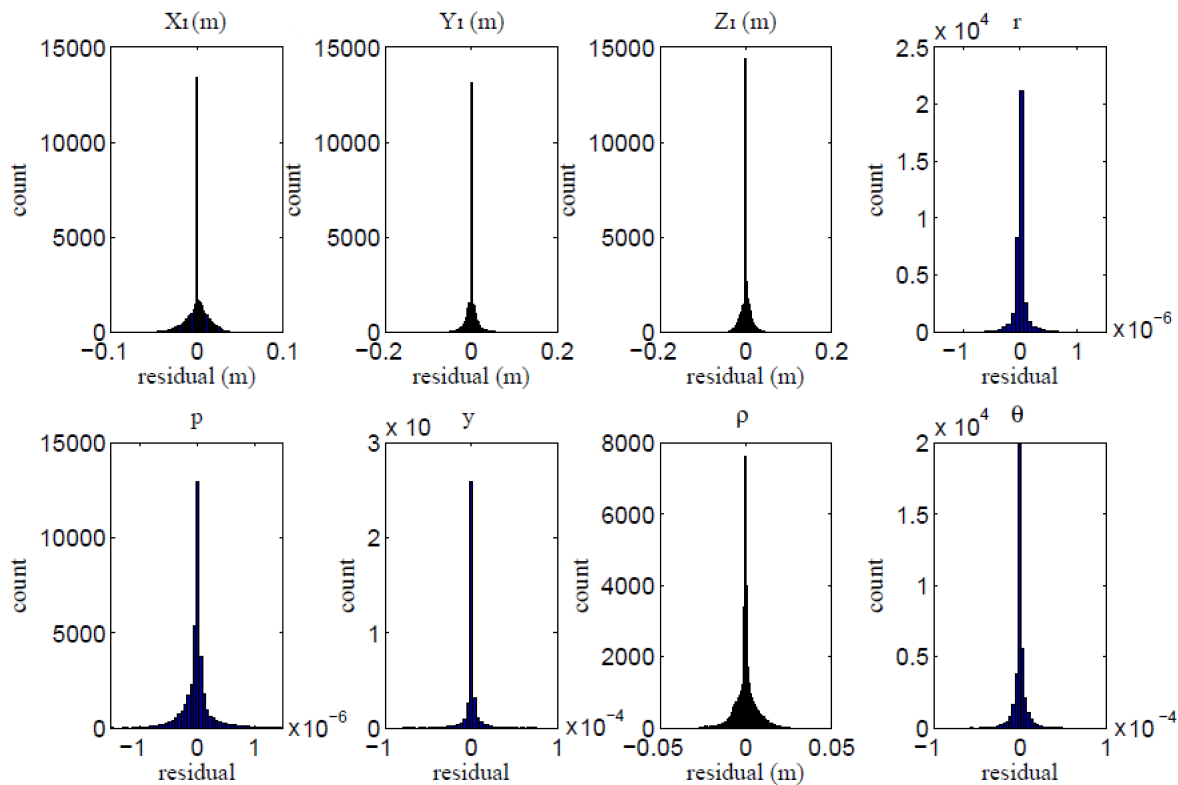


Figure 5.6: The residuals of plane-based calibration adjustment using 56 planes

there are two planes with different orientations, then an optimal value of γ exists and can be estimated. As the number of the vertical planes with different orientations increases, the more precisely γ can be determined. It is noted that planes orientated differently in the $x - y$ can solve γ effectively (Figure 5.8). As a result, similarly, vertical planes orientated differently in the $x - z$ can solve α effectively (Figure 5.9). However, vertical planes orientated differently in the $y - z$ cannot solve β because the vertical planes being rotated in the $y - z$ (about the x -axis) are basically equivalent in terms of the direction cosines. So using only vertical planes cannot solve β . This could explain that β is the most poorly estimated because the input planes for Scanner 1 and 2 are mainly vertical planes.

Another way to explain the lowest precision of β can be done by analysing Figure 5.10.

Table 5.1: Calibration results with 56 input planes

				53742
DOF				
Scanner	Boresight ($^{\circ}$) angle	Terrapoint($^{\circ}$) value	Estimated ($^{\circ}$) value	$\sigma(^{\circ})$
1	α	90.2388	90.1405	0.0104
	β	0.0207	0.0623	0.0167
	γ	8.7677	8.8078	0.0019
2	α	270.3228	270.4021	0.0129
	β	0.0004	-0.5761	0.0196
	γ	-8.7277	-8.6701	0.0030
3	α	0.8464	0.9766	0.0551
	β	-69.8769	-69.7423	0.0143
	γ	-0.9728	-1.5316	0.3776
4	α	0.2947	-1.5255	0.1979
	β	129.9668	130.1442	0.0104
	γ	180.0676	178.7314	0.1435
$\hat{\sigma}_o$				0.92079

It shows the geometry of Scanner 1 and a captured vertical plane with an arbitrary orientation. β is defined as the rotational angle about the x -axis of the scanner-frame. If Scanner 1's x -axis is orthogonal to the driving direction, any absolute vertical planes will have unit normal vector in the form of $\begin{pmatrix} a & b & 0 \end{pmatrix}$ where a and b are the direction cosines for the x and y axis. Then, any deviation of β ($\delta\beta$) will result in deviation of the $y - z$ plane, i.e. the $y - z$ coordinates of the measurements. Since all the scanners in TITAN are 2D-line scanners, there is no y coordinate measurement. Therefore, the y measurement can be omitted. This means that $\delta\beta$ is directly associated with the deviation in the z measurement. The $\delta\beta$ in Figure 5.10 leads to a shift of Point Cloud 1 to Point Cloud 2 of the captured vertical plane. Only the z coordinates of the points are shifted. The x and y coordinates, as well as the direction cosines of Point Cloud 1 and Point Cloud 2 are equivalent. Thus, the $\delta\beta$ has no impact on the direction cosine of the plane and vice versa. This concept can be further confirmed with fitting of a simulated

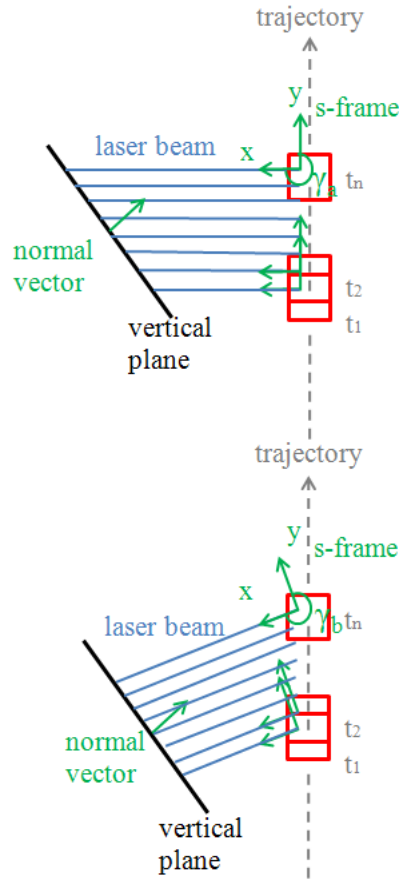


Figure 5.7: Scanner 1 and a vertical plane with γ_a (Top) and γ_b (Bottom)

vertical plane with random noise in both x , y and z , it is found that the z -residuals are always insignificant as the orientation of the vertical planes only depend on x and y coordinates. To recapitulate, adjusting the direction cosines of vertical planes fails to adjust β of Scanner 1, and also β of Scanner 2 as they have the similar geometry. In reality, the x -axis of Scanner 1 is not absolutely orthogonal to the driving direction and also vertical planes may not be absolutely orthogonal to the ground (the direction cosine, c_p will not equal zero, but a tiny number), thus the z -measurement of the vertical planes can still contribute to the estimation of β , but insignificantly. Accordingly, the precision of β is relatively the lowest. Most of the planes used for the calibration are vertical as they are mainly building façades. They orientate differently in the $x - y$ plane and thus

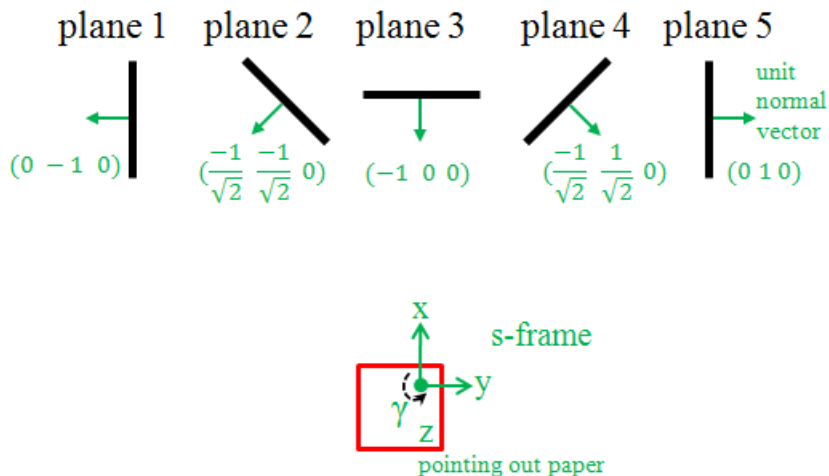


Figure 5.8: The geometry of Scanner 1 and five vertical planes with different normal vectors

the precision of γ is relatively the highest.

The β angle of both Scanner 3 and Scanner 4 have the highest precisions among the three boresights, which is the opposite to that of Scanners 1 and 2. Again, this can be accounted for by analyzing the geometry of the scanners and also the orientation of the input planes. Table 5.2 shows that Scanner 3 has only the input planes with only one orientation (i.e. the ground surfaces with their normal vector pointing upward as illustrated in Figure 5.11), while Scanner 4 has captured planes with two kinds of orientation (the bottoms of bridges with their normal vectors pointing upward and also large surfaces of traffic signs with normal vectors parallel to the $x - y$ plane). Based on the explanation

Scanner	Type of the 56 planes
1	Mainly vertical façades
2	Mainly vertical façades
3	Ground surfaces
4	Large Traffic Signs and Bridge bottoms

for β of Scanner 1, $\delta\beta$ of Scanner 3 is also associated with z -measurements. On the

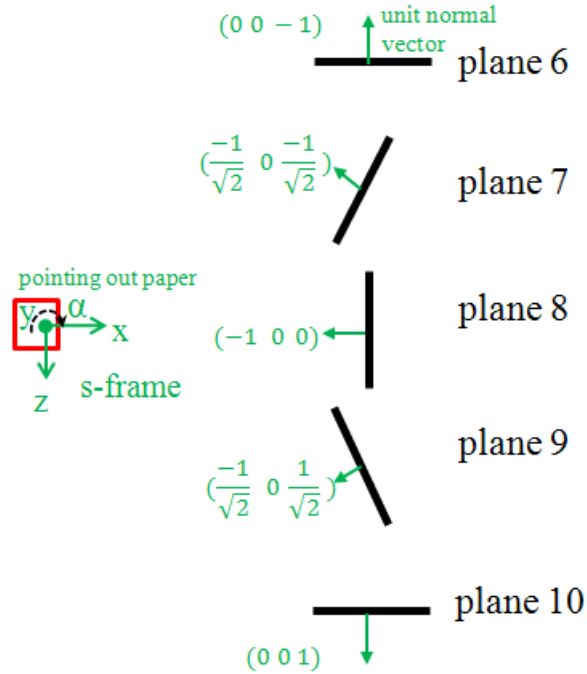


Figure 5.9: The geometry of Scanner 1 and five tilted/horizontal planes with different normal vectors

contrary to vertical planes, z -measurements are significant for defining horizontal planes while the x and y -measurements are not. Apart from this, the simultaneous estimation of the four set of boresights leads to more rigorous estimation of the direction cosines of horizontal planes as the two side edges of horizontal planes can be captured by Scanner 1 and 2 (overlapping point clouds of between Scanner 1 and 3, and also between Scanner 2 and 3). Therefore, β can be precisely estimated. Analogically, $\delta\alpha$ is associated with both the x and z measurements and so the estimation of α can also be benefited from the more rigorous estimation of direction cosine of the overlap. This applied to Scanner 4 as it has overlap regions with Scanner 1 and 2.

5.2.1.1 Accuracy Analysis

5.2.1.1.1 RMS of Test Plane Fitting

The RMSs in all the 3 dimensions of the fittings of 28 test planes extracted outside the

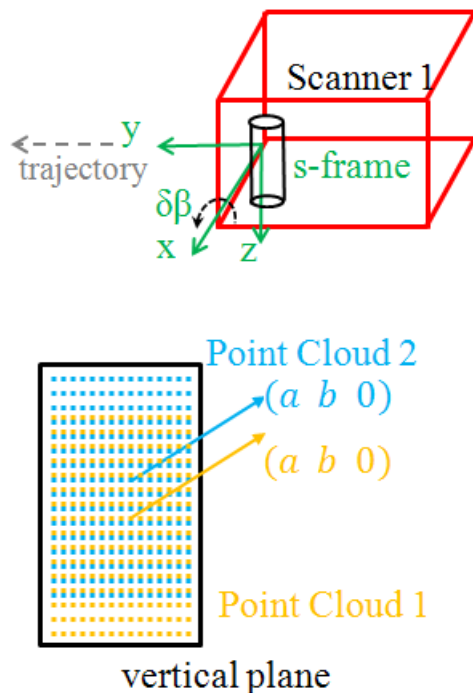


Figure 5.10: The Scanner 1 and a vertical plane in an arbitrary orientation

calibration zones are plotted versus the plane numbers of the test planes in Figure 5.12. It can be seen that the RMSs are reduced significantly after the calibration and also the performance of the calibration are compatible to that of the Terrapoint calibration.

5.2.1.1.2 Profile Analysis

The boresight values before and after the calibration, and also the values from the Terrapoint's calibration were used to reconstruct a long horizontal profile with the length approximately equals 340 m (Figure 5.13). It can be seen that the point cloud reconstructed before calibration contains two apparent layers that after the calibration and Terrapoint cases do not possess. Figure 5.14 and 5.15 compare the z -measurement of the profiles explicitly. Figure 5.14 compares the z -measurement of the profile while Figure 5.15 compares the absolute value of the difference of the profile z -measurement between the Terrapoint, and before and after calibration with the corresponding RMS in the z direction. The effectiveness of such the long profile reconstruction mainly relies on the

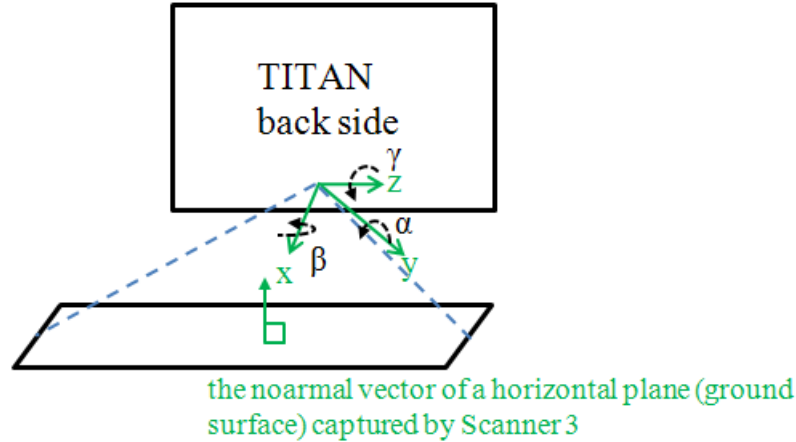


Figure 5.11: The geometry of Scanner 3 and a horizontal plane

accuracy of boresights of Scanner 3, and the discrepancy ($\text{RMS}_z = 0.019$ m) between the profile reconstructed by the calibrated boresights and Terrapoint boresights might be due the fact that the reduced number of planes are used in the calibration (only 56 planes compared to the 350 planes used by Terrapoint). Figure 5.16 shows another horizontal profile of a concrete bridge side from the data set with the length about 160 m reconstructed with the boresight values before and after the calibration, and also from the values from Terrapoint's calibration. More explicit comparisons of the $x - y$ positions of the bridge side are illustrated in Figure 5.17. Both the calibration and Terrapoint's boresight define a proper bridge side profile. The distance between the origin and a point of the profile in the $x - y$ plane, u , is defined as $u = \sqrt{x^2 + y^2}$ for evaluating the positioning accuracy of the profile in the $x - y$ plane. The differences in u between the point cloud reconstructed by Terrapoint boresights and the boresights before the calibration, as well as that between the Terrapoint boresights and the boresights after the calibration are compared in Figure, 5.18 along with the corresponding RMS. It can be seen that the RMS_u is greatly reduced from 1.796 m to 0.02 m.

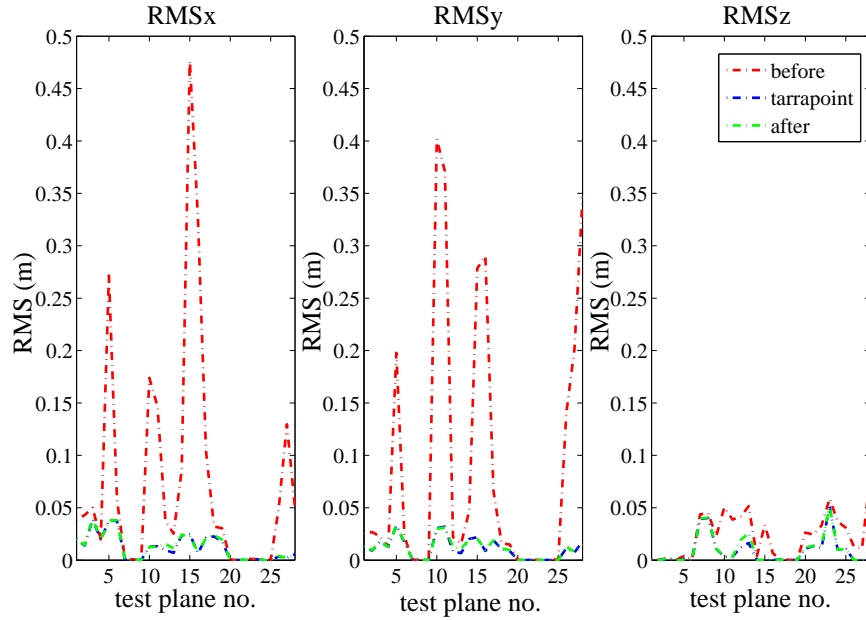


Figure 5.12: RMS of the test plane fitting with the point cloud of before, Terrapoint and after calibration

5.2.1.2 Parameter Correlation

Parameters correlation is an important indicator for assessing the reliability of an adjustment. Figure 5.19 shows the correlation matrix with the absolute values taken. There are no high correlation terms between the boresights and the plane parameters (the highest correlation coefficient is 0.667), but do exist between the plane parameters themselves. The high correlation is expected as the direction cosines (a_p , b_p and c_p) are constrained with the condition that the sum of squares of the direction cosines is equal to one.

5.2.2 Calibration Each Scanner Independently with the 56 Planes

In order to investigate the rigour of solving the four scanners in one adjustment process, the 56 planes were then divided into four groups to calibrate each scanner independently and the results are presented in Table 5.3. The estimated boresight values deviate significantly from the multi-scanner simultaneous adjustment solved values. As already explained, the geometry in the above section, the α is a function of x and z , and vertical

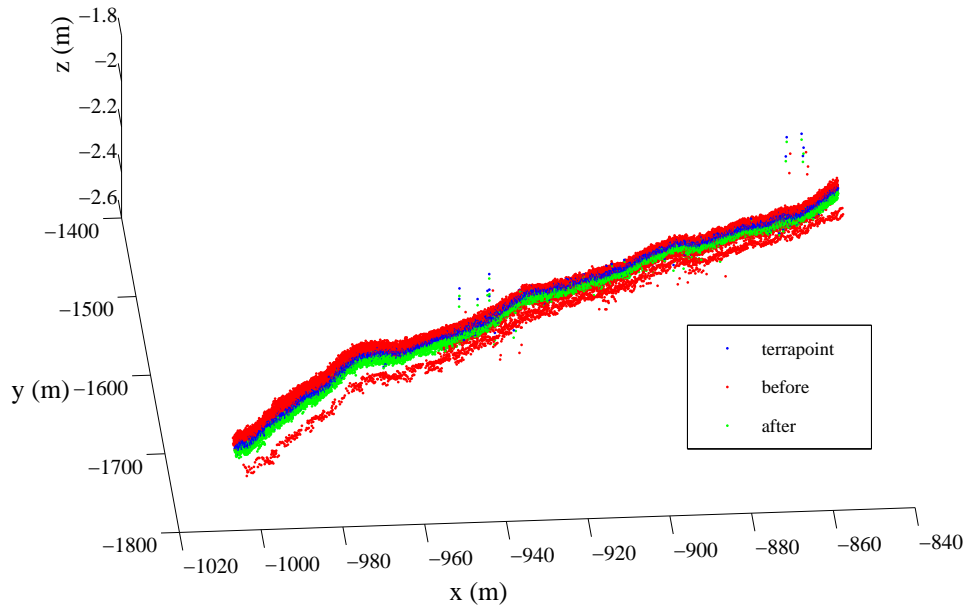


Figure 5.13: Horizontal profile of highway surface reconstructed

planes's z measurements do not contribute much on estimating α . The larger derivation of the estimated Scanner 1's α may be attributed to the relatively poorer variation in the x direction (direction cosine a_p) of Scanner 1's plane group than Scanner 2's plane group. Also, as the overlap regions are not considered, the number of iterations of Scanner 1 and 3 is relatively larger (the 56 planes simultaneous calibration has 16 iterations). The reason for the smallest number of iterations of Scanner 4 is due to the fact that Scanner 4 captured two type of orthogonal targets (vertical target signs and bridge bottoms), while the other Scanners do not possess orthogonal targets. Furthermore, the overall precision of all the boresight estimation are lower as the overlapping of the point clouds are not considered in the adjustment.

5.2.2.1 Accuracy Analysis

The average RMSs (Figure 5.2.2.1) of fittings of the 28 test planes after the simultaneous calibration are higher than that of the calibration solving the 4 sets of boresight with 56 planes. This demonstrates that considering the overlapped point clouds captured by

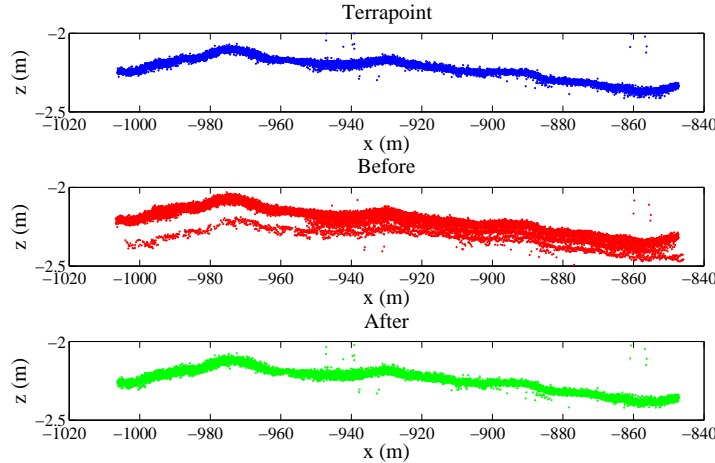


Figure 5.14: The z -measurement of the horizontal profile reconstructed

Table 5.3: Calibration results for solving the four sets of boresight independently

	Scanner 1		Scanner 2		Scanner 3		Scanner 4	
No. of planes	16		21		20		12	
No. of iter.	25		12		20		7	
DOF	10945		9255		7847		10809	
Boresight	Est. values($^{\circ}$)	Est. $\sigma(^{\circ})$						
α	87.334	0.092	270.890	0.160	1.017	0.044	0.078	0.180
β	-2.489	0.147	-0.704	0.073	-69.786	0.232	130.295	0.013
γ	9.049	0.018	-8.897	0.019	-1.784	0.308	179.819	0.128

different scanners to calibrate all the four scanners in one adjustment process is much more rigorous than calibrating each scanner independently. From the plot of the RMS z in Figure 5.2.2.1, it can be seen that the individual estimated values of Scanner 3 actually fail to reconstruct horizontal surfaces with reasonable heights, and the performance even worse than that of the nominal values before the calibration. Without accounting the overlap point clouds from Scanner 1 and 2 in the adjustment, only homogeneous horizontal ground surfaces indeed fail to estimate realistic values for the boresight of

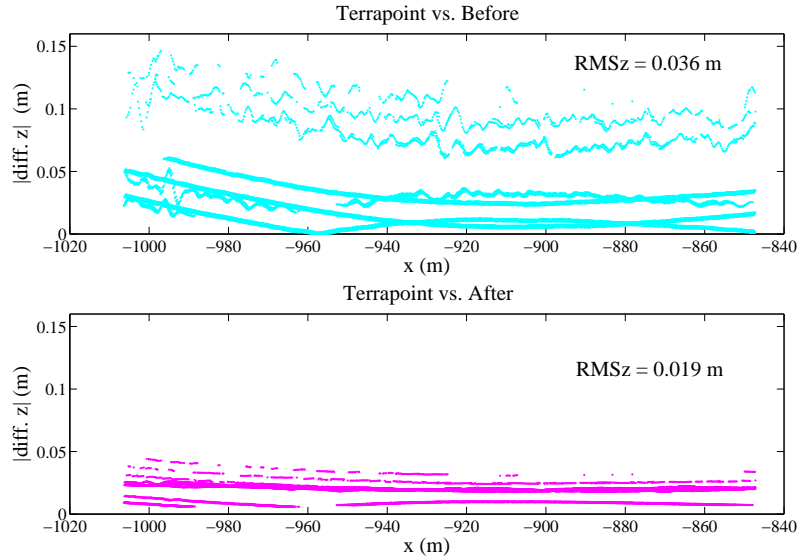


Figure 5.15: The difference in z of the horizontal profile

the Scanner 3. This is confirmed by Filin (2003) and Skaloud and Lichti (2006) that several planes with different orientations are needed for calibrating the boresight of a single scanner ALS. Scanner 4 has a similar scanning geometry with Scanner 3, however, the performance individual estimated values of Scanner 4 are compatible with that of the simultaneous calibration since the its input planes have more than one, and also orthogonal geometry (vertical traffic signs and horizontal bridge bottoms).

5.2.3 Examination of the Plane-based Calibration Using Groups of Planes in Parallel and Orthogonal Drive Lines

Since the drive lines on the bridge (Figure 5.4) do not possess plane surfaces captured with Scanner 1 and 2, the façades of the hotel outside the intersection are used to examine the impact of using the planar features captured with the system travels in orthogonal drive lines on the calibration. Nine plane surfaces are divided into three groups and used to perform nine independent calibration to Scanner 1. The details of the nine planes are summarized in Table 5.4. The calibration results of the nine calibrations are shown in

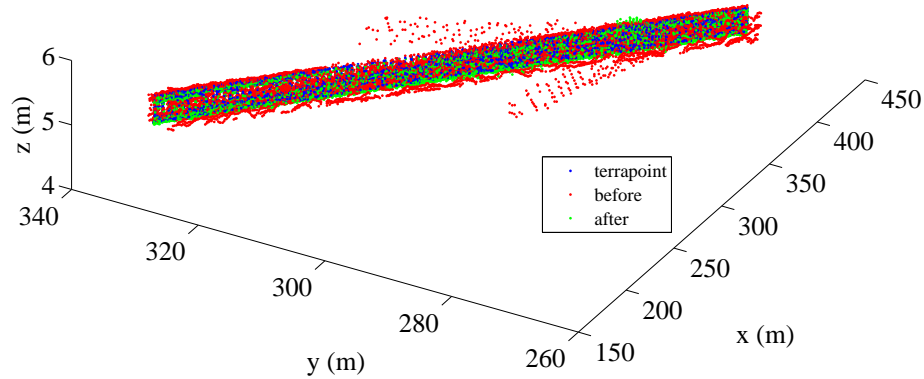


Figure 5.16: Horizontal profile of bridge side reconstructed

Table 5.4: The groups of planes used to examine the impact of using planar features captured by the system travelling in orthogonal drive lines

	Plane(p)	drive line location
Group 1	1,2,3	the highway
Group 2	4,5,6	the highway
Group 3	7,8,9	the ramp adjacent to the hotel

Table 5.5. It can be seen that by adding Group 2 (p4, p5 and p6) to calibration using Group 1 (p1, p2 and p3) does enhance the estimation since all the planes are captured with parallel drive lines. However, adding Group 3 (p7, p8 and p9) is more beneficial to the calibration, especially to the estimation of β , as it can be seen that the estimated values are more compatible with the results of the 56 planes calibration and also the overall precision is improved. Therefore, orthogonal drive line data are important to calibrate the Scanner 1 as well as Scanner 2. This motivates the next experiment of reducing the number of parallel drive line planes but adding orthogonal drive line planes from the hotel (from 56 planes to 24 planes).

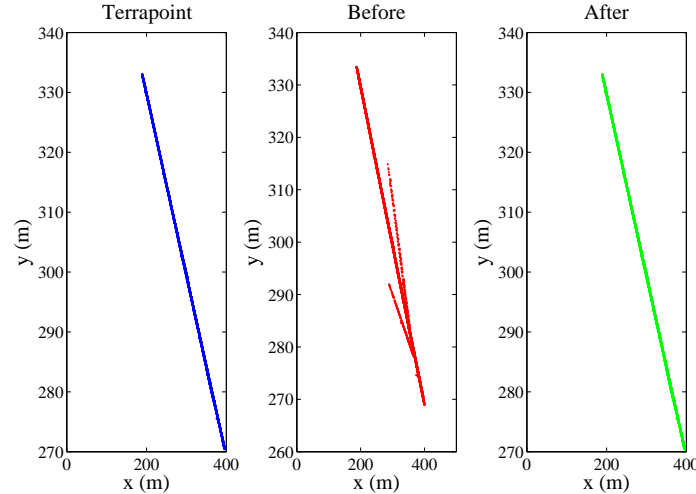


Figure 5.17: The $x - y$ plane of the bridge side reconstructed

Table 5.5: The results of the plane-based calibration using groups of planes in parallel and orthogonal drive lines

	Group 1		Group 1 and 2 (\parallel drive lines)	
	est. value ($^\circ$)	σ ($^\circ$)	est. value ($^\circ$)	σ ($^\circ$)
α	94.7588	0.2020	94.7255	0.2021
β	5.2021	0.7553	5.1104	0.7502
γ	8.0182	0.1309	7.97792	0.1292
	Group 1 and 3 (\perp drive lines)			
α			93.6665	0.2398
β			-0.9065	0.2624
γ			8.6690	0.0214

5.2.4 Examination of the Plane-based Calibration Using 24 planes

The 56 planes used in calibration for the last section are not captured by the system travelled in orthogonal drive lines for Scanner 1 and 2. The calibration results (Table 5.6) presented in this section is based on 24 (12 planes were captured with the system travelled in parallel drive lines while the other 12 planes were captured with the system travelled in orthogonal drive lines). Reducing the input planes from 56 to 24 should result in much less rigorous calibration as the redundancy is reduced more than a half. However, the results shows that the estimation of Scanner 1 and 2 are approximately

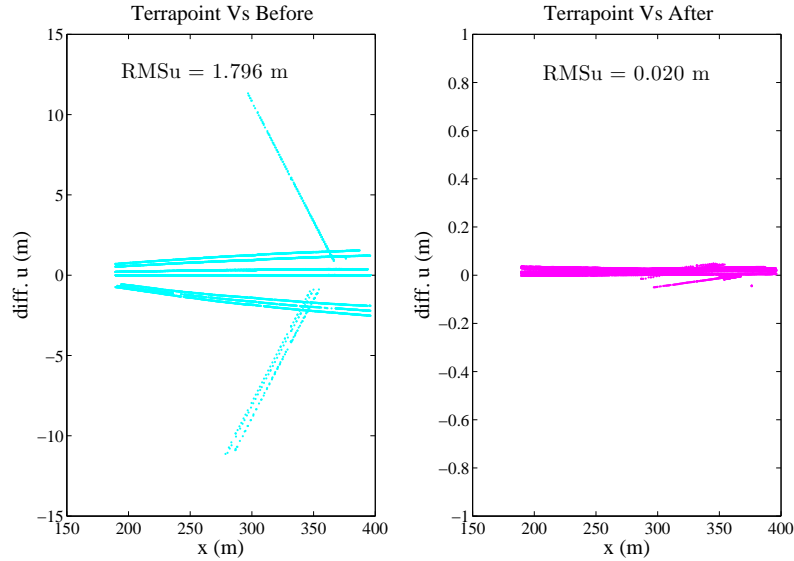


Figure 5.18: The difference of the $x - y$ position of the bridge side in terms of u , where $u = \sqrt{x^2 + y^2}$

the same and this suggests that the robustness of the estimation of Scanner 1 and 2's boresights by the data captured by orthogonal drive lines. The estimation of Scanner 1 and 2 can even have higher overall precisions. However, there are apparent discrepancies for the estimated boresights of Scanner 3 and 4, this is presumably due to the reduced overlap regions between Scanner 1, 2 and 3, as well as between Scanner 1, 2 and 4 as the number of the overall input planes is reduced.

5.2.4.1 Accuracy Analysis

The RMSs of fittings of the 28 test planes reconstructed by the boresight estimated using the 24 planes are compared with that of using the 56 planes in Figure 5.21. It can be seen that the RMSs are effectively the same. The same analysis as given in Figure 5.15 and 5.18 are repeated with the boresight solved using the 24 planes, the results are compared with the boresight of the 56 planes and are shown in Figure 5.22 and 5.23. The RMS_z is further reduced from 0.019 m to 0.014 m. There is only an increment of 6 mm in RMS_u and therefore the performance of the two calibrations are effectively the same.

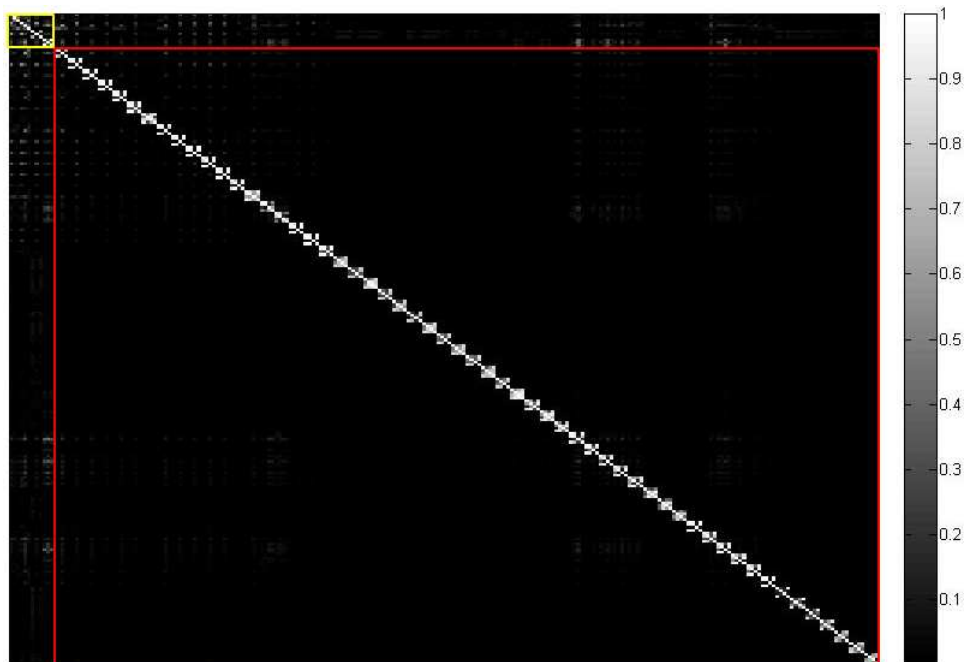


Figure 5.19: Correlation Matrix of plane-based calibration adjustment using 56 planes. The yellow highlights the boresight parameters, the red highlights the plane parameters

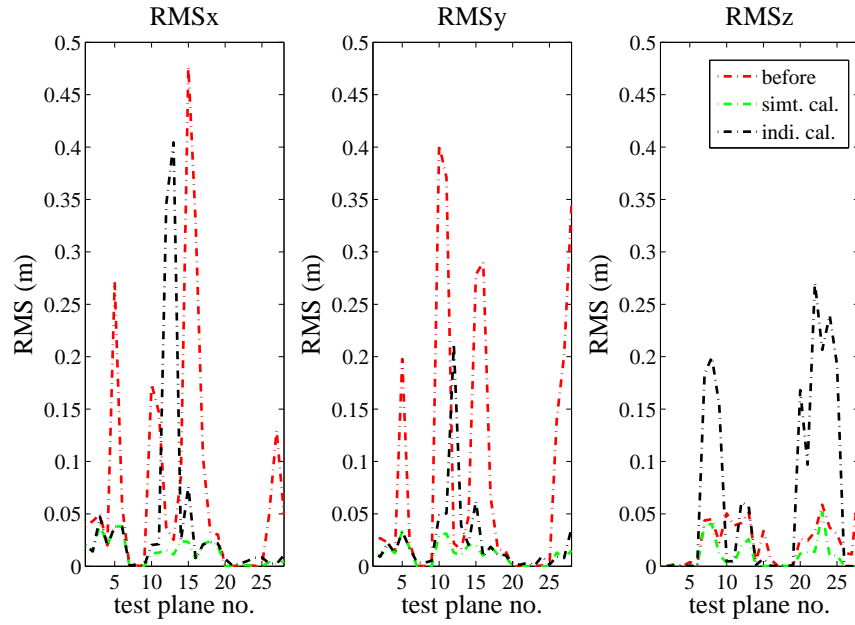


Figure 5.20: RMS of the test plane fitting with the point cloud of before, after calibration with 56 planes and calibration with 56 planes independently

Table 5.6: Results comparison of the plane-based calibration using 56 and 24 planes

Scanner	Boresight	Estimated Values			
		56 planes($^{\circ}$)	σ_{56p} ($^{\circ}$)	24 planes($^{\circ}$)	σ_{24p} ($^{\circ}$)
1	α	90.1405	0.0104	90.1684	0.0085
	β	0.0623	0.0167	-0.0063	0.0187
	γ	8.8078	0.0019	8.7536	0.0039
2	α	270.4021	0.0129	270.3651	0.0099
	β	-0.5761	0.0196	-0.5427	0.0159
	γ	-8.6701	0.0030	-8.6573	0.0028
3	α	0.9766	0.0551	1.1814	0.0521
	β	-69.7423	0.0143	-69.7784	0.0129
	γ	-1.5316	0.3776	-1.9462	0.3462
4	α	-1.5255	0.1979	-0.9392	0.1595
	β	130.1442	0.0104	130.0864	0.0115
	γ	178.7314	0.1435	179.1083	0.1153

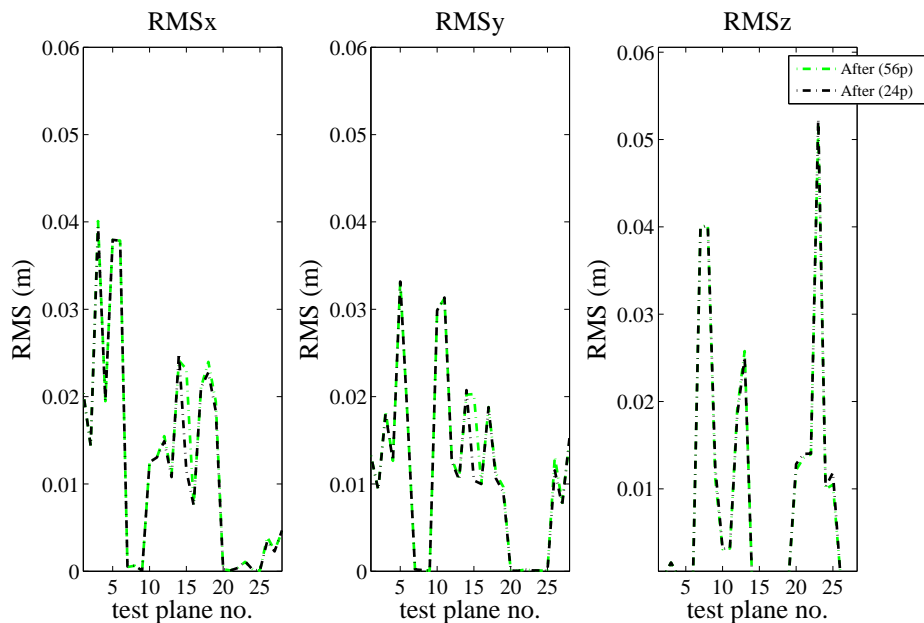


Figure 5.21: RMS of the test plane reconstructed from the boresight of calibration using 56 planes (without \perp drive lines) and 24 planes (with \perp drive lines)

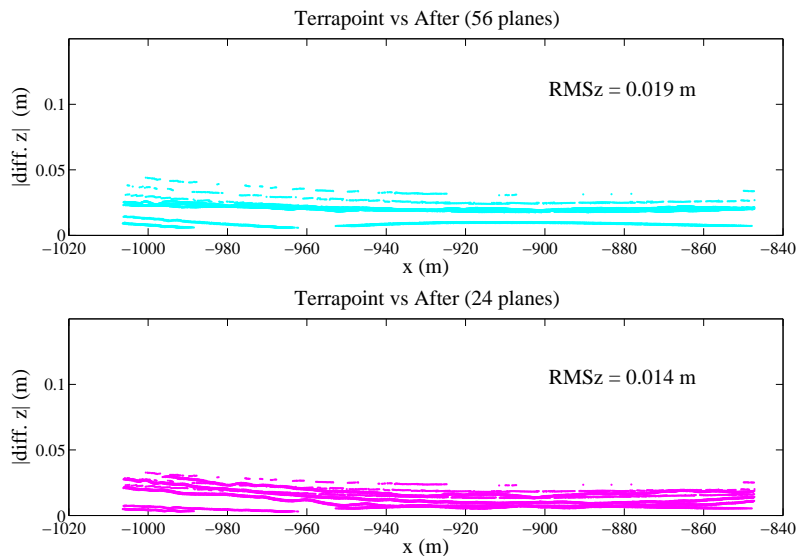


Figure 5.22: The difference in z of the horizontal profile

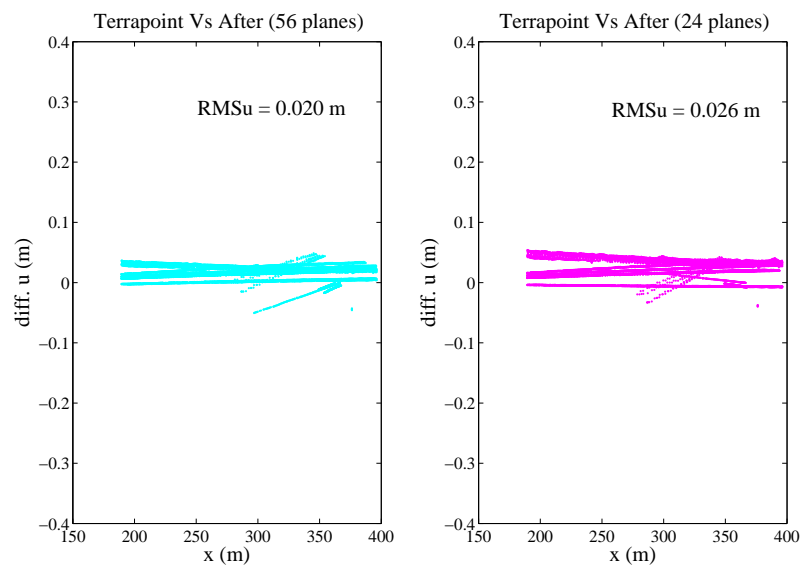


Figure 5.23: The difference of the $x - y$ position of the bridge side in terms of u , where $u = \sqrt{x^2 + y^2}$

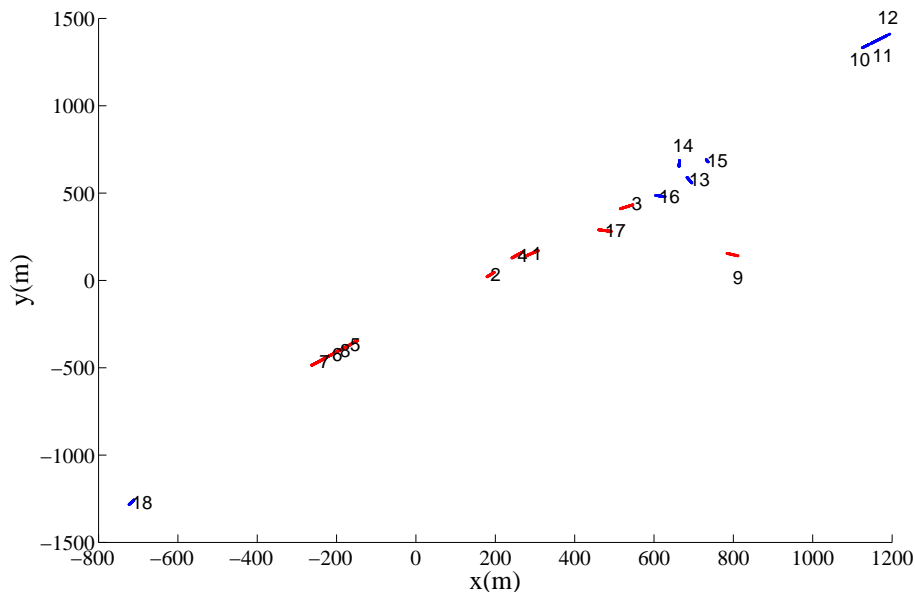
5.3 Results of Catenary-based Calibration

5.3.1 Calibration with 15 Catenaries: Group 1 and 2

Point clouds of eighteen hanging power cables (no. 1-18) were extracted from the dataset for calibration and their $x - y$ positions are shown in Figure 5.24. All the eighteen cables were then examined for their degree of symmetry by evaluating the ΔH_n introduced in Chapter 4 and the results are shown in the Table 5.7. By checking the length and also the ΔH_n , catenaries no. 1, 8 and 14 were identified as extremely asymmetric catenaries that will cause high correlations between the parameters (b_c and c_c) for the calibration or fitting. Therefore, these three catenaries were then discarded and the rest were further examined for their RMS in the z direction (RMS z) after the outlier removal. The results are shown in Table 5.8. It is expected that catenaries which are further away from the system will incur a higher RMS z as the combined effect of the rangefinder error and the encoder angle error increase with the range. All the remaining 15 catenaries are further divided into two groups (Group 1: with average range less than 20 m and with relatively smaller RMS z ; and Group 2: with average range more than 20 m and with relatively higher RMS z) for the calibration.

Table 5.7: The normalized height difference of the input catenaries

Cable	L(m)	ΔH_n	Cable	L(m)	ΔH_n
1	44.101	0.046	10	44.802	0.013
2	31.622	0.024	11	28.268	0.019
3	39.239	0.003	12	28.962	0.009
4	45.185	0.024	13	34.149	0.028
5	59.86	0.001	14	30.459	0.053
6	39.748	0.003	15	14.726	0.005
7	60.58	0.005	16	25.498	0.003
8	17.77	0.063	17	33.18	0.001
9	31.067	0.023	18	28.902	0.018

Figure 5.24: The $x - y$ position of the 18 catenariesTable 5.8: RMS z of input catenary fitting

Cable	Total Pts.	Blunder	Pts. for Cal.	Avg. ρ (m)	RMS z (m)	$\hat{\sigma}_o$
2	277	3	274	15.137	0.05	1.049
3	179	3	176	15.224	0.046	0.887
4	453	2	451	8.789	0.044	0.815
5	557	0	557	8.991	0.041	0.689
6	404	0	404	9.239	0.04	0.654
7	629	0	629	9.308	0.04	0.644
9	73	7	66	8.865	0.077	2.526
10	110	42	68	39.685	0.124	6.427
11	66	26	40	39.775	0.095	3.8
12	41	17	24	38.68	0.1	4.306
13	132	43	89	29.038	0.111	5.144
14	184	83	101	32.799	0.124	6.313
16	66	42	24	31.396	0.187	14.858
17	309	18	291	15.444	0.053	1.15
18	158	69	89	40.894	0.109	4.873

5.3.1.1 Parameter Estimation

Table 5.9 shows the calibration results using Group 1 (8 catenaries with average $\rho < 20$ m) and also the results using both the Group 1 and Group 2 (7 catenaries with average $\rho > 20$ m). The two estimated values of the boresights are very close to each other. As briefly mentioned in Chapter 3, the hanging cables are mainly captured by Scanner 1 and 2 as the cables are located in the two sides of the trajectory and the heights of the system and the catenary are compatible (Figure 5.25). Only very few measurements at the two ends of the catenaries are given by Scanner 4. Scanner 3 points toward the ground and therefore it cannot scan the hanging cables. As a result, only the boresights of Scanner 1 and 2 will be estimated with the catenary features.

Figure 5.26 shows the residuals of the catenary-based calibration adjustment. As with the plane-based calibration, the residual distributions are centred around zero. This indicates that the model for the adjustment is appropriate. The overall precision of the estimation is worse than that of the plane-based. This might be attributed to the fact that the degrees of freedom (DOF) of the catenary-based (15 catenary with $\text{DOF} = 3643$) is much smaller than that of the plane-based (56 planes with $\text{DOF} = 53742$).

It can be noted that the estimated β of Scanners 1 and 2 show relatively larger deviations compared to that of the plane-based calibration. As already explained in section 5.2.1, the z measurement of the vertical planes do not contribute significantly to the estimation of β . However, this is opposite in the case of the catenary. Unlike adjusting the parameters of the vertical planes, adjusting the catenary parameters can affect the estimation of β . Comparing the RMSs in the x , y and z directions when fitting a 3D catenary point cloud is performed, the RMS_z is much higher than the RMS_x and the RMS_y . The uncertainty in the z direction propagates into β and thus β has the lowest

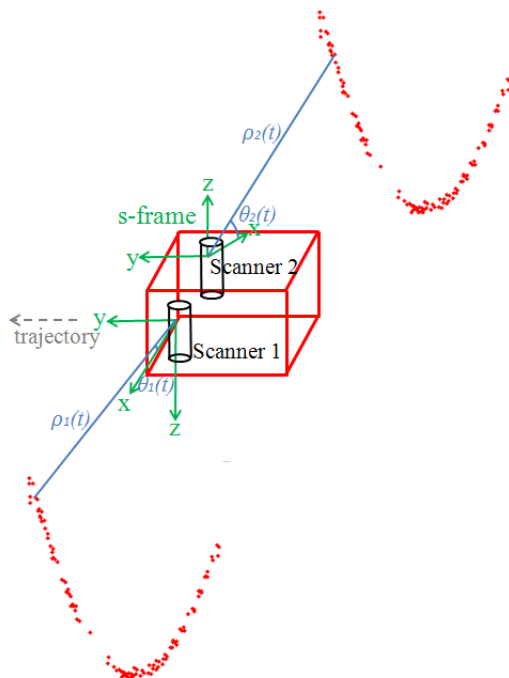


Figure 5.25: Scanner 1 and 2 scan the catenaries

precision. α is associated with both the x and z measurement and combined effect of the x and z measurement leads to the highest precision of α . γ is associated only with the x -measurement, so it has lower precision than α .

Table 5.9: Catenary-based calibration results with Group 1 and 2 catenaries

Catenary			Group 1 (8 cat'y)		Group 1+2 (15 cat'y)	
Scanner		Terrapoint values($^{\circ}$)	Estimated values($^{\circ}$)	Estimated $\sigma(^{\circ})$	Estimated values($^{\circ}$)	Estimated $\sigma(^{\circ})$
1	α	90.2388	90.2682	0.0131	90.2671	0.0136
	β	0.0207	-0.4528	0.4063	-0.5002	0.3673
	γ	8.7677	8.7491	0.1158	8.7191	0.1016
2	α	270.3228	270.2894	0.0291	270.2812	0.0223
	β	0.0004	-0.9261	1.0409	-0.9890	0.6682
	γ	-8.7277	-8.6632	0.2827	-8.6201	0.1931
	$\hat{\sigma}_o$		0.3582		0.3681	

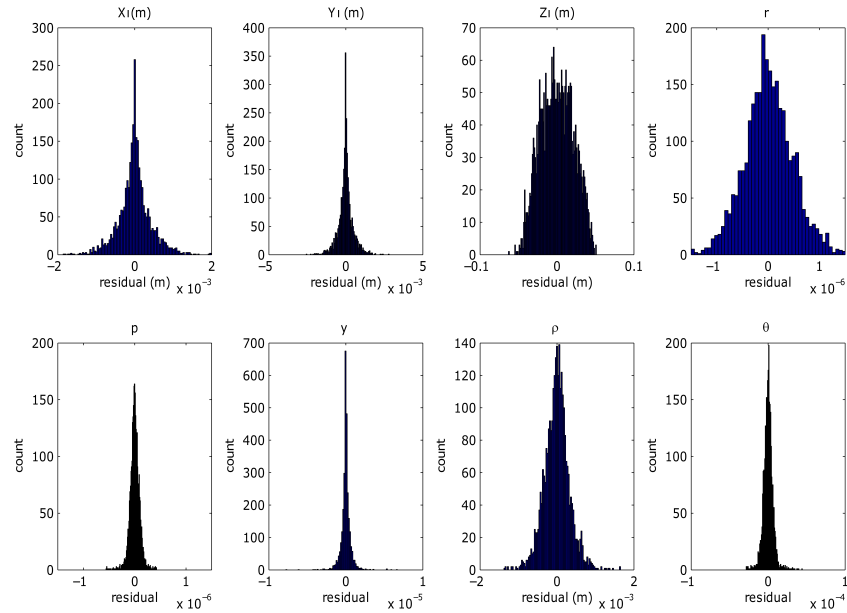


Figure 5.26: The residuals of catenary-based calibration adjustment using 15 catenaries

5.3.1.2 Accuracy Analysis

5.3.1.2.1 RMS with Test Catenary Fitting

Table 5.10 shows that RMS in the z direction for fitting 10 test catenaries (extracted outside the calibration zones) with the power cable point clouds reconstructed from the boresight values from the Terrapoint's calibration, also the plane-based Group 1 and 2 (15 catenaries). The results show that their RMS_z only differ at the millimetre-level and therefore all the three calibrations perform effectively the same.

5.3.1.2.2 Profile Analysis

The same horizontal profile of the concrete bridge side is used for testing the estimated boresight values with the catenary-based calibration and Figure 5.18 is duplicated with the boresights of the calibration using the 15 catenaries and is presented in Figure 5.27. It can be seen that the $x - y$ position deviates more ($RMS_u = 0.03$ m) from the Terrapoint compared to the calibration using the 56 planes. The density of the catenary point cloud,

Table 5.10: RMS z of 10 test catenaries

test cat'y	Terrapoint	Plane-based	Catenary-based
	RMS z (m)		
1	0.093	0.098	0.093
2	0.094	0.103	0.093
3	0.090	0.098	0.089
4	0.115	0.110	0.115
5	0.114	0.110	0.114
6	0.101	0.097	0.101
7	0.095	0.097	0.093
8	0.102	0.108	0.101
9	0.099	0.104	0.100
10	0.092	0.093	0.092

and thus the DOF of catenary is much smaller than that of planes. This results in less accurate and precise estimation of the boresights.

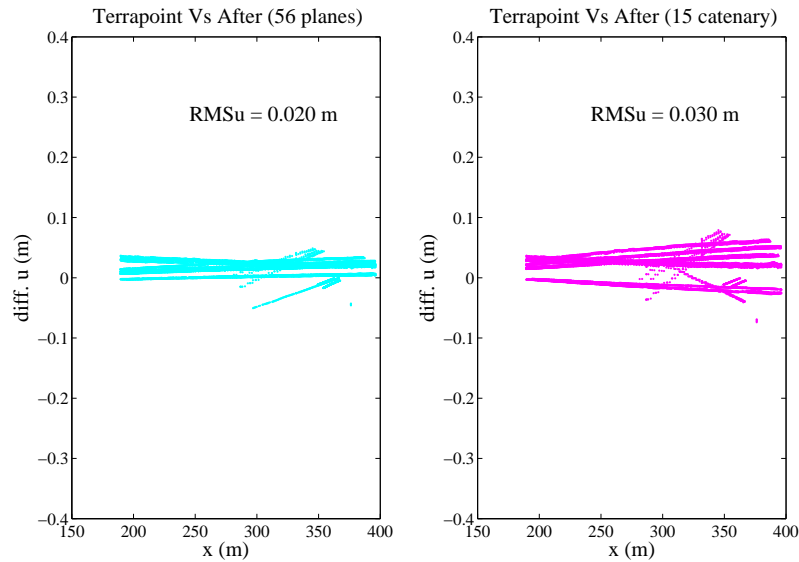


Figure 5.27: The difference of the $x - y$ position of the bridge side in terms of u , where $u = \sqrt{x^2 + y^2}$

5.3.1.3 Parameter Correlation

Figure 5.28 shows the correlation matrix (absolute values taken) of the calibration using the 15 catenaries (Group 1 and Group 2). In this Figure, the correlation coefficients of

the boresight of Scanners 1 and 2 is highlighted with yellow ($\alpha_1, \beta_1, \gamma_1, \alpha_2, \beta_2, \gamma_2$) and the catenary parameters are highlighted with green (dash line for Group 1 ($a_{c1}, b_{c1}, c_{c1}, \dots, a_{c8}, b_{c8}, c_{c8}$) and the rest for Group 2 ($a_{c9}, b_{c9}, c_{c9}, \dots, a_{c15}, b_{c15}, c_{c15}$)). It can be seen that the high correlation between α of Scanner 1 and 2 (maximum is 0.81), and also between both the α and the a_c parameters, and also some moderate correlation between the same parameters for the Group 1. The average range measurement of the Group 2 is about 40 m which is approximately the double of that of the Group 1. Therefore, this suggests that the the higher correlation exists between α and the a_c parameters of Group 2 is due to the larger range. This is because when as the range increases, the effect of adjusting the α on the z -measurement increases. The geometry of α and a_c is shown in Figure 5.29 and from that it can be seen α and a_c are geometrically correlated.

5.3.2 Calibration Results using Two Catenaries with Parallel and Orthogonal Drive Lines

In order to specifically investigate the correlation between parameters and the geometry of the catenaries, two pairs of catenaries are selected from Group 1 catenary to solve the boresights of Scanner 1 and 2: Catenary 2 and 3; and Catenary 2 and 17. Catenary 2 and Catenary 3 were captured on the same highway and therefore they are almost parallel while Catenary 17 was captured on the bridge, thus it is rather close to “orthogonal” to Catenary 2 as illustrated in Figure 5.30. Table 5.11 shows the calibration results using Catenary 2 and 3 (parallel case), and also that using Catenary 2 and 17 (orthogonal case).

Compared to the estimated values of the plane-based calibration (Table 5.5), α and γ seem being well estimated with only using 2 catenaries comparing to using 6 planes. This can be explained by the fact that the x and y coordinates are in collinearity for the 3D

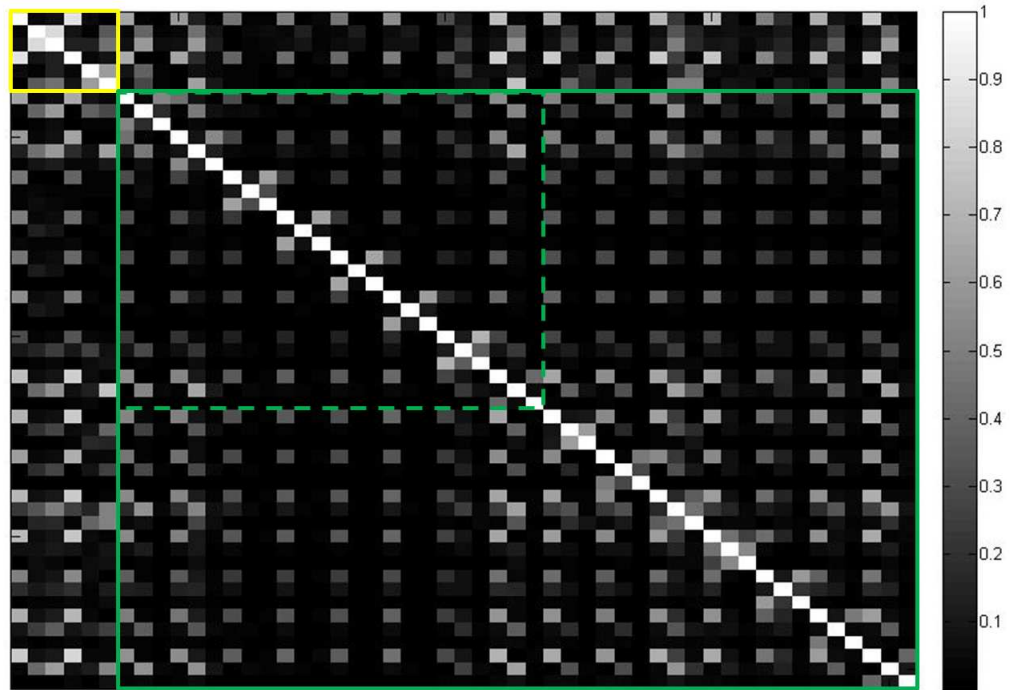


Figure 5.28: Correlation Matrix (absolute value taken) of the catenary-based calibration using the 15 catenaries (Group 1 and Group 2), the yellow highlights the boresight parameters and the green highlights the catenary parameters

catenary model and thus the x and y -measurements contribute to the rotation of the catenary (the rotation is about the vertical axis that passes through the $x - y$ centroid of the catenary). This rotation can solve the γ effectively. Apart from this, α is associated with both the x and z measurement, therefore, both the rotation and the z -measurement of the catenary contribute to its estimation. Two catenaries seem able to solve α and γ quite accurately.

The correlation coefficients of the above two calibrations are shown in the correlation matrix in Figure 5.31. It can be seen that the \perp case reduced the correlation between α and a_c .

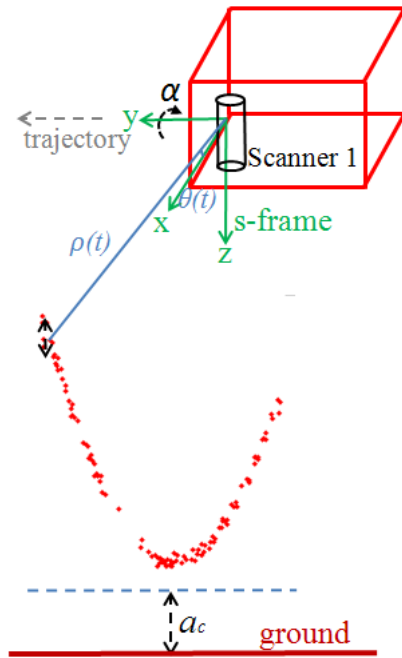


Figure 5.29: The geometry of α and a_c

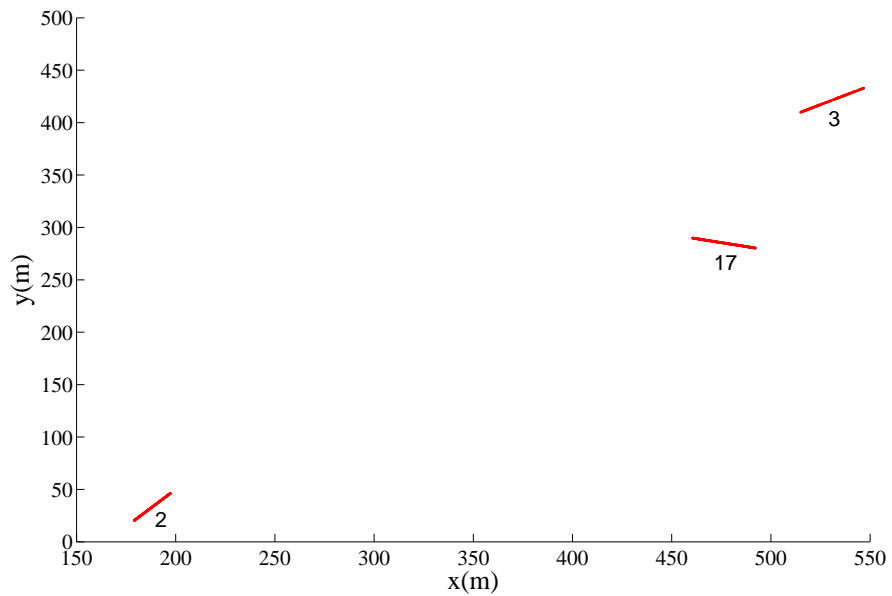


Figure 5.30: The x-y position of the catenaries

Table 5.11: Calibration results of catenary-based calibration using 2 catenaries

Catenary			(no. 2 \perp 17)		(no. 2 \parallel 3)	
Scanner	Terrapoint values($^{\circ}$)		Estimated values($^{\circ}$)	Estimated σ ($^{\circ}$)	Estimated values($^{\circ}$)	Estimated σ ($^{\circ}$)
1	α	90.2388	90.2341	0.0261	90.2417	0.0382
	β	0.0207	2.0668	3.2271	1.8050	2.4259
	γ	8.7677	8.5044	0.4725	8.6611	0.3331
2	α	270.3228	270.3572	0.0427	270.3393	0.0715
	β	0.0004	-3.6044	2.9533	-2.7424	2.2054
	γ	-8.7277	-8.9878	0.5318	-8.8491	0.5425
	$\hat{\sigma}_o$		0.4062		0.4018	

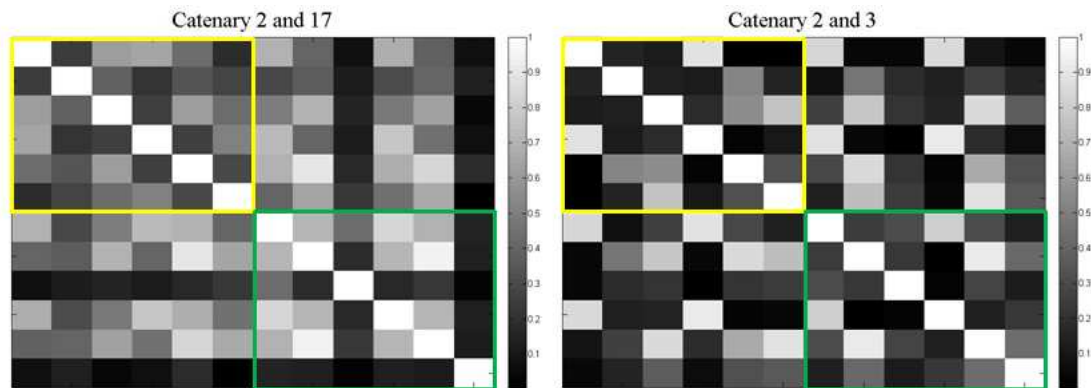


Figure 5.31: Correlation Matrix of the catenary-based calibration using only Catenary 2 and 17 (\perp case) and Catenary 2 and 3 (\parallel case), the yellow highlights the boresight parameters and the green highlights the catenary parameters

5.4 Results of Mixed Feature-based Calibration

In this section, the 56 planes are first combined with the 15 catenaries for the calibration adjustment (mixed feature-based calibration). The estimated boresights are almost the same as those from only using the 56 planes because the redundancy of the 56 planes (over 50000) is much larger than that of the 15 catenaries (approximately 3000). The results of using the 24 planes and the 15 catenaries are analysed instead and the redundancy of the 24 planes is approximately 18000. The results are compared with the calibration only using the 24 planes in Table 5.12. Adding the 15 catenaries to the 24 planes brings the estimated values of Scanners 1, 2, 3 closer to the Terrapoint's values. However, the overall precision is slightly reduced.

Table 5.12: Results comparison of the plane-based calibration (24 planes) and the mixed feature-based calibration (24 planes and 15 catenaries)

Scanner	Boresight	Terra- point(°)	Estimated Values			
			24 planes(°)	σ_{24p} (°)	24 planes + 15 catenary(°)	σ_{24p15c} (°)
1	α	90.2388	90.1684	0.0085	90.2441	0.0082
	β	0.0207	-0.0063	0.0187	0.0202	0.0232
	γ	8.7677	8.7536	0.0039	8.7574	0.0047
2	α	270.3228	270.3651	0.0099	270.3153	0.0111
	β	0.0004	-0.5427	0.0159	-0.3375	0.0196
	γ	-8.7277	-8.6573	0.0028	-8.6721	0.0034
3	α	0.8464	1.1814	0.0521	1.1942	0.0625
	β	-69.8769	-69.7784	0.0129	-69.8381	0.0147
	γ	-0.9728	-1.9462	0.3462	-2.0292	0.4138
4	α	0.2947	-0.9392	0.1595	0.4237	0.1990
	β	129.9668	130.0864	0.0115	129.7753	0.0155
	γ	180.0676	179.1083	0.1153	180.1062	0.1439

5.4.1 Accuracy Analysis

5.4.1.1 RMS of the Test Plane Fitting

The RMSs of fittings of the 28 test planes of the mixed feature-based calibration are presented in Figure 5.32 along with the previous calibration results. It is shown that the the mixed feature-based calibration performs slightly better than the 24 plane-based calibration in terms of plane fitting in a few cases.

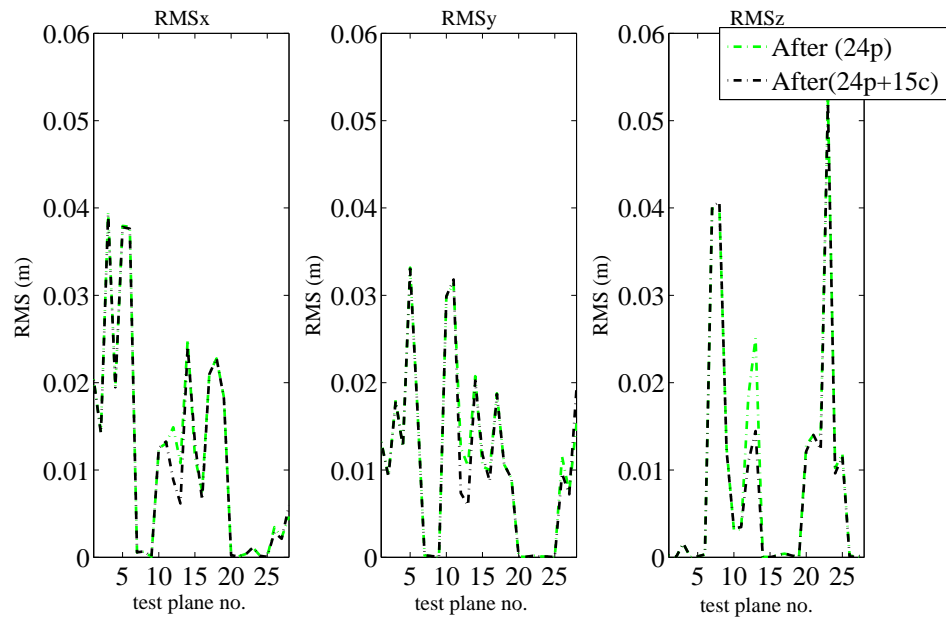


Figure 5.32: RMSs of the test plane fitting

5.4.1.2 Profile Analysis

The relative vertical and horizontal accuracy can be analysed by investigating Figure 5.33 and 5.34 which are reproduced by the profiles from the estimated boresights of the mixed feature-based calibration. It can be seen that after 15 catenaries are added to the 24 planes for the calibration, the RMS_z is reduced to 6 mm while the RMS_u is slightly increased by 1 mm.

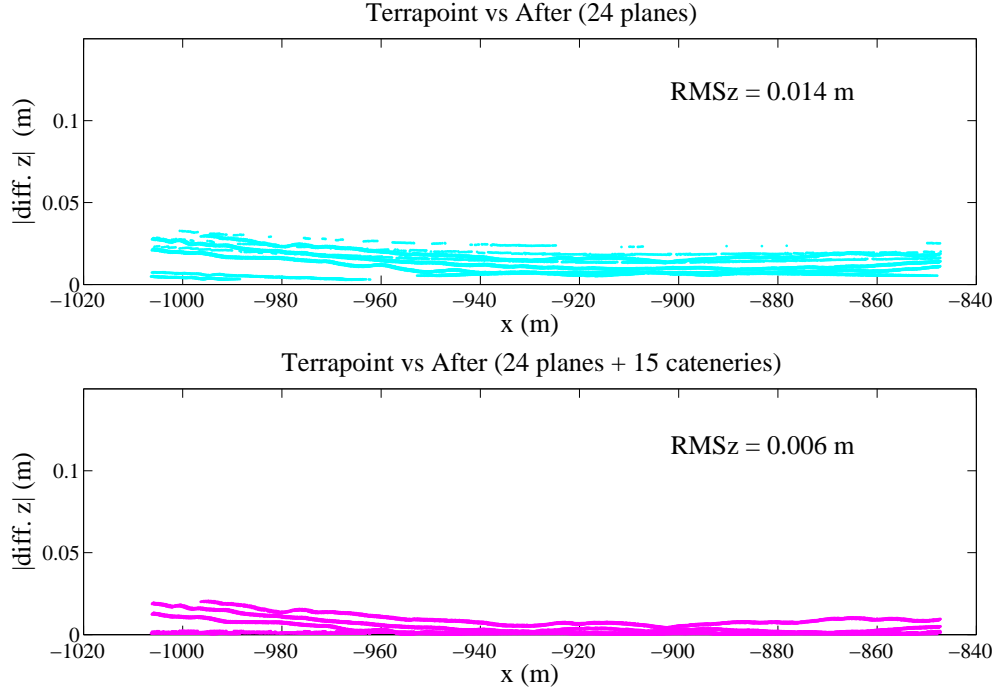


Figure 5.33: The difference in z of the horizontal profile

5.4.2 Parameter Correlation

The correlation matrix of the calibration is shown in Figure 5.35. (The yellow region is for boresight of Scanners 1 - 4, $\alpha_1, \beta_1, \gamma_1, \dots, \alpha_4, \beta_4, \gamma_4$; the red region is for the 24 planes' parameters, $a_{p1}, b_{p1}, c_{p1}, d_{p1}, \dots, a_{c24}, b_{c24}, c_{c24}, d_{p24}$; and the green region is for the 15 catenaries' parameters, $a_{c1}, b_{c1}, c_{c1}, \dots, a_{c15}, b_{c15}, c_{c15}$). It is found that the high correlation coefficients 0.81 (the maximum) between α and a_c are reduced to 0.44 (the maximum). The maximum correlation coefficient between the boresights of Scanner 1 - 4 is 0.66.

In conclusion, the mixed feature-based calibration tends to be more rigorous compared to either plane- or catenary-based calibration as shown by the reduced RMSs of independent planes fitting and also the compatible positioning accuracy with the Terrapoint's

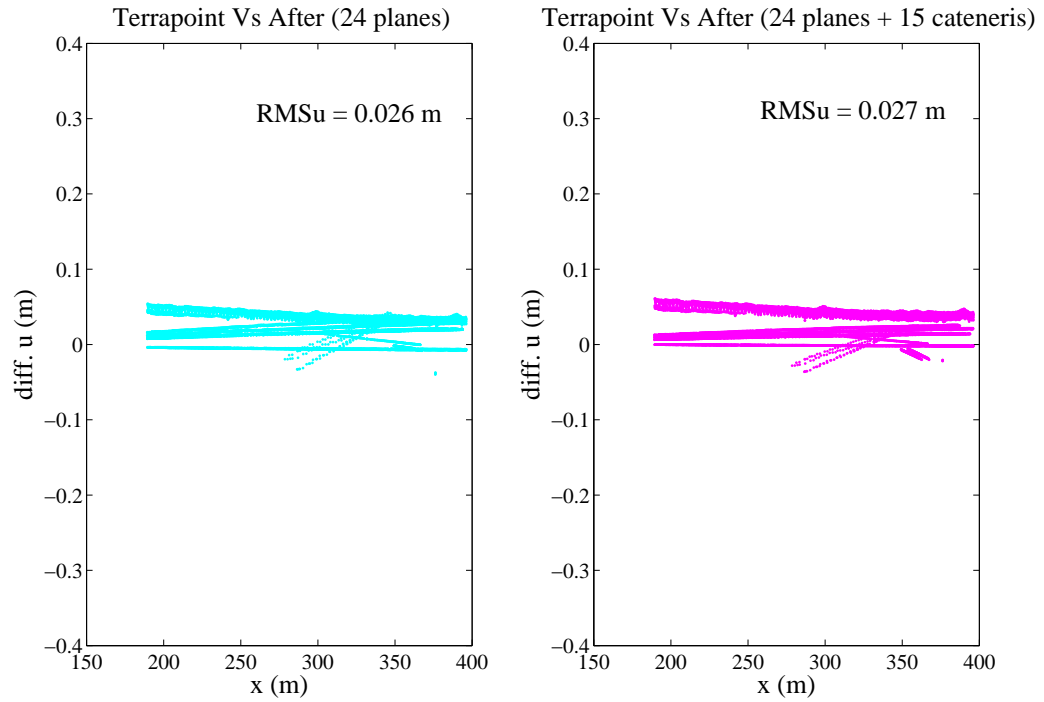


Figure 5.34: The difference of the $x - y$ position of the bridge side in terms of u , where $u = \sqrt{x^2 + y^2}$

dedicated calibration. The adjustment is also more reliable than the catenary-based calibration adjustment as the high correlation between the α and a_c is reduced.

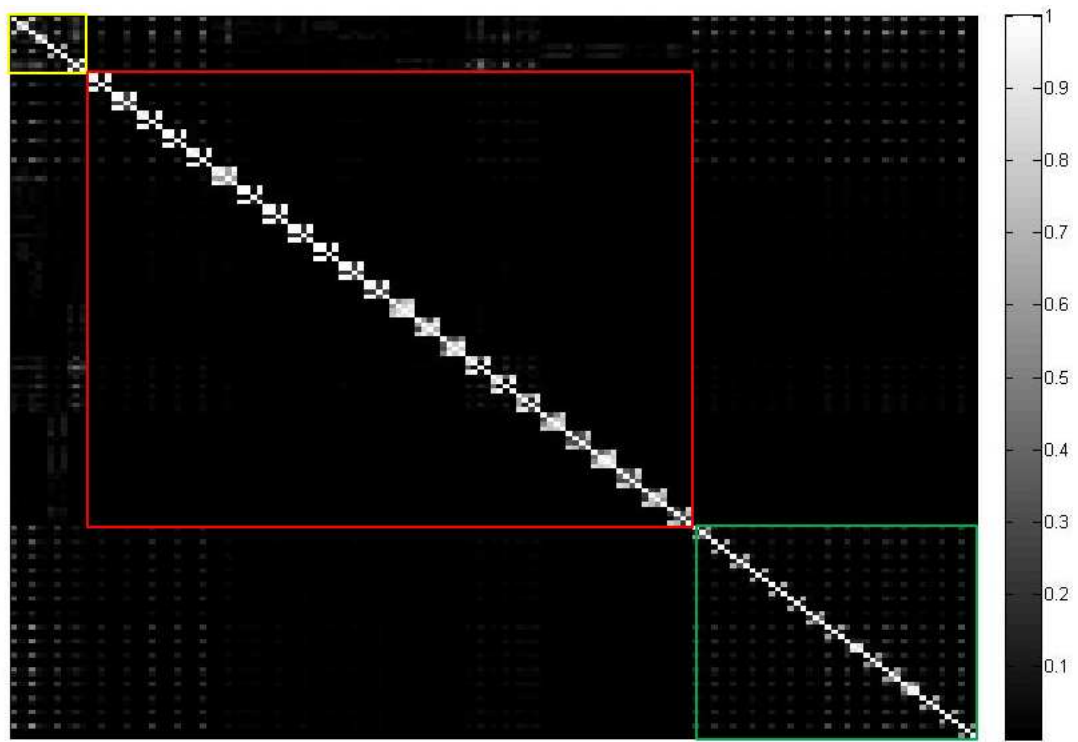


Figure 5.35: Correlation Matrix with calibration solving boresights with 24 planes and 15 catenaries. The yellow highlights the boresight parameters, the red highlights the plane parameters and the green highlights the catenary parameters

Chapter 6

Conclusions and Recommendations for Future Works

6.1 Conclusions

This research proposed a new multi-feature, multi-scanner boresight calibration methodology for laser scanner-based MMSs. A detailed analysis for calibration results has been presented and an attempt is made to cover analysis of the geometry of scanners and input features. The proposed methodology have been thoroughly investigated for its accuracy in term of feature fitting, and vertical and horizontal positioning of a long profile based on the reference calibration results (Terrapoint developed plane-calibration using around 350 planes). Using 24 planes captured by the system travelled in orthogonal drive lines and 15 catenaries for the calibration leads to an average RMS of independent plane fittings in the vertical and horizontal directions of approximately 2.5 cm and 3 cm respectively. Moreover, by treating the point cloud reconstructed by the Terrapoint's calibration results as the ground truth, the mixed feature-based calibration with 24 planes and 15 catenaries gives approximate accuracy of 27 mm and 6 mm for horizontal and vertical positioning respectively. No high correlations were found between the the boresight parameters and the features parameters (maximum correlation coefficient is 0.44) and also between the boresights of the four scanners (maximum correlation coefficient is 0.66).

The major new contributions of this research have already be presented in section 1.3 of Chapter 1 and therefore are not repeated here. Some important findings, worth noting throughout this research are summarized as follows:

1. Simultaneous estimation of the boresight angles of multiple scanners using planar features is shown to be more rigorous than individual estimation of the boresights of a single scanner. Point clouds of the same object captured by multiple scanners could provide more control to each other during the calibration adjustment.
2. The analysis of the geometry of the scanners and the planar features in this research showed that a boresight angle can be effectively adjusted if planes are orientated differently at the same level as the rotation of the boresight angle. That means adjusting α about the y -axis should be achieved by adjusting or rotating vertical planes in $x - z$ planes, while for adjusting γ about the z -axis should be achieved by adjusting or rotating vertical planes in $x - y$ planes. However, it should be noted that β cannot be adjusted by rotating planes at the same level as β about the x -axis because such the rotation of the planes will keep the direction cosine unchanged and the planes are basically the same in terms of the orientation. This is the reason why the precision of β of Scanner 1 and 2 was the lowest.
3. The analysis of the geometry of the scanners and the planar features in this research also showed at least two planes in different orientations are needed to adjust one boresight angle.
4. The boresights of the scanner pointing toward the ground surface (Scanner 3) are the most difficult to estimate as the input plane features for it are only the ground surfaces and solving boresights of the Scanner 3 independently is shown to be impractical. However, as the ground surfaces had an overlap regions between Scanner 1 and 3, and also between Scanner 2 and 3, the simultaneous multi-scanner calibration using the planar features is shown to be practical and rigorous.
5. With the new 3D model of the catenary proposed by the author in Chan and Lichti

(2011), asymmetric catenaries should be discarded for calibration or fitting due to the extremely high parameter correlation (the coefficient can be larger than 0.9).

6. When solving the boresight with catenaries, α about the y -axis (pointing toward the navigating direction) was found to be highly correlated with a_c (the vertical translation) of the catenary (maximum correlation coefficient = 0.81). This correlation increases as the range increases (the catenary is further away from the scanner). The deviation from the parallelity of catenaries will reduce the correlation.
7. Only two catenaries in parallel directions in the catenary-based calibration have been shown to be necessary to solve α and γ quite accurately.
8. It was found that the accuracy and precision of β for catenary-based catenary highly depends on the accuracy of the z -measurement of the catenary.
9. It was shown that the mixed feature-based calibration is practical. It includes two different geometric features and therefore the correlation between the boresights and the features parameters (planar and catenary feature parameters) was reduced.

6.2 The Advantages of the Developed Calibration Method

The advantages of the calibration developed in this research are summarized as the following:

1. Planar and catenary features are abundant in many highway scenes. Therefore, the calibration can be conveniently carried out without setting up control points and is suitable for in-situ calibration. Therefore, it is cost effective and flexible.
2. This calibration method can be applied to datasets captured in rural areas where the number of planar features (building façades) is not always sufficient but some catenary features (hanging power cables) are available.

3. Simultaneous adjustment reduces the number of planes needed to achieve high accuracy. Only using 24 planes can produce similar results to the Terrapoint plane-based calibration (350 planes).
4. Only two parallel catenaries are needed to give a reasonably approximate estimation of the boresights. This is better than only using planes as only using two planes is not sufficient to solve three boreisight angles. The catenary-based calibration is potentially a prompt and efficient way to obtain approximate boresight values.
5. As mentioned earlier, the mixed feature-based calibration includes two different geometric features that reduces the correlation between the boresights and feature parameters. The algorithm can be readily extended to include more features such as cylinders and spheres in order to further reduce the correlation.

6.3 Recommendations for Future Works

Some future works can be associated with this research and are listed as below:

1. The calibration concept developed in this research can be potentially applied to 3D scanner-based MMSs.
2. Control points or control features might be included to evaluate the absolute positioning accuracy of the calibration.
3. Investigation of the impact of the moving speed of the system on the calibration accuracy.
4. Investigation of improving the geometric variety for the scanner pointing to the ground surface (Scanner 3).

5. More geometric features can be included from the highway scene in the adjustment.
For example, cylinder features of vertical poles.

References

- Alho, P., M. Vaaaja, A. Kukko, E. Kasvi, M. Kurkela, J. Hyyppä, H. Hyyppä, and H. Kaartinen (2011). Mobile laser scanning in fluvial geomorphology: mapping and change detection of point bars. *Zeitschrift fr Geomorphologie, Supplementbnde 55(2)*, 31 – 50.
- Angrisano, A., M. Petovello, and G. Pugliano (2010). GNSS/INS integration in vehicular urban navigation. In *GNSS/INS Integration in Vehicular Urban Navigation. Proceedings of GNSS10*, Portland, US.
- Applanix (2011). Applanix Inc. Webpage: POS LV series specifications. http://www.applanix.com/media/downloads/products/specs/POSLV_Specifications.pdf. [Online; accessed 06-Nov-2011].
- Ashtech (2011). Ashtech Inc. Webpage: High-Precision RTK without the High Cost. <http://www.ashtech.com/promark3-rtk-2655.kjsp>. [Online; accessed 06-Nov-2011].
- Bae, K. and D. D. Lichti (2007). On-site self-calibration using planar targets for terrestrial laser scanners. *International Archives of Photogrammetry, Remote Sensing and Spatial Information Sciences 37 (Part 3/W52)*, 14 – 19.
- Baltsavias, E. (1999). Airborne laser scanning: basic relations and formulas. *ISPRS Journal of Photogrammetry and Remote Sensing 54(1)*, 199 – 214.
- Bang, K. (2010). Alternative methodologies for LiDAR system calibration. *Ph.D thesis, Department of Geomatics Engineering, University of Calgary, UCGE Report No. 20317*.
- Barber, D., J. Mills, and S. Smith-Voysey (2008). Geometric validation of a ground-

- based mobile laser scanning system. *ISPRS Journal of Photogrammetry and Remote Sensing* 63, 128 – 141.
- Becker, S. and N. Haala (2009). Grammar supported facade reconstruction from mobile LiDAR mapping. *International Archives of Photogrammetry, Remote Sensing and Spatial Information Sciences* 38 (Part 3/W4), 229 – 234.
- Böder, V., T. P. Kersten, T. Thies, and A. Sauer (2011). Mobile laser scanning on board hydrographic survey vessels - applications and accuracy investigations. In *FIG Working Week 2011: Bridging the Gap between Cultures*, Marrakech, Morocco.
- Boulaassal, H. and P. Grussenmeyer (2011, May). Dataprocessing of building façades recorded by vehicle-based laser scanning. In *GTC2011 Symposium, Geomatics in the City*.
- Brown, D. C. (1971). Close-range camera calibration. *Photogrammetric Engineering* 37(8), 855 – 866.
- Burman, H. (2000). Adjustment of laser scanner data for correction of orientation errors. *International Archives of Photogrammetry, Remote Sensing and Spatial Information Sciences* 33 (Part B3), 125 – 132.
- Chan, T. and D. D. Lichti (2011). 3D catenary curve fitting for geometric calibration. *International Archives of Photogrammetry, Remote Sensing and Spatial Information Sciences* 38 (Part 5/W12), [On CD-ROM].
- Chow, J., A. Ebeling, and W. Teskey (2010). Low cost artificial planar target measurement techniques for terrestrial laser scanning. In *FIG Congress 2010: Facing the Challenges - Building the Capacity*, Sydney, Australia.

- Chow, J., D. D. Lichti, and C. Glennie (2011). Point-based versus plane-based self-calibration of static terrestrial laser scanners. *International Archives of Photogrammetry, Remote Sensing and Spatial Information Sciences 38 (Part 5/W12)*, [On CD-ROM].
- Cothren, J. (2005). Reliability in constrained gauss-markov models: An analytical and differential approach with applications in photogrammetry. *Ph.D thesis, Department of Civil and Environmental Engineering and Geodetic Science. The Ohio State University.*
- Dow, J., R. E. Neilan, and C. Rizos (2009). The international GNSS service in a changing landscape of global navigation satellite systems. *Journal of Geodesy 83*, 191 – 198.
- El-Halawany, S. and D. D. Lichti (2011). Detection of road poles from mobile terrestrial laser scanner point cloud. In *2011 International Workshop on Multi-Platform/Multi-Sensor Remote Sensing and Mapping*, Xiamen, China. [On CD-ROM].
- El-Sheimy, N. (1996). The development of visat - a mobile survey system for gis applications. *Ph.D thesis, Department of Geomatics , University of Calgary, UCGE Report No. 20101.*
- El-Sheimy, N. (2003). Mapping systems: The new trend in mapping and GIS applications. http://www.fig.net/pub/cairo/ppt/ts_17/ts17_03_elsheimy_ppt.pdf. [Online; accessed 06-Nov-2011].
- El-Sheimy, N. (2005). An overview of mobile mapping systems. In *FIG Working Week 2005 and GSDI-8*, Cairo, Egypt.
- Farrell, J. and M. Barth (1999). *The Global Positioning System and Inertial Navigation*. McGraw-Hill Publishing.

- Filin, S. (2003). Recovery of systematic biases in laser altimetry data using natural surfaces. *Photogrammetric Engineering and Remote Sensing* 69, 1235 – 1242.
- Glennie, C. (2007a). Reign of point clouds: a kinematic terrestrial LiDAR scanning system. *InsideGNSS Fall 2007*, 22 – 32.
- Glennie, C. (2007b). Rigorous 3D error analysis of kinematic scanning LiDAR systems. *Journal of Applied Geodesy* 1, 147 – 157.
- Glennie, C., K. Kusevic, and P. Mrstik (2006). Performance analysis of a kinematic terrestrial lidar scanning system. In *Proceedings of MAPPS/ASPRS Fall Conference*, San Antonio, USA.
- Glennie, C. and D. D. Lichti (2010). Static calibration and analysis of the Velodyne HDL-64E S2 scanner for high accuracy mobile scanning. *Remote Sensing* 2(6), 1610 – 1624.
- Glennie, C. and D. D. Lichti (2011). Temporal stability of the Velodyne HDL-64E S2 scanner for high accuracy scanning applications. *Remote Sensing* 3(3), 539 – 553.
- Grejner-Brzesinska, D., R. Li, N. Haala, and C. Toth (2004). From mobile mapping to telegeoinformatics: Paradigm shift in geospatial data acquisition, processing, and management. *Photogrammetric Engineering and Remote Sensing* 70(2), 197 – 210.
- Grejner-Brzezinska, D. A. (2001). Direct sensor orientation in airborne and land-based mapping application. *Report No. 461, Geodetic GeoInformation Science, Department of Civil and Environmental Engineering and Geodetic Science. The Ohio State University.*
- Grewal, M. S., L. R. Weill, and A. P. Andrews (2007). *Global Positioning Systems, Inertial Navigation, and Integration, 2nd Edition*. John Wiley & Sons, Inc.

- Haala, N., M. Peter, J. Kremer, and G. Hunter (2008). LiDAR mapping for 3D point cloud collection in urban areas - a performance test. *International Archives of Photogrammetry, Remote Sensing and Spatial Information Sciences 37 (Part B5)*, 1119 – 1124.
- Habib, A., M. Morgan, and Y. Lee (2002). Bundle adjustment with self-calibration using straight lines. *Photogrammetric Record 17(6)*, 635 – 650.
- Habib, A. F., M. Al-Durgham, A. P. Kersting, and P. Quackenbush (2008). Error budget of LiDAR systems and quality control of the derived point cloud. *International Archives of Photogrammetry, Remote Sensing and Spatial Information Sciences 37 (Part B1)*, 203 – 209.
- Harrap, R. and S. Daniel (2009). Mobile lidar mapping: Building the next generation of outdoor environment model for ar. In *Workshop: Let's Go Out: Research in Outdoor Mixed and Augmented Reality*.
- Hefford, S. W., C. Samson, J. W. Harrison, F. P. Ferrie, K. Kusevic, P. Mrstik, and P. J. W. Iles (2009). Augmenting the iterative closest point (ICP) alignment algorithm with intensity. *GEOMATICA 63*, 407 – 418.
- Heikkilä, R., M. Jaakkola, T. Saarenketo, and F. Malaguti (2004). Modeling information flows for automated road rehabilitation process. *International Symposium on Automation and Robotics in Construction*.
- Hong, S., M. Lee, H. Chun, S. Kwon, and J. Speyer (2006). Experimental study on the estimation of lever arm in GPS/INS. *IEEE Transactions on Vehicular Technology 55(2)*, 431 – 448.
- Hunter, G. (2009). Laser scanning: There's more than one option. *Engineering and Mining Journal 210*, 33 – 34.

- IGI (2011). IGI GmbH. Webpage: aerocontrol series specifications. http://www.igi.eu/aerocontrol.html?file=tl_files/IGI/Brochures/AEROcontrol/AEROcontrol_specs.pdf. [Online; accessed 06-Nov-2011].
- Ishikawa, K., J. Takiguchi, Y. Amano, T. Hashizume, and T. Fujishima (2009). Tunnel cross-section measurement system using a mobile mapping system. *Journal of Robotics and Mechatronics* 21(2), 193 – 199.
- Jwa, Y. and G. Sohn (2009). Automatic 3D powerline reconstruction using airborne lidar data. *International Archives of Photogrammetry, Remote Sensing and Spatial Information Sciences* 38 (Part 3/W8), 105 – 110.
- Kaasalainen, S., H. Kaartinen, A. Kukko, K. Anttila, and A. Krooks (2011). Brief communication: Application of mobile laser scanning in snow cover profiling. *The Cryosphere* 5, 135 – 138.
- Katzenbeisser, R. (2003). About the calibration of LiDAR sensors. *International Archives of Photogrammetry, Remote Sensing and Spatial Information Sciences* 34 (Part 3/W13), 59 – 64.
- Kim, H. B. and G. Sohn (2011). Random forests based multiple classifier system for power-line scene classification. *International Archives of Photogrammetry, Remote Sensing and Spatial Information Sciences* 38 (Part 5/W12), [On CD-ROM].
- Kremer, J. and G. Hunter (2007). Performance of the StreetMapper mobile LiDAR mapping system in real world projects. In *Photogrammetric Week' 07*, Heidelberg, Germany.
- Kukko, A., H. Kaartinen, S. Kaasalainen, M. Vaaja, and K. Anttila (2010). Experiences of mobile mapping in environmental monitoring. In *Dept. of Remote Sensing and Photogrammetry, Finnish Geodetic Inst*, Masala, Finland.

- Kumari, P., W. Carter, and R. Shrestha (2011). Adjustment of systematic errors in ALS data through surface matching. *Advances in Space Research* 47(10), 1851 – 1864.
- Lam, S. Y. W. (2010). Recent advances of engineering survey operations for tunnel construction in Hong Kong. In *FIG Congress 2010 Facing the Challenges Building the Capacity*, Sydney, Australia.
- Leslar, M. (2009). Extraction of geo-spatial information from LiDAR-based mobile mapping system for crowd control planning. In *IEEE Toronto International Conference - Science and Technology for Humanity*, Toronto, Canada, pp. 468–472.
- Leysens, J. (2009). *GNSS positioning for UAV Applications - International Symposium Light Weight Unmanned Aerial Vehicle Systems and Subsystems*.
- Lichti, D., S. Gordon, and T. Tipdecho. Error models and propagation in directly georeferenced terrestrial laser scanner networks. *ASCE Journal of Surveying Engineering* 131.
- Lichti, D. D. (2007). Error modelling, calibration and analysis of an AM-CW terrestrial laser scanner system. *ISPRS Journal of Photogrammetry and Remote Sensing* 61(5), 307 – 324.
- Lichti, D. D. (2010). Terrestrial laser scanner self-calibration: correlation sources and their mitigation. *ISPRS Journal of Photogrammetry and Remote Sensing* 65(1), 93 – 102.
- Lichti, D. D., S. Brustle, and J. Franke (2007). Self calibration and analysis of the surphaser 25HS 3D scanner. In *FIG Working Week 2007*, Volume 65, pp. 93 – 102.
- Lichti, D. D., J. Chow, and H. Lahamy (2011). Parameter de-correlation and model-

- identification in hybrid-style terrestrial laser scanner self-calibration. *ISPRS Journal of Photogrammetry and Remote Sensing* 66(3), 317 – 326.
- McLaughlin, R. (2006). Extracting transmission lines from airborne LiDAR data. *IEEE Geoscience and Remote Sensing Letters* 3, 222 – 226.
- Mikhail, E. M. and F. Ackerman (1976). *Observations and Least Squares*. Lanham, US: University Press of America.
- Morgan, D. (2009). Using mobile LiDAR to survey railway infrastructure. Lynx mobile mapper. In *FIG Commissions 5, 6 and SSGA Workshop -Innovative Technologies for an Efficient Geospatial Management of Earth Resources*, Lake Baikal, Russian Federation.
- Morin, K. W. (2003). Calibration of airborne laser scanners. *M.Sc. thesis, Department of Geomatics Engineering, University of Calgary, UCGE Report No. 20179*.
- Mostafa, M. and K. Schwarz (2001). Digital image georeferencing from a multiple camera system by GPS/INS. *ISPRS Journal of Photogrammetry and Remote Sensing* 56(1), 1 – 12.
- Ohio State University (2011). GPSVanTM project. <http://www.cfm.ohio-state.edu/research/gpsvan.php>. [Online; accessed 06-Nov-2011].
- Optech (2011). Optech Inc. Webpage: Lynx Data Sheet. <http://www.optech.ca/pdf/LynxDataSheet.pdf>. [Online; accessed 24-Oct-2011].
- Petrie, G. (2010). An introduction to the technology mobile mapping systems. *GEOinformatics Magazine* 13(1), 32 – 43.
- Puttonen, E., A. Jaakkola, P. Litkey, and J. Hyypä (2011). Tree classification with fused mobile laser scanning and hyperspectral data. *Sensors* 11(5), 5158 – 5182.

- Reshetyuk, Y. (2010). A unified approach to self-calibration of terrestrial laser scanners. *ISPRS Journal of Photogrammetry and Remote Sensing* 65(5), 445 – 456.
- Rieger, P., N. Studnicka, M. Pfennigbauer, and G. Zach (2010). Bore-sight alignment method for mobile laser scanning systems. *Journal of Applied Geodesy* 4, 13 – 21.
- Samama, N. (2008). *Global Positioning Techniques and Performance*. Hoboken, New Jersey: John Wiley and Sons, Inc.
- Schwarz, K. and N. El-Sheimy (2004). Mobile mapping technologies: State of the art and future trends. *International Archives of Photogrammetry, Remote Sensing and Spatial Information Sciences* 35 (Part B5), 759 – 768.
- Shakarji, C. (1998). Least-squares fitting algorithms of the NIST algorithm testing system. *Journal of Research of the National Institute of Standards and Technology* 103(6), 633 – 641.
- Shan, J. and C. K. Toth (2009). *Topographic Laser Ranging and Scanning*. CRC Press.
- Shi, Y., R. Shibasaki, and Z. C. Shi (2008). Towards automatic road mapping by fusing vehicle-borne multi-sensor data. *International Archives of Photogrammetry, Remote Sensing and Spatial Information Sciences* 37 (Part B5), 867 – 872.
- Skaloud, J. (1999). Optimizing georeferencing of airborne survey systems by INS/DGPS. *Ph.D thesis, Department of Geomatics Engineering, University of Calgary, UCGE Report No. 20126*.
- Skaloud, J. and D. Lichti (2006). Rigorous approach to bore-sight self-calibration in airborne laser scanning. *ISPRS Journal of Photogrammetry and Remote Sensing* 61(1), 47–59.

- Sun, D. (2010). Ultra-tight GPS/reduced IMU for land vehicle navigation. *Ph.D thesis, Department of Geomatics Engineering, University of Calgary, UCGE Report No. 20305.*
- TITAN (2011). Ambercore software inc. webpage: Titan underground for mineshafts and tunnels. <http://www.ambercore.com/files/TITANUndergroundDatasheet%20Dec09%20v5.1.pdf>. [Online; accessed 06-Nov-2011].
- Trimble (2011). Trimble Inc. Webpage: Trimble's VRSTM (Virtual Reference Station) Networks Provide High Quality RTK Positioning Data on Demand. <http://www.trimble.com/vrs.shtml>. [Online; accessed 06-Nov-2011].
- Ussyshkin, R., L. Theriault, M. Sitar, and T. Kou (2011). Advantages of airborne LiDAR technology in power line asset management. In *Multi-Platform/Multi-Sensor Remote Sensing and Mapping (M2RSM), 2011 International Workshop*, Xiamen, China. [On CD-ROM].
- Ussyshkin, R. V. and R. B. Smith (2007). A new approach for assessing LiDAR data accuracy for corridor mapping applications. In *Conference Proceedings, The 5th International Symposium on Mobile Mapping Technology*, Padua, Italy.
- Vaaja, M., M. Kurkela, H. Hyyppä, P. Alho, J. Hyyppä, A. Kukko, H. Kaartinen, E. Kasvi, S. Kaasalainen, and P. Rönholm (2011). Fusion of mobile laser scanning and panoramic images for studying river environment topography and changes. *International Archives of Photogrammetry, Remote Sensing and Spatial Information Sciences 38 (Part 5/W12)*, [On CD-ROM].
- Vallet, J. and J. Skaloud (2004). Development and experiences with a fully-digital handheld mapping system operated from a helicopter. *International Archives of Photogrammetry, Remote Sensing and Spatial Information Sciences 35 (Part B5)*, 791 – 796.

- VectorNav (2011). VectorNav Technologies Inc. Webpage: Inertial Navigation Article. http://www.vectornav.com/index.php?option=com_content&view=article&id=21&Itemid=11. [Online; accessed 06-Nov-2011].
- Vollath, U., A. Buerchl, H. Landau, C. Pagels, and B. Wagner (2000). Long-range RTK positioning using virtual reference stations. In *Proceedings of ION GPS 2000, 13th International Technical Meeting of the Satellite Division of the Institute of Navigation*, Salt Lake City, USA.
- Vosselman, G. and H. Mass (2010). *Airborne and Terrestrial Laser Scanning*. Whittles Publishing.
- Wang, J. and F. Jin (2010). Precision estimation of mobile laser scanning system. *Survey Review* 42(317), 270 – 278.
- Wells, D. E. and E. Krakiwsky (1971). *The method of least squares. Geodesy and Geomatics Lecture Notes*. University of New Brunswick.
- Wildi, T. and R. Glaus (2002). A multisensor platform for kinematic track surveying. In *2nd Symposium on Geodesy for Geotechnical and Structural Engineering*, Sydney, Australia.
- Xu, G. (2007). *GPS: Theory, Algorithms and Applications*. Heidelberg, Germany: Springer.
- Zhu, L., J. Hyypä, A. Kukko, H. Kaartinen, and R. Chen (2011). Photorealistic building reconstruction from mobile laser scanning data. *Remote Sensing* 3(7), 1406 – 1426.